Design Aspects of n-type Metal Oxide Based Photoanodes for Electrochemical Performance

A Dissertation Submitted to the
Indian Institute of Technology Guwahati
in Partial Fulfilment for the Degree of

DOCTOR of PHILOSOPHY

by

Manoj Kumar Mohanta

DEPARTMENT OF CHEMISTRY
INDIAN INSTITUTE OF TECHNOLOGY GUWAHATI
GUWAHATI, ASSAM, INDIA

OCTOBER 2022

Design Aspects of n-type Metal Oxide Based Photoanodes for Electrochemical Performance

A Dissertation Submitted to the
Indian Institute of Technology Guwahati
in Partial Fulfilment for the Degree of

DOCTOR of PHILOSOPHY

by

Manoj Kumar Mohanta
Roll No. 176122015
DEPARTMENT OF CHEMISTRY

DEPARTMENT OF CHEMISTRY
INDIAN INSTITUTE OF TECHNOLOGY GUWAHATI
GUWAHATI, ASSAM, INDIA
OCTOBER 2022

STATEMENT

I hereby declare that the scientific findings included in this thesis entitled, "**Design Aspects of n-type Metal Oxide Based Photoanodes for Electrochemical Performance**" is the outcome of research work carried out by me under the supervision of Prof. Mohammad Qureshi, at Department of Chemistry, Indian Institute of Technology Guwahati, Guwahati, Assam, India, for the award of the degree of Doctor of Philosophy.

The work embodied in this thesis is the result of original research done by me except where otherwise stated in this thesis with proper citations. I confirm that the investigations were conducted in accordance with the ethics policies and integrity standards of Indian Institute of Technology Guwahati and that the research data are presented honestly and without prejudice. The thesis work has not been submitted for a degree or professional qualification to any other university or institution.

IIT Guwahati — Manoj Kumar Mohanta

October 2022 — Candidate

Professor Mohammad Qureshi
Department of Chemistry
Indian Institute of Technology Guwahati
Guwahati – 781036, India
Tel: +91 – 361 – 2582320;
Fax: +91 – 361 – 2582349
Email: mq@iitg.ac.in

Certificate

Certified that the work described in this thesis entitled "**Design Aspects of n-type Metal Oxide Based Photoanodes for Electrochemical Performance**" by Mr. Manoj Kumar Mohanta, Department of Chemistry, Indian Institute of Technology Guwahati has been carried out under my supervision and has not been submitted elsewhere for a degree.

Guwahati
October 2022

Prof. Mohammad Qureshi
Thesis supervisor
Department of Chemistry
Indian Institute of Technology Guwahati
Guwahati – 781039, Assam, India

ACKNOWLEDGEMENT

Undertaking this PhD has been a truly life-changing experience for me and it would not have been possible to do without the support and guidance that I received from many people.

It is a genuine pleasure to express my deep sense of thanks and gratitude to my mentor and thesis adviser, Professor Mohammad Qureshi, for his continuous support throughout my PhD tenure. I sincerely thank him for his constant guidance, encouragement and freedom to work which assisted me in completing the work assembled in the thesis. I could not have imagined having a better advisor and mentor for my research study.

I am extremely grateful to my doctoral committee members, Prof. Aditya Narayan Panda, Prof. Chivukula V Sastri and Dr. Nageswara Rao Peela for their assistance and suggestions throughout my PhD work. I would like to thank all faculty members and staff members of Chemistry department. My sincere thanks to the staff of Central Instruments Facility for their help and in hand guidance to several analytical instruments required during my research work. Special thanks to Milan and Sujit for teaching me the operation of FETEM instrument. Also, thanks to Mr. Madhurjya Borah and Sumit Bhaiya for teaching me the operation of AFM instrument. I wish to express my sincere gratitude to IIT Guwahati for all the facilities that were made available to me and the Ministry of Human Resource Development (MHRD), India for the financial support.

I would like to thanks my past and present lab members - Dr. Anindya, Dr. Shaad, Dr. Avishek, Dr. Gaurangi, Dr. Tushar, Dr. Suhaib, Dr. Adit, Sourav, Moite, Nitul, Alpana, Piyush and Anjana for their timely help, support and for creating a pleasant atmosphere in the lab. I would especially like to thanks Dr. Tushar, Dr. Avishek and Dr. Shaad for teaching me basics, experiments and handling instruments in the initial periods of my research work.

I extend my sincere thanks to my beloved friends, Umesh Bhai, Jagnyesh, Bipin, Manmath, Siba, Paresh, Ashish, Chandra, Debojit, Subhamoy, Arpita and Angana for all the love and support throughout this time.

Apart from the research activities, the joyous and memorable time spent with my dearest friends, juniors and seniors, Satyam, Rakesh, Dibya, Shakti, Dhwaneet, Sandhya, Sandeep, Ashish, Himanshu, Suman, Lucky, Abhishek, Chandu Bhaiya, Ashish Bhaiya, Sumanta Bhaiya, Abhi Bhaiya, Satya Bhaiya, Biswajit Bhaiya, Ketan Bhaiya, Dhanesh Bhaiya,

Dileep Bhaiya, Subash Bhaiya and Niranjan Bhaiya is unforgettable. Thank you guys for always being there for me in my good and bad times.

My sincere thanks to Ankush, Sweta and Saptarshi Da for the support and help they extended whenever required.

Finally, my Ph. D. endeavor could not have been completed without the endless love, unending support, tolerance and blessings from my family. I would like to express my deepest gratitude to my parents for all the unconditional love and sacrifices they have made for the sake of my upbringing. I am also grateful to my sister, brother and cousins for their affection and deep concern for my career.

Still, many names are missing whose contribution and help is worth mentioning.

Manoj

Dedicated

To

My Beloved Parents

Family and Friends

Table of Contents

Thesis Title: **Design aspects of n-type metal oxide based photoanodes for electrochemical performance**

Name of the Candidate: Manoj Kumar Mohanta

Registration Number: 176122015

Thesis Supervisor: Prof. Mohammad Qureshi

Department: Chemistry

Institute: Indian Institute of Technology Guwahati, Assam – 781039, India.

Thesis Overview

Chapter 1: Introduction and literature survey

This chapter elucidates the engineering and fabrication aspects of metal oxide based semiconductors for solar energy harvesting, maximized photoinduced electron/hole separation and transportation by minimizing recombination. Also, this chapter discusses the basics on photoelectrochemical (PEC) water splitting, working principle, new challenging approaches to develop photoelectrodes for improved PEC performance based on the reported literature. The superiority of an photoanodes having suitable band alignment, bandgap and earth abundance has been explained. The major strategies of modified photoanode related to structure engineering, elemental doping, different heterojunctions, surface passivation, hole extraction and co-catalyst modification have been discussed briefly.

Chapter 2: Experimental section

This chapter covers the discussions of material synthesis, fabrication and characterizations for PEC water oxidation. All characterization techniques related to materials analysis have been mentioned. The PEC measurements along with the experimental set up have also been discussed. The PEC water oxidation related measurements have been analyzed through various instruments such as CHI1120B potentiostat (linear sweep voltammetry analysis), GAMRY INTERFACE 1010 E potentiostat (LSV, electrochemical impedance spectroscopy and Mott−Schottky analysis),

Newport Oriel IQE-200 (incident photon to current efficiency), Agilent 7820A gas chromatography (Faradaic yield of hydrogen and oxygen gas evolution), etc. The crucial PEC techniques have been discussed briefly for better understanding.

Chapter 3: Electronic structure modulations of monoclinic tungsten oxide nanoblocks by indium doping for boosted photoelectrochemical performance [Chem Asian J. 2020, 15, 3886]

This chapter offers the hydrothermal growth of In-doped monoclinic WO_3 nanoblocks directly over fluorine doped tin oxide (FTO) substrate without the aid of any seed layer. X-ray photoelectron spectroscopy (XPS) data reveals the shifting W^{6+} peaks to lower binding energy by In^{3+}-doping which attributes the shorting of W-O bond and indicates that In^{3+} ions are partially occupying the W^{6+} ions in In-doped WO_3 photoanode. The maximum current density value of 2.18 mA/cm^2 has been provided by the optimized In-doped WO_3 photoanode with 3 wt% indium doping at 1.23 V vs. RHE, which is ~3 times higher than that of undoped monoclinic WO_3 photoanode. Mott-Schottky (MS) analysis reveals charge carrier density (N_D) for In-doped WO_3 photoanode has been enhanced by a factor of 3. The Schematic band position analysis (a) and the application in PEC activity (b) are shown in figure **1**.

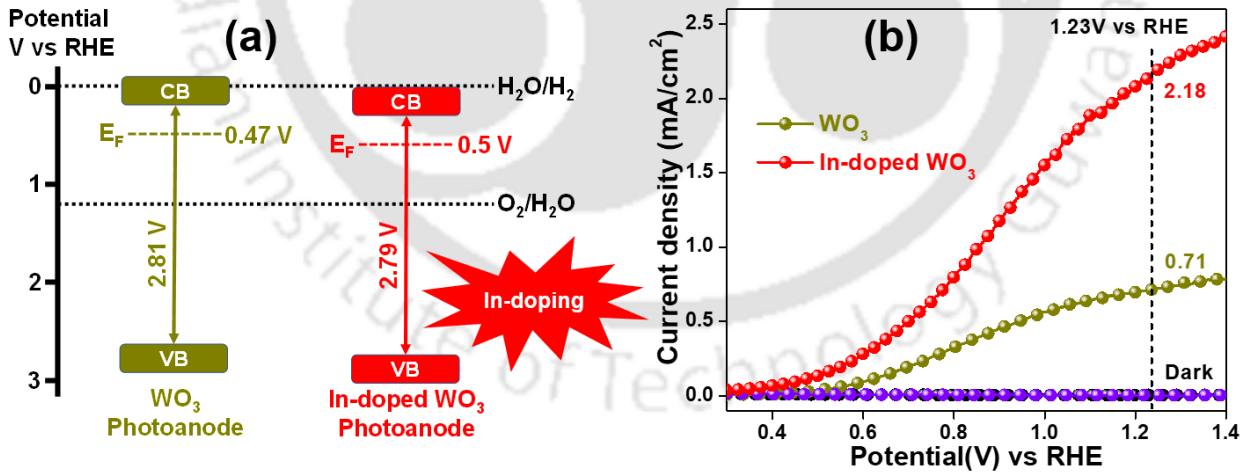

Figure 1. (a) Schematic band position analysis of bare WO_3 and In-doped WO_3 photoanodes; (b) Linear sweep voltammetry curves of bare WO_3 and In-doped WO_3 photoanodes in 0.1 M Na_2SO_4 electrolyte under 1 Sun illumination @ 10 mV/s scan rate at 1.23 V vs. RHE.

Chapter 4: Hexagonal boron nitride as a superior hole extractor for efficient charge separation in WO_3-based photoelectrochemical water oxidation [ACS Appl. Energy Mater. 2019, 2, 7457]

This chapter demonstrates the modification of stable monoclinic WO_3 nanoblocks with hexagonal boron nitride quantum dots (h-BNQDs) incorporation to improve the photogenerated electron−hole separation and additionally to hinder the charge recombination process. The photocurrent density (J) value for the modified WO_3 photoanode by incorporation of BNQDs has been found to be 1.63 mA/cm^2 at the potential of 1.23 V vs. RHE, which is approximately 2.4-fold higher than the bare WO_3 photoanode. The enhancement in photocurrent density is mainly due to the hole extraction property of BNQDs on the surface of the WO_3 nanoblocks. The present work demonstrates a unique, low-cost strategy for enhancement of PEC water oxidation by modification of the photoanode with hole extracting agents. The schematic illustration of hole extraction mechanism by BNQD from WO_3 photoanode (a) and the PEC analysis (b) are shown in figure **2**.

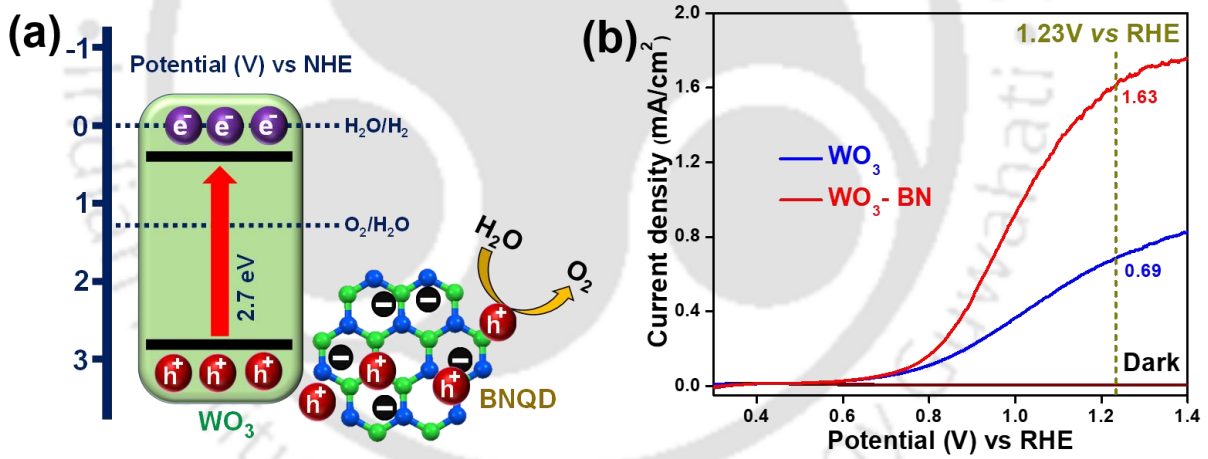

Figure 2. (a) Schematic illustration of hole extraction mechanism by BNQD from WO_3 photoanode to improve the photogenerated electron−hole separation and additionally to hinder the charge recombination process; (b) Linear sweep voltammetry curves of bare WO_3 and modified WO_3-BN photoanodes in 0.1 M Na_2SO_4 electrolyte under 1 Sun illumination @ 1.23 V vs. RHE.

Chapter 5: Surface charge directed borophene - phosphorous nitride heterojunction formation for enhanced electrochemical performance in tungsten oxide based photoanodes

[Chem. Commun., 2023, 59, 1955–1958]

This chapter determines the widely explored zero dimensional (0D) non-metal based materials for photoelectrochemical (PEC) electrode modification due to their faster charge transfer and better light harvesting abilities. Herein, we have designed a complimentary charged nanosized 0D-0D hybrid assemble of phosphorous nitride dots (PNDs) (**ς = + 9.5 mV**) and borophene dots (BDs) (**ς = - 26.2 mV**) having favorable type-II heterojunction approach among them. A model system has been studied using WO_3 as a semiconductor for showing the effectiveness of PNDs-BDs for PEC water oxidation. The type-II-II′ heterojunction based WO_3/PNDs-BDs photoanode offers a significant four -fold higher current density of 2.8 mA/cm^2 at 1.23 V vs RHE in comparison to the bare WO_3 photoanode. The oppositely charged 0D-0D hybrid model provides rapid carrier separation along with minimized carrier recombination to metal oxide based semiconductor for enhanced PEC water oxidation. The schematic of the composite photoanode, followed by type-II-II′ heterojunctions, proposing a detailed charge transfer mechanism within the components (a) and the related PEC analysis (b) are shown in figure **3**.

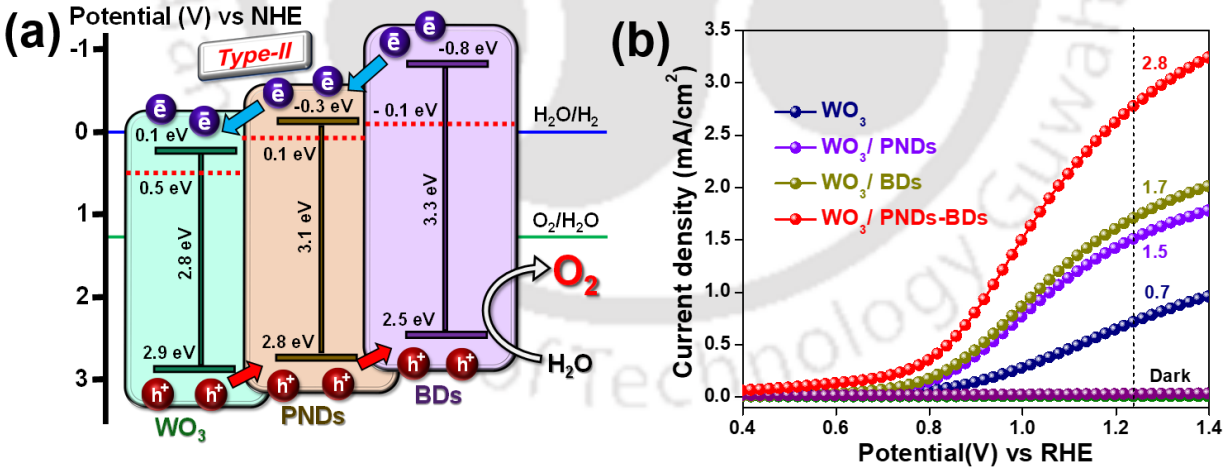

Figure 3. (a) Schematic of the type-II-II′ based WO_3/PNDs-BDs composite photoanode proposing the detailed charge transfer mechanism within the components; (b) LSV curves and of WO_3, WO_3/PNDs, WO_3/BDs and WO_3/PNDs-BDs photoanodes under 1 Sun illumination in 0.1 M Na_2SO_4 electrolyte at 1.23 V vs RHE.

Chapter 6: Synchronized carrier extraction and injection through boron nitride nanoplatelets in hierarchical $BiVO_4$/CoCr-layered double hydroxides for efficient water oxidation [Electrochimica Acta, 2022, 415, 140269]

This chapter offers the interfacial insertion of hole extractor between semiconductor photoanode and surface oxygen evolution catalyst (OECs) for amplified photoelectrochemical (PEC) water oxidation performance. Herein, modifications of bare monoclinic $BiVO_4$ photoanode with two dimensional boron nitride nanoplatelets (BNNPs) as hole extractor and CoCr-layered double hydroxides (CoCr-LDH) as kinetics accelerator results to achieve a maximum photocurrent density of 3.8 mA/cm^2 at 1.23 V vs RHE along with a cathodic shift of ~360 mV onset photocurrent, which indicates the 3.2 fold enhancement in photo-current density in comparison to

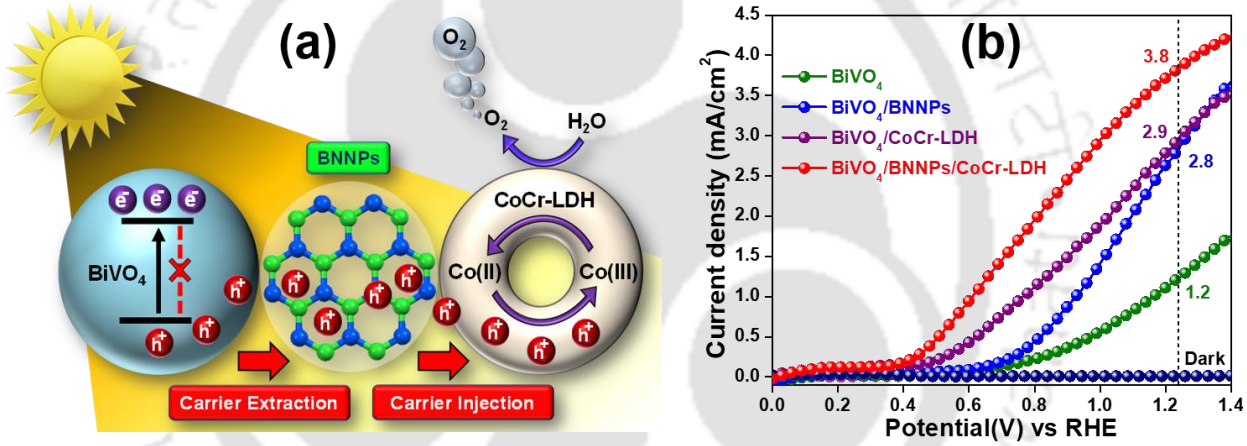

Figure 4. (a) Schematic proposed mechanism of the $BiVO_4$/BNNPs/CoCr-LDH photoanode for enhanced PEC water oxidation; (b) LSV curves and of $BiVO_4$, $BiVO_4$/BNNPs, $BiVO_4$/CoCr-LDH and $BiVO_4$/BNNPs/CoCr-LDH photoanodes under 1 Sun illumination in 0.1 M Na_2SO_4 electrolyte at 1.23 V vs RHE.

bare $BiVO_4$. Semiconductor/hole extractor/OECs composite photoanode, i.e., $BiVO_4$/BNNPs/CoCr-LDH offers speedy charge separation with suppressed charge recombination to accelerate the PEC water oxidation kinetics. The presented work is promising as it fill-in the gap between the photoanode and OECs for boosting the PEC water oxidation efficiency of metal-oxide based photoanode. The proposed mechanism of the $BiVO_4$/BNNPs/CoCr-LDH photoanode for enhanced PEC water oxidation (a) and the related PEC water oxidation performances (b) are shown in the figure **4**.

Conclusions and overview

In conclusion, we have tuned the electronic structure and surface activities of the known metal oxide photoanodes by applying different efficient strategies such as metal dopant modification, hole extractor incorporation, co-catalyst modification and type-II heterojunction fabrication, etc. We have used narrow bandgap photoanodes having ~ 2.4 to ~ 2.8 eV bandgaps for fabrication of high performance hybrid photoanodes. Our approached strategies offer enhanced charge carrier density, maximized photogenerated electron-hole separation along with minimized recombination, high water oxidation kinetics of the known photoanodes for boosted PEC performance. Also, these present strategies demonstrate a unique, low-cost, stable and effective hybrid photoanodes for enhancement of PEC water oxidation.

CHAPTER 1

Introduction and Literature Survey

This chapter describes the motivation for photoelectrochemical water oxidation. The growing global energy demand and global warming are challenging us to discover new alternative renewable energy sources and solutions. Solar energy has the potential to tackle the desired challenge. It describes the features of metal oxide semiconductors as photoanode for photoelectrochemical water splitting and provides new approaches to overcome the photoanodic limitations.

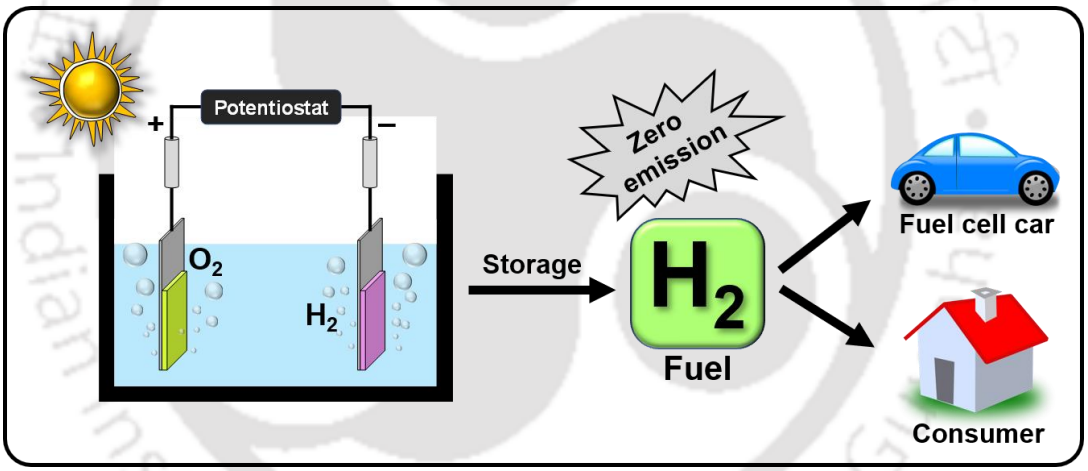

1.1 GLOBAL ENERGY CALAMITY AND CLIMATE VARIABILITY: AN OVERVIEW

In the coming decades, our biosphere is going to tackle two major challenges of energy source and climate variation, which are strongly related to each other. The energy demand has enhanced exponentially after the industrial rebellion.[1] The recent estimation of the world population is noted to be ~ 7.96 billion with ~ 25 terawatts (TW) power consumption.[2,3] The predicted world population by 2050 will be reached up to ~ 9 billion with ~ 40 TW power consumption.[3] Recently, our primary energy resources are non-renewable and related to fossil fuels, i.e., coal, oil, natural gases, etc. However, fossil fuels are always ready to cause global warming and some other unwanted effects by releasing greenhouse gases such as CO_2 into the atmosphere.[4] The atmospheric CO_2 gas has a tendency to absorb infrared radiation, which leads to enhance normal atmospheric temperature. In the last few decades, the increment percentage of CO_2 gas emission is noted to be 3 % per year.[5] If the release rate of CO_2 gas remains the same, then there will be a terrible warning for human civilization and the environment.

According to the international energy agency (IEA) report, the level of difficulty in controlling greenhouse emissions is being maximized every year.[3] The energy division has to play a major role to minimize the uncontrollable emissions of greenhouse gases. The development of innovative technologies is really essential to tackle the global energy demand with no greenhouse gas emissions. Recently, the emission of greenhouse gases from the consumption of oil and coal covers more than 70% of the world's greenhouse gas. To avoid the devastating consequences, the Intergovernmental Panel on Climate Change (IPCC) warns that the raised temperature related to global warming and the atmospheric CO_2 concentration should always be below 2 °C and 450 ppm, respectively.[6] To achieve the minimum worldwide emissions of CO_2 gas, awareness of climate change and the related consequences should be considered globally. The development of noble technologies generating low percent of CO_2 emission has to be enhanced for alternative energy sources. In 2015, United Nations Climate Change Conference, 197 countries have signed to control the raised temperature below 2 °C related to global warming.[7] To overcome the present scenario, renewable energy systems with advanced technologies should be invented to tackle the global energy demand and climate change.

1.2 RENEWABLE ENERGY SOURCES

The development of new innovative technologies with renewable carbon-free energy sources is essential to resolve global energy demands along with fossil fuel-based global warming. Renewable carbon-free energy sources such as solar, wind, nuclear, geothermal, and hydroelectric energy systems, etc., are responsible for the reduction of CO_2 emission and have the potential to fulfill the energy demand. **Figure 1.1** is the current distribution of the energy sources, which indicates the dominant position of solar energy among all other non-renewable and renewable energy systems.[8] Some part of the projected solar energy falls on the earth's surface and that energy is measured as solar irradiance. The wavelength (λ) of solar radiation that reaches to earth is in the range of 100 nm to 1mm. The yearly flow of energy from the Sun to earth is very high, i.e., in several orders of magnitude in comparison to other renewable sources. A very high energy of ~ 1,73,000 TW, i.e., 1000 times higher compared to human energy demand, is provided by the Sun to earth.[9] Solar energy is sufficient enough to fulfill human lifetime energy demand. The challenging part is to cover the harvesting, storing and application of solar energy by approaching innovative economically feasible methods. Solar power is the only one having the sufficient potential to fulfill the global energy demand in recent and future times with zero CO_2 emission.

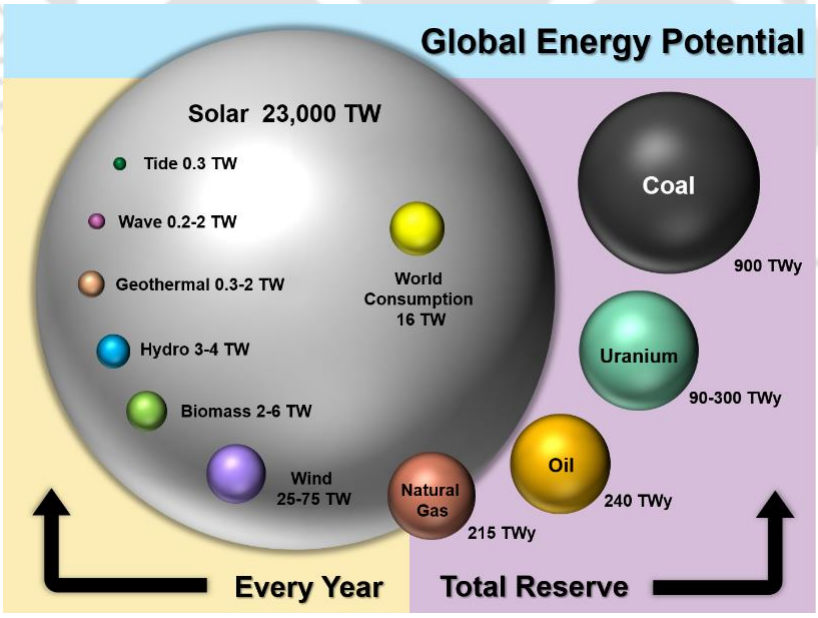

Figure 1.1 Availability of energy sources on the earth that can be applied for energy production (reproduced from source: https://commons.wikimedia.org/wiki/File:Global_Energy_Potential_2014_08_09.svg).

Among various technologies, photovoltaic, solar thermal, and solar fuels are able to harvest solar power prominently from the Sun. Photovoltaics is known to be one of the strong-growing industries having widely distributed technologies.[10] But in photovoltaics, the storage of generated electricity is having an intrinsic issue.[11] For proper utilization of solar power, a noble approach corresponds to the conversion of energy from solar to chemical form along with its storage. Hydrogen (H_2) production from water splitting by utilizing solar power is known to be a promising fuel for harvesting solar energy, which involves fuel cells with no CO_2 emissions.[12]

The zero-emission fuel, popularly known as hydrogen, has a very high ~141.7 MJ kg^{-1} calorific figure in comparison to other conventional energy sources such as methane (~ 55.5 MJ kg^{-1}), diesel (~ 45.6 MJ kg^{-1}), kerosene (~ 46.2 MJ kg^{-1}) and gasoline (~ 46.4 MJ kg^{-1}).[13,14] In recent times, coal gasification and steam reforming methane gas are the major techniques to produce H_2 gas on an industrial scale. However, these techniques emit a huge amount of greenhouse gases.[15] Therefore, it is necessary to get a low-cost noble approach for efficient carbon-free H_2 fuel generation having remarkably high efficiency and good sustainability. Recently, an extensive techno-economic analysis (TEA) has published a report on the feasibility of H_2 generation from water electrolysis based renewable energy systems.[16] Among numerous ways, photoelectrochemical (PEC) water splitting is a futuristic way to tackle energy demand by generating H_2 fuel.

1.3 PHOTOELECTROCHEMICAL WATER SPLITTING

Photoelectrochemical (PEC) water splitting, a futuristic way to harvest clean and sustainable hydrogen fuel driven by solar energy for resolving the global energy demand. PEC water splitting is similar to electrolysis, involving two processes, i.e., water reduction at the cathode for hydrogen generation and water oxidation at the anode for oxygen generation.[17,18] The major advantage of the PEC system is the generation of both hydrogen and oxygen gas separately during the process.[19] It is essential for at least one electrode to be a semiconductor having light harvesting ability.[20] In general, n-type semiconductor based photoanodes are exposed to sunlight for electron-hole pair generation through photoexcitation of electrons (e^-) in the photoanode from the valence band (VB) to the conduction band (CB), leaving behind the holes (h^+) at VB. The remaining h^+ carriers at the VB move to the photoanodic surface for promoting water oxidation activity and the e^- carriers at the CB move to the cathodic surface via an external circuit for

promoting water reduction activity.[21-23] The corresponding chemical reactions with a schematic for this PEC activity are provided below in **Figure 1.2**:[24,25]

$$\text{Cathode: } 2H^+ + 2e^- \rightarrow H_2\ ;\ E^0_{\text{reduction}} = 0V \quad (1.1)$$

$$\text{Photoanode: } 2H_2O + 4h^+ \rightarrow O_2 + 4H^+\ ;\ E^0_{\text{oxidation}} = 1.23V \quad (1.2)$$

$$\text{Overall water} - \text{splitting: } 2H_2O \rightarrow 2H_2(g) + O_2(g) \quad (1.3)$$

For water splitting processes, a minimum potential of 1.23 V, followed by the above reaction and the Nernst equation, is needed. In general, minimum thermodynamical photon energy of 1.23 V is needed to split water into hydrogen and oxygen. Hence, the semiconductors with a minimum 1.23 eV bandgap is crucial for water splitting. In principle, to drive water oxidation and reduction reactions by the charge carriers upon light illumination, the VB and CB of the semiconductor must be more positive (+ve) than 1.23 V vs NHE and more negative (-ve) than 0 V vs NHE, respectively.[26]

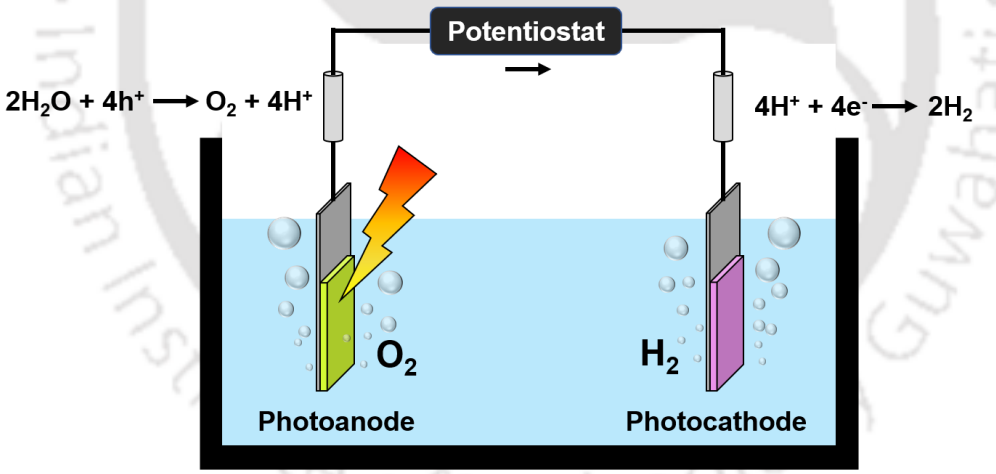

Figure 1.2 Schematic of PEC cell in which water is oxidized to O_2 at photoanode and water is reduced to H_2 at photocathode.

Though semiconductors play a key role in PEC water splitting under light irradiation, some other related features will reduce the PEC efficacy. As the maximum portion of the solar illumination meets to earth with visible range, i.e., 400 to 700 nm, it is important to choose a semiconductor having suitable band alignment and bandgap to harvest maximum light.[27] The Planck's energy–frequency relation ($E=h\nu=h(C/\lambda)$) confirms the bandgap of visible light

responsive materials (photoactive materials) to be in the range of 3.1 eV to 1.7eV. A major drawback in PEC activity is the recombination of electron-hole carriers at the interface of semiconductor and electrolyte because of the surface and lattice defects. It is challenging to drive oxidation, reduction reactions and solid-liquid interfacial kinetics by using an appropriate material having the desired overpotential.[28] The semiconductors with a suitable bandgap range of ~ 1.6 to ~ 2.4 eV are the appropriate materials to drive PEC water splitting.[29] Understanding the kinetics, thermodynamics and physical parameters related to catalyst surface and semiconductor electrolyte interface is really important to design an ideal semiconductor for boosted PEC water splitting.

1.4 APPROACHES TO IMPROVE PHOTOELECTROCHEMICAL PERFORMANCE

The most focused inquiry in PEC water splitting is the generation of H_2 and O_2 gas by the semiconductor-based catalyst. Photoanodic oxidation is the crucial primary reaction for photocathodic reduction to generate H_2 gas. According to **equation 1.2**, for one molecule of O_2 generation, four electrons and protons were extracted from two molecules of water. To oxidize water molecule in single step, it is exceedingly difficult to accumulate and store four numbers of oxidized electron-hole pairs in the photoanode. The overall PEC water splitting is hindered by both thermodynamic and kinetic complications.[30] Hence, the designing of efficient PEC water oxidation catalysts is the primary essential feature to develop an ideal efficient PEC device.

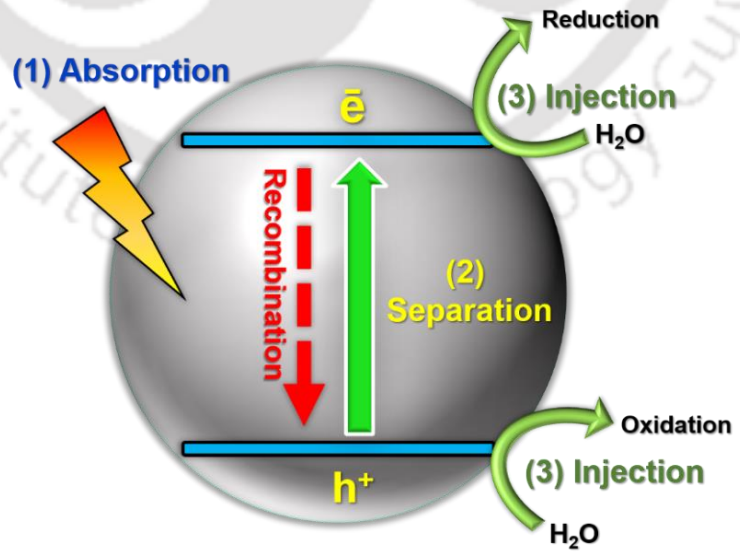

Figure 1.3 PEC activities and the related features to influence its performance.

The PEC water oxidation includes solar energy harvesting, electron-hole carriers generation, photogenerated charge carriers separation and recombination, charge carriers transportation and surface reactions.[31,32] The major criteria to be an ideal photoanode are (I) VB has to be more +ve than 1.23 V vs NHE; (II) light absorption range should be broadened; (III) maximized charge carriers separation by minimizing recombination; (IV) maximum transportation of charges to the photoanodic surface; (V) having high active surface sites; (VI) faster kinetics for water oxidation; (VII) longer operational stability in different electrolytes with a wide range of pH; (VIII) Ecofriendly and cost-effective.[33] **Figure 1.3** represents the schematic of PEC activity having different features to influence the performance. There are so many photoanodic materials satisfying all the criteria to be the ideal photoanode. But only a few of them are able to perform high water oxidation activity.[34-36] Therefore, it is challenging to design a very high efficient photoelectrochemical photoanode.

In a PEC cell, the improvement in each step should be considered to get a high solar-to-hydrogen (STH) efficiency. It is important to select a semiconductor having suitable band

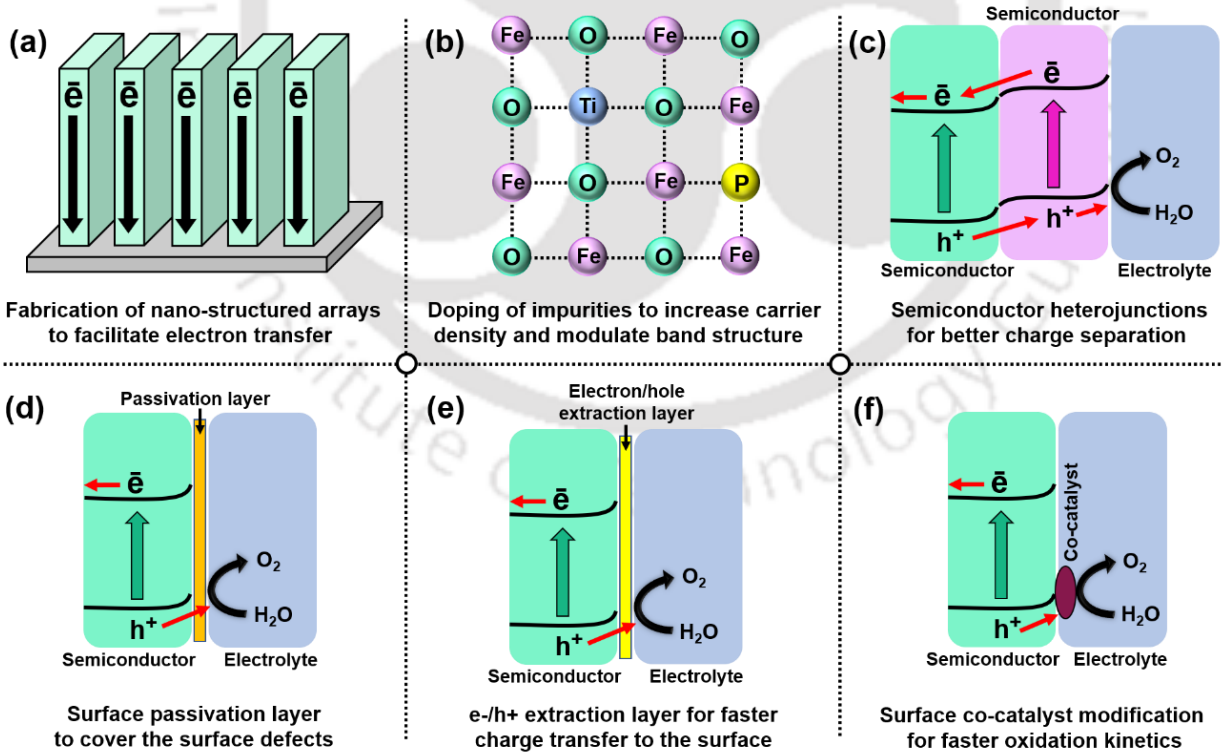

Figure 1.4 Schematics of various strategies to improve the photoanodic efficiency for PEC water oxidation (Reproduced from *Adv. Funct. Mater.* 2019, **29**, 1808032).

alignment, bandgap, and earth abundance for efficient PEC performance. **Figure 1.4** represents the major strategies to maximize the PEC efficacy, i.e., (a)structure engineering, (b) elemental doping, (c) different heterojunctions, (d) surface passivation, (e) hole extraction and (f) co-catalyst modification.

1.4.1 Structure engineering

The minimized recombination of electron-holes enhances the PEC water splitting efficiency. However, the recombination of electrons-holes is very high in the planner surface which leads to the lesser photocurrent. Also, the nanosized mesoporous catalyst doesn't have this necessity because of the presence of a huge number of grain boundaries which perform as carrier trapping sites to enhance the electron-holes recombination rate.[37] Therefore, designing well-organized nanostructured arrays of metal oxide based nanotubes, nanowires, nanorods, nanosheets, nano-cone and nanodots with minimum carrier diffusion length is a feasible approach for minimizing electron-holes recombination.[38] According to reported literatures, one dimensional (1D) nanostructured photoanode of hematite nanotubes,[39] nanobelts,[40] nanowires,[41] nanorods,[42] ZnO nanorods,[43] and TiO_2 nanotubes[44] exhibits boosted PEC water oxidation. Two-dimensional (2D) nanostructured photoanode has a very high surface area which provides better connection and interaction among the photoanodic surface and electrolyte.[45] Also, very thin 2D materials have a shorter hole diffusion length for moving the holes to the surface of the materials.[46] The WO_3 nanosheets,[47] nanoplates,[48] $BiVO_4$ nano-worms,[49] and hematite nanosheets[50,51] show efficient PEC activity by maximizing the charge carrier's separation and transportation. Three-dimensional (3D) materials have the advantage of reducing overpotential for better catalytic activity, efficient light harvesting, and greater interfacial interactions between the photoanode and the electrolyte.[52] The 3D normal spinel structured $ZnFe_2O_4$,[53] TiO_2 nano-tunnels,[54] hematite urchin-like structure[55] provide better PEC performances. Hence, structure engineering of photoanode offers high charge separation and transportation by reducing carrier diffusion length and large interfacial interactions between the catalyst and electrolyte.[56]

1.4.2 Elemental doping

The engineering of photoanodes through elemental doping offers improved optical and electrical features by producing intrinsic defects. As per experimental and theoretical studies, the doping of elements with anionic or cationic phase to the metal oxide semiconductor tunes the band

alignments and bandgap, which regulate the light absorption range, charge carrier density, electrical conductivity, growth orientation, crystallinity, shape, and Size.[57-63] The elemental doping can be done by two different processes, i.e., *in-situ* or *ex-situ*. In general, *in-situ* doping provides uniformity of the dopants throughout the surface of the photoanode, and in *ex-situ* doping, the concentration of dopants reduces gradually from the outer surface to the bulk area.[64,65] As the WO_3 photoanode has a very low carrier density, transition metal dopants such as Zn, Ag, Bi, Ti, Te, Fe, Gd, Ta, Cu, Ce, Mo, and Ni have been used with WO_3 catalyst for boosted PEC performance.[66-71] Doping in $BiVO_4$ film tunes the band alignment, morphology and electron-holes separation of the photoanode.[72] The charge carrier concentration is directly and inversely proportional to the bend bending and depletion layer width, respectively.[73] Also, the optimization of dopant concentration is crucial for high PEC efficacy because the high concentration of dopant leads to high numbers of recombination centers.[74]

1.4.3 Semiconductor heterojunctions

In the PEC system, the internal driving force of a single material is not sufficient for efficient charge carrier separation and transportation, which indicates the need of an external driving force for better performance. Designing of heterojunction among two or more semiconductors needs to have suitable band alignments for a wide range of light harnessing and better charge separation with lower charge recombination in comparison to the single one. These heterojunctions form a built-in electric field, the main driving force to separate the photogenerated electrons-holes efficiently.[75] The combination of two n-type materials forms an n-n heterojunction and the CB of the semiconductor, nearer to the electrolyte, has to be higher than the CB of the other one. $WO_3/BiVO_4$,[76-78] WO_3/Fe_2O_3,[79] $ZnO/BiVO_4$,[80] and Fe_2O_3/Fe_2TiO_5[81] are some of the well-known n-n heterojunctions for efficient PEC water oxidation. Similarly, in p-n heterojunctions, the p-type semiconductor should be present at the electrolyte side. The p-n heterojunctions such as p-Cu_2O/n-$BiVO_4$,[82] p-NiO/n-Fe_2O_3,[83] p-$CuBi_2O_4$/n-$BiVO_4$[84] and p-Co_3O_4/n-Fe_2O_3[85] have been explored for high PEC performance. Another heterojunction approach is the Z-scheme which involves the combination of electrons from the CB of one semiconducting material with the holes from the VB of another one. ZnO/Au/SnO_2[86] and Se/$BiVO_4$[87] are the Z-scheme approaches related to efficient interfacial charge transfer. Homojunctions of WO_{3-x}/WO_3, Zn:$BiVO_4$/Mo:$BiVO_4$, and Mg-Fe_2O_3/P-Fe_2O_3 are also studied for high charge separation due to the elimination of lattice mismatch and the formation of the built-in electric field.[88-90]

1.4.4 Surface passivation

Surface defect, creating the electron-holes recombination at the photoanode-electrolyte interface, is a major limitation of the photoanodes for PEC activity.[91] The surface passivation through the incorporation of a thin oxide overlayer can eliminate the surface defects for extracting the charge carriers to the interface of photoanode-electrolyte.[92] However, the optimization of the thickness of the overlayer is crucial for higher efficiency. As the crystal boundary of the semiconductor causes surface defects, the oxide layer of minimal thickness with amorphous nature is known to be highly operative for surface passivation. A very thin overlayer of Al_2O_3, ZnO, Ga_2O_3 and TiO_2 were analyzed to reduce the surface defects.[93-95] An interaction between the semiconductor and overlayer release the lattice strain from the semiconductor and recombination of charge carriers at the surface.[94] Hence, the surface passivation minimizes the recombination at the photoanodic surface and also protects from corrosion and chemical dissolution.

1.4.5 Co-catalyst modification

In a PEC cell, thermodynamically controlled high energy consuming anodic water oxidation is more critical over the kinetically controlled cathodic water reduction, which indicates the poor kinetics at the interface of photoanode-electrolyte. The incorporation of oxygen evolution catalyst over the photoanode, simply called "co-catalyst modification", minimizes the overpotential and charge carrier's recombination, faster the oxidation kinetics at the interface of photoanode-electrolyte and maximizes the photoanodic durability. Metal oxides such as RuO_2 and IrO_2 are some of the efficient oxygen evolution co-catalysts (OECs); however, they are less appropriate for practical application because they are low earth-abundance and high-cost materials.[96] Among various OECs, cobalt oxides have been a promising co-catalyst for water oxidation at neutral pH.[97,98] The major advantage of Co-Pi is that it requires lower overpotential for water oxidation at neutral conditions. Also, Ni and Fe-based OECs have been widely analyzed due to their magnificent electrocatalytic performances.[57] More complexed OECs, such as NiFe oxide/hydroxide has been introduced due to its transparency to visible light irradiation. Low-cost layered double hydroxides (LDHs) of metals related to Co, Fe, Mn and Ni are emerging OECs for maximized charge separation and accelerated PEC water oxidation kinetics.[57] New grouping of several metal oxides and hydroxides as OECs needs to be explored for efficient PEC activity.

1.4.6 Electron/hole extraction layer

As per the reported literature, R. van de Krol et al. have noted the ability limitation of OECs due to lacking of hole extraction from the photoanodes, which reduces the thermodynamic driving force.[99] To sort out the above limitation, band bending must be maximized at the interface of the photoanode-electrolyte.[100] K.-S. Choi et al. have inserted a hole extraction layer of FeOOH between the $BiVO_4$ semiconductor and NiOOH co-catalyst to enhance the PEC water oxidation kinetics.[101] K. Domen et al. have incorporated a p-type NiO layer over an n-type $CoO_x/BiVO_4$ photoanode for faster hole extraction by the construction of p-n junction.[102] Recently, Zhang et al. have inserted black phosphorene hole extractor in between $BiVO_4$ semiconductor and the co-catalyst to enhance the PEC performance.[103] Polyaniline, a very thin layer transports the holes easily from $BiVO_4$ to NiOOH co-catalyst for boosted efficiency.[104] In PEC water oxidation, the insertion of hole extractors between semiconductor and OECs finds great attention for high performance. The ability of the hole extractor can also be tuned with different morphologies such as 0D nanosized dots, 2D nanosheets etc.

1.5 MOTIVATION AND OBJECTIVES OF THE PRESENT WORK

$BiVO_4$, WO_3 and Fe_2O_3 are promising metal oxide-based semiconductors for PEC water oxidation having proper band alignments and band gaps related to water oxidation, photo-stability, and earth abundance. However, the reported water oxidation performance remains too poor for commercialization because of insufficient photogenerated electron-holes separation and transportation.[105] These key limiting factors can be shorted out by approaching several methods for high PEC water oxidation performance. The current thesis work approaches to different objectives as follows:

[1] Designing new emerging semiconductors as photoanode for efficient PEC water oxidation.

[2] Synthesis of known photoanodes with different novel nanostructured morphologies for better charge separation, transportation and high surface area.

[3] Fusion of different approaches such as structure engineering, elemental doping, electron and hole extractor modification, heterojunctions and co-catalyst incorporation for stable and efficient photoanodes.

[4] Implementation of less explored supporting materials for known photoanodes having unique properties to make the photoanode more efficient.

[5] Well understanding of above mentioned approaches with proper charge transfer mechanism at several interfaces.

[6] Engineering and fabrication of simple, novel, low-cost, and eco-friendly efficient photoanodic materials.

1.6 REFERENCES

(1) J. Barber *Chem. Soc. Rev.*, 2009, **38**, 185.

(2) *IPCC Panel Reports on Climate Change and Biodiversity*, April 2002.

(3) International Energy Agency (IEA), *Key World Energy Statistics*, 2020.

(4) *World Energy Assessment: Energy and the Challenge of Sustainability*, November 2015.

(5) R. Lindsey, *Climate Change: Atmospheric Carbon Dioxide*, August 2020.

(6) European Environment Agency (EEA), *https://www.eea.europa.eu*

(7) *https://en.wikipedia.org/wiki/2015_United_Nations_Climate_Change_Conference*

(8) S. Yun , Y. Qin , A. R. Uhl , N. Vlachopoulos , M. Yin , D. Li , X. Han and A. Hagfeldt, *Energy Environ. Sci.*, 2018, **11**, 476.

(9) D. J. C. MacKay, *Phil. Trans. R. Soc. A.* 2013, **371**, 20110431.

(10) International Renewable Energy Agency (IRENA), *Future of Solar Photovoltaic Deployment, investment, technology, grid integration and socio-economic aspects*, November 2019

(11) V. Vega-Garita, L. Ramirez-Elizondo, N. Narayan and P. Bauer, *Prog. Photovoltaics*, 2018, **27**, 346.

(12) J. H. Kim, D. Hansora, P. Sharma, J.-W. Jang and J. S. Lee, *Chem. Soc. Rev.*, 2019, **48**, 1908.

(13) S. S. Lam, V. Nguyen, M. T. N. Dinh, D. Q. Khieu, D. D. La, H. T. Nguyen, D. V. N. Vo, R. S. Varma, M. Shokouhimehr, C. C. Nguyen, Q. V. Le and W. Peng. *J. Mater. Chem. A*, 2020, **8**, 10571.

(14) P. Nikolaidis and A. Poullikkas, *Renew. Sust. Energ. Rev.*, 2017, **67**, 597.

(15) F. Dalena, A. Senatore, M. Basile, S. Knani, A. Basile and A. Iulianelli, *Membranes*, 2018, **8**, 98.

(16) International Renewable Energy Agency (IRENA), *Hydrogen from Renewable Power TECHNOLOGY OUTLOOK FOR THE ENERGY TRANSITION*, September 2018.

(17) Baxter , Z. Bian , G. Chen , D. Danielson , M. S. Dresselhaus , A. G. Fedorov , T. S. Fisher , C. W. Jones , E. Maginn , U. Kortshagen , A. Manthiram , A. Nozik , D. Rolison , T. Sands , L. Shi , D. Sholl and Y. Wu , *Energy Environ. Sci.*, 2009, **2**, 559.

(18) C. Ros, T. Andreu and J. R. Morante, *J. Mater. Chem. A*, 2020, **8**, 10625.

(19) L. G. Bloor, R. Solarska, K. Bienkowski, P. J. Kulesza, J. Augustynski, M. D. Symes and L. Cronin, *J. Am. Chem. Soc.*, 2016, **138**, 6707.

(20) F. Decker and S. Cattarin, *PHOTOELECTROCHEMICAL CELLS-Overview in Encyclopedia of Electrochemical Power Sources*, 2009, 1-9.

(21) M. Grätzel, *Nature*, 2001, **414**, 338.

(22) A. J. Bard , A. B. Bocarsly , F. F. Fan , E. G. Walton and M. S. Wrighton , *J. Am. Chem. Soc.*, 1980, **102**, 3671.

(23) J. R. Bolton , S. J. Strickler and J. S. Connolly , *Nature*, 1985, **316**, 495.

(24) S. Chen, D. Huang, P. Xu, W. Xue, L. Lei, M. Cheng, R. Wang, X. Liu and R. Deng, *J. Mater. Chem. A*, 2020, **8**, 2286.

(25) W. Yang, R. R. Prabhakar, J. Tan, S. D. Tilley and J. Moon, *Chem. Soc. Rev.*, 2019, **48**, 4979.

(26) M. Ahmed and G. Xinxin, *Inorg. Chem. Front.*, 2016, **3**, 578.

(27) P. M. Ushasree and B. Bora, *Silicon Solar Cells, in Solar Energy Capture Materials*, 2019,1-55.

(28) J. Li and N. Yu, *Catal. Sci. Technol.*, 2015, **5**, 1360.

(29) R. Asmatulund and W. S. Khan, *Electrospun nanofibers for catalyst applications, Synthesis and Applications of Electrospun Nanofibers*, 2019, 153-173.

(30) L. Yang, H. Zhou, T. Fan and D. Zhang, *Phys. Chem. Chem. Phys.*, 2014, **16**, 6810.

(31) H. Zhou, Y. Qu, T. Zeid and X. Duan, *Energy Environ. Sci.*, 2012, **5**, 6732.

(32) H. Tong, S. Ouyang, Y. Bi, N. Umezawa, M. Oshikiri and J. Ye, *Adv. Mater.*, 2012, **24**, 229.

(33) X. Chen, S. Shen, L. Guo and S. S. Mao, *Chem. Rev.*, 2010, **110**, 6503.

(34) Z. F. Huang, L. Pan, J. J. Zou, X. Zhang and L. Wang, *Nanoscale*, 2014, **6**, 14044.

(35) S. Cho, J. W. Jang, K. H. Lee and J. S. Lee, *APL Materials*, 2014, **2**, 010703.

(36) F. E. Osterloh and B. A. Parkinson, *MRS Bull.* 2011, **36**, 17.

(37) P. Peerakiatkhajohn, J.-H. Yun, S. Wang and L. Wang, *J. of Photonics for Energy*, 2016, **7**, 012006.

(38) F. L. Souza, K. P. Lopes, E. Longo and E. R. Leite, *Phys. Chem. Chem. Phys.*, 2009, **11**, 1215.

(39) T. J. LaTempa, X. Feng, M. Paulose and C. A. Grimes, *J. Phys. Chem. C*, 2009, **113**, 16293.

(40) M. Marelli, A. Naldoni, A. Minguzzi, M. Allieta, T. Virgili, G. Scavia, S. Recchia, R. Psaro and V. D. Santo, *ACS Appl. Mater. Interfaces*, 2014, **6**, 11997.

(41) M. T. Mayer, C. Du and D. Wang, *J. Am. Chem. Soc.*, 2012, **134**, 12406.

(42) Y. Fu, C. L. Dong, Z. Zhou, W. Y. Lee, J. Chen, P. Guo, L. Zhao and S. Shen, *Phys. Chem. Chem. Phys.*, 2016, **18**, 3846.

(43) D. Commandeur, G. Brown, E. Hills, J. Spencer and Q. Chen, *ACS Appl. Nano Mater.*, 2019, **2**, 1570.

(44) A. M. Mohamed, A. S. Aljaber, S. Y. AlQaradawi and N. K. Allam, *Chem. Commun.*, 2015, **51**, 12617.

(45) Y. Hou, Z. Wen, S. Cui, X. Guo and J. Chen, *Adv. Mater.*, 2013, **25**, 6291.

(46) S. Shen, S. A. Lindley, X. Chen and J. Z. Zhang, *Energy Environ. Sci.*, 2016, **9**, 2744.

(47) Y. Liu, L. Liang, C. Xiao, X. Hua, Z. Li, B. Pan andY. Xie, *Adv. Energy Mater.*, 2016, **6**, 1600437.

(48) X. Feng, Y. Chen, Z. Qin, M. Wang and L. Guo, *ACS Appl. Mater. Interfaces*, 2016, **8**, 18089.

(49) Y. Kuang, Q. Jia, H. Nishiyama, T. Yamada, A. Kudo and K. Domen, *Adv. Energy Mater.*, 2016, **6**, 1501645.

(50) P. Peerakiatkhajohn, J.-H. Yun, H. Chen, M. Lyu, T. Butburee and L. Wang, *Adv. Mater.*, 2016, **28**, 6405.

(51) O. Zandi, A. R. Schon, H. Hajibabaei and T. W. Hamann, *Chem. Mater.*, 2016, **28**, 765.

(52) J. R. McKone, E. L. Warren, M. J. Bierman, S. W. Boettcher, B. S. Brunschwig, N. S. Lewis and H. B. Gray, *Energy Environ. Sci.*, 2011, **4**, 3573.

(53) A. G. Hufnagel, K. Peters, A. Müller, C. Scheu, D. Fattakhova-Rohlfing, and T. Bein, *Adv. Funct. Mater.*, 2016, **26**, 4435.

(54) R. Takakura, T. Oshikiri, K. Ueno, X. Shi, T. Kondo, H. Masuda and H. Misawa, *Green Chem.*, 2017, **19**, 2398.

(55) A. G. Tamirat, W.-N. Su, A. A. Dubale, C.-J. Pan, H.-M. Chen, D. W. Ayele, J.-F. Lee and B.-J. Hwang, *J. Power Sources*, 2015, **287**, 119.

(56) Y. Ling and Y. Li, *Part. Part. Syst. Charact.*, 2014, **31**, 1113.

(57) M. Xiao, B. Luo, Z. Wang, S. Wang and L.Wang, *Sol. RRL*, 2020, **4**, 1900509.

(58) X. Shi, S. Siahrostami, G.-L. Li, Y. Zhang, P. Chakthranont, F. Studt, T. F. Jaramillo, X. Zheng and J. K. Norskov, *Nat. Commun.*, 2017, **8**, 701.

(59) J. Liu, C. Liang, H. Zhang, Z. Tian and S. Zhang, *J. Phys. Chem. C*, 2012, **116**, 4986.

(60) M. N. Huda, Y. Yan and M. M. Al-Jassim, *J. Appl. Phys.*, 2011, **109**, 113710.

(61) J. Su, J. Wang, C. Liu, B. Feng, Y. Chen and L. Guo, *RSC Adv.*, 2016, **6**, 101745.

(62) Z. Zhou, P. Huo, L. Guo and O. V. Prezhdo, *J. Phys. Chem. C*, 2015, **119**, 26303.

(63) J. Xie, W. Liu, J. Xin, F. Lei, L. Gao, H. Qu, X. Zhang and Y. Xie, *ChemSusChem*, 2017, **10**, 4465.

(64) R. Asahi, T. Morikawa, T. Ohwaki, K. Aoki and Y. Taga, *Science*, 2001, **293**, 269.

(65) X. Chen and S. S. Mao, *Chem. Rev.*, 2007, **107**, 2891.

(66) T. Zhang, Z. L. Zhu, H. N. Chen, Y. Bai, S. Xiao, X. L. Zheng, Q. Z. Xue and S. H. Yang, *Nanoscale*, 2015, **7**, 2933.

(67) B. Yang and V. Luca, *Chem. Commun.*, 2008, **37**, 4454.

(68) W. Erbs, J. Desilvestro, E. Borgarello, and M. Grätzel, *J. Phys. Chem.*, 1984, **88**, 4001.

(69) Y. Liu, J. Li, W. Li, Y. Yang, Y. Li and Q. Chen, *The Journal of Physical Chemistry C*, 2015, **119**, 14834.

(70) S. S. Kalanur and H. Seo, *J. Colloid Interface Sci.*, 2018, **509**, 440.

(71) S. S. Kalanur, I.-H. Yoo, K. Eom and H. Seo, *J. Catal.*, 2018, **357**, 127.

(72) X. Zhong, H. He, M. Yang, G. Ke, Z. Y. Zhao, F. Dong, B. Wang, Y. Chen, X. Shi and Y. Zhou, *J. Mater. Chem. A*, 2018, **6**, 10456.

(73) G. Wang, Y. Ling, H. Wang, L. Xihong and Y. Li, *J. Photochem. Photobiol C Photochem. Rev.*, 2014, **19**, 35.

(74) X. Zhang, H. Li, S. Wang, F.-R. F. Fan and A. J. Bard, *J. Phys. Chem.*, C 2014, **118**, 16842.

(75) G. Yun, M. Balamurugan, H.-S. Kim, K.-S. Ahn and S. H. Kang, *J. Phys. Chem. C*, 2016, **120**, 5906.

(76) P. M. Rao, L. Cai, C. Liu, I. S. Cho, C. H. Lee, J. M. Weisse, P. Yang and X. Zheng, *Nano Lett.*, 2014, **14**, 1099.

(77) J. H. Seo, G. Park, K. H. Oh, S. H. Kang, H. C. Lee, S. K. Cho and K. M. Nam, *J. Electroanal. Chem.*, 2017, **789**, 17.

(78) S. Y. Chae, C. S. Lee, H. Jung, O.-S. Joo, B. K. Min, J. H. Kim and Y. J. Hwang, *ACS Appl. Mater. Interfaces*, 2017, **9**, 23, 19780.

(79) Y. Li, L. Zhang, R. Liu, Z. Cao, X. Sun, X. Liu and J. Luo, *ChemCatChem*, 2016, **8**, 2765.

(80) J.-S. Yang and J.-J. Wu, *Nano Energy*, 2017, **32**, 232.

(81) C. Li, T. Wang, Z. Luo, S. Liu and J. Gong, *Small*, 2016, **12**, 3415.

(82) S. Bai, J. Liu, M. Cui, R. Luo,J. He and A. Chen, *Dalton Trans.*, 2018, **47**, 6763.

(83) A. K. Singh and D. Sarkar, *Nanoscale*, 2018, **10**, 13130.

(84) S. Liu, J. Zhou, Y. Lu and J. Su, *Sol. Energy Mater. Sol. Cells*, 2018, **180**, 123.

(85) S. -S. Yi, B. -R. Wulan, J. -M. Yan and Q, Jiang, *Adv. Funct. Mater*, 2019, **29**, 1801902.

(86) J. M. Li, H. Y. Cheng, Y. H. Chiu and Y. J. Hsu, *Nanoscale*, 2016, **8**, 15720.

(87) S. N. F. M. Nasir, H. Ullah, M. Ebadi, A. A. Tahir, J. S. Sagu and M. A. M. Teridi, *J. Phys. Chem. C*, 2017, **121**, 6218.

(88) F. Zhan, Y. Liu, K. Wang, X. Yang, M. Liu, X. Qiu, J. Li and W. Li, *ACS Appl. Mater. Interfaces*, 2019, **11**, 39951.

(89) J. M. Lee, J. H. Baek, T. M. Gill, X. Shi, S. Lee, I. S. Cho, H. S. Jung and X. Zheng, *J. Mater. Chem. A*, 2019, **7**, 9019.

(90) F. Li, J. Li, F. Li, L. Gao, X. Long, Y. Hu, C. Wang, S. Wei, J. Jin and J. Ma, *J. Mater. Chem. A*, 2018, **6**, 13412.

(91) M. J. Kenney, M. Gong, Y. Li, J. Z. Wu, J. Feng, M. Lanza and H. Dai, *Science* 2013, **342**, 836.

(92) Y. Hou, F. Zuo, A. Dagg and P. Feng, *Nano Lett.*, 2012, **12**, 6464.

(93) F. L. Formal, M. Gr¨atzel and K. Sivula, *Adv. Funct. Mater.*, 2010, **20**, 1099.

(94) T. Hisatomi, J. Brillet and M. Cornuz, *Faraday Discuss.*, 2012, **155**, 223.

(95) T. Hisatomi, H. Dotan and M. Stefik, *Adv. Mater.*, 2012, **24**, 2699.

(96) C. Jiang, S. J. A. Moniz, A. Wang, T. Zhang and J. Tang, *Chem. Soc. Rev.*, 2017, **46**, 4645

(97) A. Kay, I. Cesar and M. Grätzel, *J. Am. Chem. Soc.*, 2006, **128**, 15714.

(98) M. W. Kanan and D. G. Nocera, *Science*, 2008, **321**, 1072.

(99) C. Zachäus, F. F. Abdi, L. M. Peter and R. van de Krol, *Chem. Sci.*, 2017, **8**, 3712.

(100) B. J. Trześniewski, I. A. Digdaya, T. Nagaki, S. Ravishankar, I. Herraiz-Cardona, D. A. Vermaas, A. Longo, S. Gimenez and W. A. Smith, *Energy Environ. Sci.*, 2017, **10**, 1517.

(101) T. W. Kim and K.-S. Choi, *Science*, 2014, **343**, 990.

(102) M. Zhong, T. Hisatomi, Y. Kuang, J. Zhao, M. Liu, A. Iwase, Q. Jia, H. Nishiyama, T. Minegishi, M. Nakabayashi, N. Shibata, R. Niishiro, C. Katayama, H. Shibano, M. Katayama, A. Kudo, T. Yamada and K. Domen, *J. Am. Chem. Soc.*, 2015, **137**, 5053.

(103) K. Zhang, B. Jin, C. Park, Y. Cho, X. Song, X. Shi, S. Zhang, W. Kim, H. Zeng and J. H. Park, *Nat. Commun.*, 2019, **10**, 2001.

(104) X. Wang, K.-H. Ye, X. Yu, J. Zhu, Y. Zhu and Y. Zhang, *J. Power Sources*, 2018, **391**, 34.

(105) A. Fujishima and K. Honda, *Nature*, 1972, **238**, 37.

CHAPTER 2

Experimental Section

This chapter defines the basics of instrumental methods and procedures for material characteristic analysis and device fabrications. Also, a brief overview of parameters related to photoelectrochemical analysis and electrochemical impedance spectroscopy is provided.

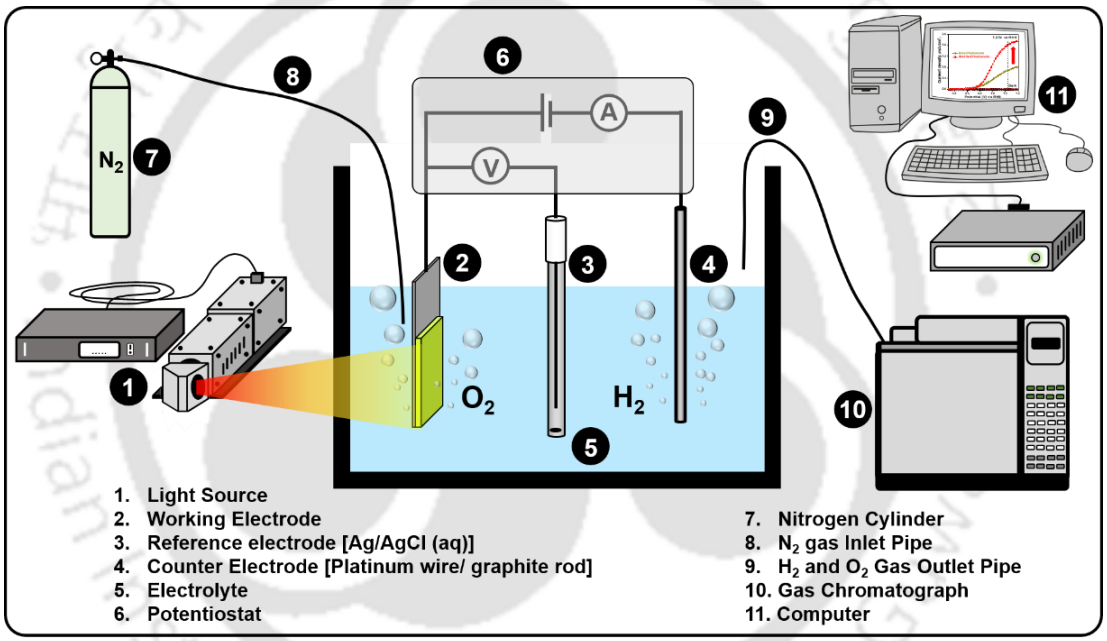

2.1 INTRODUCTION

This chapter covers the discussions of material synthesis, fabrications and characterizations for PEC water oxidation. The chemicals and materials related to the above synthesis and fabrication processes have been listed. All characterization techniques related to materials analysis have been mentioned. The PEC measurements along with the experimental set up have also been discussed. The crucial PEC techniques have been discussed briefly for better understanding.

2.2 CHEMICALS AND REAGENTS USED

Fluorine doped tin oxide (FTO) conducting substrate (Sigma Aldrich), sodium tungstate dihydrate ($Na_2WO_4 \cdot 2H_2O$) (Sigma Aldrich), ammonium oxalate monohydrate ($(NH_4)_2C_2O_4 \cdot H_2O$) (Himedia), sodium sulphate anhydrous (Na_2SO_4) (Merck), indium (III) chloride ($InCl_3$) (Sigma Aldrich), melamine ($C_3H_6N_6$) (Sigma Aldrich), boric acid (Merck), phosphonitrilic chloride trimer (PCT) (Sigma Aldrich), boron powder (Sigma Aldrich), N N-Dimethylformamide (N,N′-DMF) (Sigma Aldrich), potassium iodide (KI) (Merck), bismuth nitrate pentahydrate ($Bi(NO_3)_3 \cdot 5H_2O$) (Sigma Aldrich), p-benzoquinone (Sigma Aldrich), nitric acid (Merck), vanadyl acetylacetonate ($VO(acac)_2$) (Sigma Aldrich), dimethyl sulfoxide (DMSO) (Merck), hexagonal boron nitride (h-BN) powder (Sigma Aldrich), cobalt(II) nitrate hexahydrate ($Co(NO_3)_2 \cdot 6H_2O$) (Sigma Aldrich), chromium(III) nitrate nonahydrate ($Cr(NO_3)_3 \cdot 9H_2O$) (Loba Chemie), urea (Merck) and ammonium fluoride (NH_4F) (Sigma Aldrich). All the analytical chemicals and reagents have been used for synthesis and fabrication without any purification. For the synthesis protocol, we have used Mili-Q water of 18.2 MΩ-cm.

2.3 CHARACTERIZATION OF AS-SYNTHESIZED MATERIALS AND PHOTOELECTROCHEMICAL DEVICES

The characterizations of all the synthesized materials for PEC water oxidation have involved various instruments as follows:

[1] To identify the crystalline structure and phase purity of the synthesized materials, X-ray diffraction (XRD) analysis were carried out by Rigaku SmartLab 9 kW (Cu Kα light source, λ =1.54 Å) having 0.5 °/sec scanning speed.

[2] The UV-Vis absorption spectra were characterized on Shimadzu UV-2600, JASCO Model V-650 and PerkinElmer Lambda 750 UV/VIS/NIR spectrophotometers at room temperature by taking reference of $BaSO_4$.

[3] The Fourier transform infrared (FTIR) analysis was carried out in PerkinElmer Spectrum Two instrument using KBr pellets.

[4] The photoluminescence (PL) measurements were performed by Horiba−Jobin Yvon Fluoromax-4 and Horiba Scientific Fluoromax-4 spectrophotometers.

[5] Time-resolved photoluminescence (TRPL) analysis were performed through Edinburg Lifespec II Instrument.

[6] The field emission scanning electron microscopy (FESEM) related morphological features of the photoanodes were studied by Zeiss Sigma-300 instrument with 5 kV operating voltage.

[7] Field emission transmission electron microscopy (FETEM) related all analysis were performed through JEOL JEM 2100F microscope with 200 kV operating voltage.

[8] X-ray spectroscopy (EDS) analysis for elemental and compositional study were analyzed by INCA, Oxford instruments.

[9] The X-ray photoelectron spectroscopy (XPS) analysis were measured through Omicron Nano Technology instrument with Al K_α irradiation and Thermo-Fisher Scientific photoelectron spectrometer (ESCALAB Xi+) equipped with X-ray source ($h\nu$ = 1486.6 eV) of a monochromatized Al-K_α.

[10] The real surface and roughness analysis were characterized through the atomic force microscope (AFM) instrument of Asylum Cypher, Oxford Instruments.

[11] To know the surface charge of the synthesized material, the zeta potential analysis was recorded on Malvern Nano-ZS90 ZETASIZER instrument.

[12] The PEC measurements such as linear sweep voltammetry (LSV), chronoamperometry and cyclic voltammetry (CV) measurements were analyzed on the CH-instrument of model CHI1120B and GAMRY INTERFACE 1010 E potentiostat.

[13] The incident photon to current efficiency (IPCE) analysis was obtained from Newport Oriel IQE-200 instrument having a quartz tungsten halogen lamp of 250 W.

[14] Electrochemical impedance spectroscopy (EIS) and Mott−Schottky (MS) analysis were performed through the CH-instrument of model CHI760D and GAMRY INTERFACE 1010 E potentiostat.

2.4 PHOTOELECTROCHEMICAL MEASUREMENTS

The LSV, chronoamperometry and CV measurements of the photoanodes were analyzed through the potentiostat of CHI1120B and GAMRY INTERFACE 1010 E by using a three-electrode system. A neutral medium pH = 6 maintained 0.1 M Na_2SO_4 aqueous electrolyte, purged with N_2 gas for 30 min was used for all PEC measurements. A standard three-electrode setup having fabricated thin-films as the working electrode, Ag/AgCl electrode as reference electrode and platinum wire or graphite rod as the counter electrode was used for the PEC analysis. The measured potentials alteration from Ag/AgCl to reversible hydrogen electrode (RHE) scale can be signified as:[1]

$$E_{RHE} = E_{Ag/AgCl} + 0.059pH + E°_{Ag/AgCl} \quad \ldots\ldots\ldots\ldots\ldots\ldots \quad (2.1)$$

Where E_{RHE}, $E°_{Ag/AgCl}$ are the potentials against RHE and reference Ag/AgCl electrode, respectively and pH indicates the pH of electrolyte. The PEC measurements were analyzed under tungsten halogen lamp with power equivalent to 1 Sun (100 mW/cm^2), Photo Emission Tech., Inc., Model-300WSS-PC and SCIENCETECH (Class AAA) SciSun-300 solar simulators having 1.5 G Air mass filter. The EIS and MS analysis were performed by potentiostat of CHI760D and GAMRY INTERFACE 1010 E. In EIS, the frequency range is maintained from 10,000 Hz to 0.1 Hz. The MS plots were recorded under dark conditions in DC potential range, i.e., from -1 to +1 V vs Ag/AgCl. Online gas chromatography (GC) for Faradaic yield of hydrogen and oxygen gas evolution was operated on Agilent 7820A and Nucon 5765 instruments. **Figure 2.1** is the schematic of the complete PEC analysis setup.

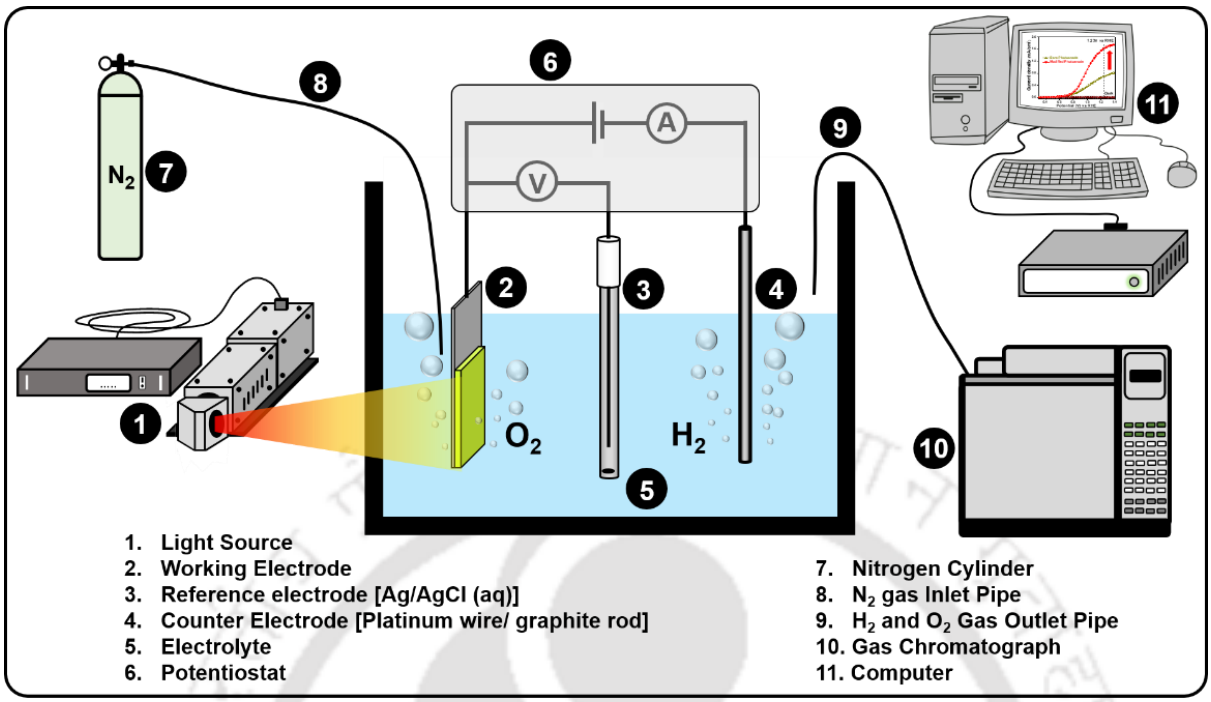

Figure 2.1 Schematic of the experimental setup for PEC water splitting.

2.5 PHOTOELECTROCHEMICAL PERFORMANCE PARAMETERS

2.5.1 Incident photon-to-current conversion efficiency (IPCE)

The IPCE analysis is very crucial to analyze the quantum efficiency of the PEC device. The conversion of incident photons to photocurrent as a function of wavelength by a photoelectrode is known as IPCE and it can be represented as follows:[2]

$$\mathrm{IPCE} = 1240 \times \frac{J_{SC}}{\lambda \times \mathrm{P}_{\mathrm{mono}}(\lambda)} \text{.........................} \quad (2.2)$$

Where J_{SC} is the photocurrent density, λ is the wavelength of light, P_{mono} is the light intensity at each wavelength.

2.5.2 Faradaic yield

The Faradaic yield of a catalyst indicates the transported charge carrier's percentage for H_2 and O_2 gas generation during the electrochemical process. The quantification of H_2 and O_2 gas generation is needed for Faradaic yield. Faradaic yield is the comparison between the real amount of evolved gases and the expected amount of evolved gases based on the total transportation of charge carriers throughout the water splitting process. The Faradaic yield equations for H_2 and O_2 gas generation are as follows: [3,4]

$$\text{FE of } O_2(\%) = \frac{4\times n_{O_2}\,(\text{mol})\times F\,(\text{C mol}^{-1})}{\text{Charge passed through working electrode (C)}} \quad \ldots\ldots\ldots\ldots\ldots\ldots\ldots\ldots \quad (2.3)$$

$$\text{FE of } H_2(\%) = \frac{2\times n_{H_2}\,(\text{mol})\times F\,(\text{C mol}^{-1})}{\text{Charge passed through working electrode (C)}} \quad \ldots\ldots\ldots\ldots\ldots\ldots\ldots\ldots \quad (2.4)$$

The calculation for charge carriers, passed through working electrode can be expressed as follows:

$$\text{Charge passed through working electrode (C)} = (\text{photocurrent (A)} \times \text{time(t)}) \ldots\ldots\ldots \quad (2.5)$$

The photocurrent density is J_{SC} (A cm^{-2}), the analysis time period is t (sec), the illumination area on the photoelectrode is A (cm^2), the electronic charge is C (1.602×10^{19} C) and the Avogadro's number is N_A (6.02×10^{23} mol^{-1}). Gas chromatography (GC) is used to quantify the amount of evolved O_2 and H_2 gas.[2]

2.6 ELECTROCHEMICAL IMPEDANCE SPECTROSCOPY (EIS) MEASUREMENTS

The parameters such as conductivity and resistivity of a PEC cell indicate the charge transfer behaviors inside the electrical circuit. These parameters can be obtained from EIS analysis, which helps to understand the reaction mechanism at the surface of the photoelectrode. Generally, EIS analysis is carried out under bias potential in an electrolyte solution.

2.6.1 Nyquist plots

In EIS analysis, a perturbation is applied to the photoelectrode through a small amplitude based sinusoidal signal at a certain bias and the response is recorded. An alternating current (AC) signal of variable frequencies (from 0.1 Hz to 10^6 Hz) is applied to the system and the corresponding current density of the photoelectrode is noted. In the Nyquist plot, the X-axis represents real impedance (Z') and the Y-axis represents imaginary impedance (Z'').[5] In general, a Nyquist plot has two regions, i.e., high and low-frequency regions (**Figure 2.2(a)**). The high-frequency region indicates the mass transfer process at the bulk of the photoanode and the low-frequency region indicates the charge transfer process at the interface of photoelectrode-electrolyte.[6] In some cases, more than one semicircle can be possible, which attributes the multiple step based charge carrier transfer through reaction intermediates or surface states. The electrode, electrolyte properties and other PEC conditions can affect the shape of the Nyquist plot.[7] All the

Nyquist plot parameters can be fitted with an equivalent circuit model (inset of **Figure 2.2(a)**). The equivalent circuit model comprises series resistance (R_s), bulk charge trapping resistance (R_{trap}) and photoelectrode/electrolyte charge transfer resistance (R_{ct}), trap-state capacitance (C_{trap}) and space-charge depletion region capacitance (C_{bulk}).[8]

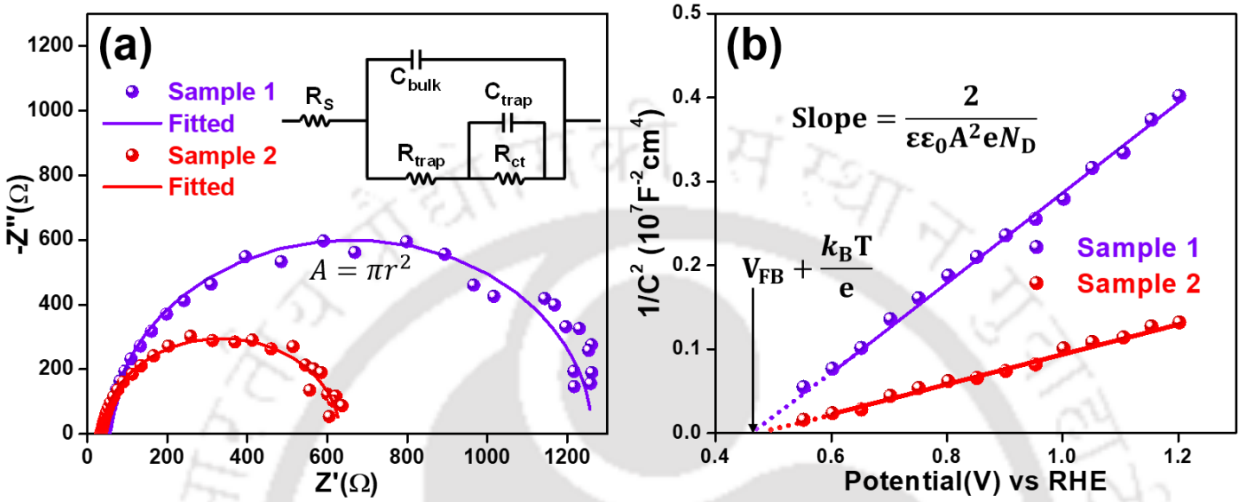

Figure 2.2 (a) Nyquist plots along with equivalent circuit model to interpret the EIS data and (b) Mott-Schottky plots of the materials.

2.6.2 Mott-Schottky (MS) plots

In general, the widely used Mott-Schottky plots follow the Mott-Schottky theory, which provides qualitative data about the charge transport properties and charge carrier density of the semiconductor. The flat band potential (E_{FB}) is another crucial parameter which represents the potential at which the potential drop in between the bulk and surface of the electrode is zero (**Figure 2.2(b)**). It obtains the band positions of semiconductors w.r.t. the redox potential of the electroactive materials in the electrolyte solution. The E_{FB} and the total charge carrier density (N_D) of the photoelectrode can be obtained from Mott–Schottky equation as mentioned in **equation 2.6**:[9,10]

$$\frac{1}{C^2} = \frac{1}{A^2 N_D e \varepsilon \varepsilon_0}\left[E - E_{FB} - \frac{kT}{e}\right] \quad \text{..... (2.6)}$$

The exposed surface area, dielectric constant and capacitance of the photoelectrode are A, ε and C, respectively. The permittivity of the vacuum is ε_0, the applied bias is E, the Boltzmann constant is k, the temperature is T and the charge of an electron is e.

2.7 CHARGE SEPARATION AND INJECTION EFFICIENCIES

The charge separation efficiency (η_{sep}) and charge injection efficiency (η_{inj}) of the photoanode can be determined from the hole scavenger (HS) test of the photoanode. In general, HSs remove the interfacial hole transfer barrier through scavenging photogenerated holes and transfer to the outer surface of the photoanode for high PEC water oxidation activity.[11] HS test is performed by adding hole scavenger to the electrolyte with a proper ratio under 1 Sun illumination. Different types of HSs such as acidic, neutral and basic medium HSs related to the pH of the corresponding electrolyte are used in PEC water oxidation. The photocurrent density arising from water splitting (J_{H_2O}), η_{sep}, and η_{inj} in the presence of HS can be described as follows:[11]

$$J_{H_2O} = J_{abs} * \eta_{sep} * \eta_{inj} \quad \text{..... (2.7)}$$

$$\eta_{sep} = \frac{J_{HS}}{J_{abs}} \quad \text{..... (2.8)}$$

and

$$\eta_{inj} = \frac{J_{H_2O}}{J_{HS}} \quad \text{..... (2.9)}$$

where J_{abs} is the photocurrent density of photoanode at complete conversion of absorbed photon to current. J_{H_2O} and J_{HS} are the photocurrent densities obtained in electrolytes without and with hole scavengers, respectively.

2.8 REFERENCES

(1) C. Miao, T. Shi, G. Xu, S. Ji and C. Ye, *ACS Appl. Mater. Interfaces*, 2013, **5**, 1310.

(2) C. Jiang, S. J. A. Moniz, A. Wang, T. Zhang and J. Tang, *Chem. Soc. Rev.*, 2017, **46**, 4645.

(3) J. H. Kim, D. Hansora, P. Sharma, J.-W. Jang and J. S. Lee, *Chem. Soc. Rev.*, 2019, **48**, 1908.

(4) Z. Chen, H. Dinh and E. Miller, *Photoelectrochemical Water Splitting*, Springer, 2013.

(5) X.-T. Xu, L. Pan, X. Zhang, L. Wang and J.-J. Zou, *Adv. Sci.*, 2019, **6**, 1801505.

(6) A. J. Bard, L. R. Faulkner, J. Leddy and C. G. Zoski, *Electrochemical Methods: Fundamentals and Applications*, Wiley, 1980.

(7) C. Cao and J. Zhang, *An Introduction to Electrochemical Impedance Spectroscopy*, Science Press, 2002.

(8) B. Klahr, S. Gimenez, F. Fabregat-Santiago, T. Hamann and J. Bisquert, *J. Am. Chem. Soc.*, 2012, **134**, 4294.

(9) C. Adel, B. M. Fethi and B. Brahim, *Appl. Phys. A: Mater. Sci. Process.*, 2016, **122**, 62.

(10) H. Dotan, K. Sivula, M. Grätzel, A. Rothschild and S. C. Warren, *Energy Environ. Sci.*, 2011, **4**, 958.

(11) R. Zhang, Y. Fang, T. Chen, F. Qu, Z. Liu, G. Du, A. M. Asiri, T. Gao and X. Sun, *ACS Sustainable Chem. Eng.*, 2017, **5**, 7502–7506.

CHAPTER 3

Electronic structure modulations of monoclinic tungsten oxide nanoblocks by indium doping for boosted photoelectrochemical performance

This chapter offers the hydrothermal fabrication of In-doped monoclinic WO_3 nanoblocks directly over fluorine-doped tin oxide (FTO) substrate without the aid of any seed layer. The In^{3+} ions are partially occupying the W^{6+} ions in the In-doped WO_3 photoanode and offering better performance by adding additional charge carriers for amplifying the expression of the number of carriers.

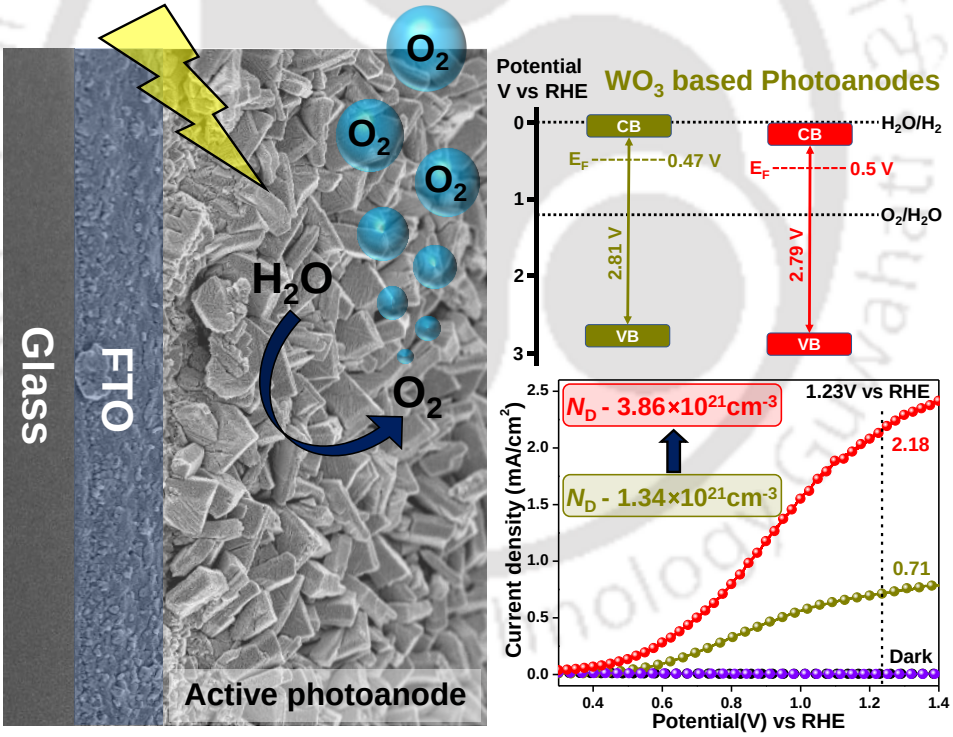

CHEMISTRY AN ASIAN JOURNAL
ACES Asian Chemical Editorial Society
WILEY-VCH

M.K. Mohanta *et al.*, 2020, **15**, 3886

3.1 INTRODUCTION

Monoclinic tungsten trioxide (WO_3) is familiar as a superior n-type metal oxide semiconductor for PEC water oxidation in recent years because of its suitable band gap (~ 2.7eV) for better light-harvesting, excellent hole mobility of around 10 cm^2 V^{-1} s^{-1}, average diffusion length (~150 nm) and stability in acidic and neutral.[1-3] However, experimental PEC water oxidation activities for bare WO_3 are not significant compared to its theoretical efficiency due to its low carrier density, poor charge separation with undesired charge recombination, and slower oxygen evolution kinetics.[4,5] Different modifications such as surface and structural engineering of semiconductors, heterojunction strategy, quantum dots incorporation for charge collection, overlayer deposition, and selective doping of metal ions are applied to get better PEC water oxidation efficiency.[6-9] The effect of metal or non-metal dopants on pristine WO_3 photoanodes induces PEC water oxidation activities by tuning band structure and better charge collection.[10,11] Transition metals such as Zn, Ti, Te, Ta, Cu, Ag, Ce, Mo, Ni, Fe, Bi, Gd have already been analyzed as dopants with bare WO_3 thin film.[2,12-16] According to recent studies, the semiconductor $BiVO_4$ has been doped with In^{3+} metal ions for enhancement of PEC activities by surface state passivation.[17] In this work, we have analyzed the effect of In-doping on bare monoclinic WO_3 photoanode to get higher PEC water oxidation efficacy. Monoclinic WO_3 nanoblocks were synthesized hydrothermally by in-situ method, which were grown over FTO directly without deposition of any seed layer. The ionic radius of In^{3+} is 0.8 Å, which is similar for doping at tungsten site of WO_3 with ionic radii of 0.74 Å for W^{6+}.

3.2 EXPERIMENTAL METHODS

3.2.1 Synthesis of In-doped WO_3 and pristine WO_3 nanoblocks photoanode

WO_3 thin-films with nanoblock features were synthesized hydrothermally.[18] Firstly, 0.124 g of sodium tungsten dihydrate ($Na_2WO_4 \cdot 2H_2O$) was dissolved in a beaker containing 15 mL of deionized water. The precursor solution was stirred for 30 min at room temperature. In another beaker, ammonium oxalate monohydrate ($(NH_4)_2C_2O_4 \cdot H_2O$) of amount 0.117 g was dissolved in 15 mL of deionized water and stirred for 30 min at room temperature. After 30 min of stirring, 5 mL of 3 M HCl was added dropwise to the tungsten precursor solution to get a white precipitated solution. Then, ammonium oxalate precursor solution was added to the tungsten precursor solution with continuous stirring. The white precipitated solution was become colorless after few minutes

Part of this chapter has been published in **Chem Asian J. 2020, 15, 3886**.

of stirring. A specific amount of indium(III) chloride ($InCl_3$) was added to that mixture precursor solution with continuous stirring up to 1 hour. After 1 hour of stirring, the final mixture solution was transferred to a Teflon-lined stainless steel autoclave. Two pieces of ozonized conducting fluorine doped tin oxide (FTO) glass substrates, cleaned with acetone, isopropanol and deionized water were placed inside the Teflon vessel by facing the conducting side down. Then, the autoclave was placed inside a hot air oven for 8 h at 140 °C. After completion of the hydrothermal reaction, the in-situ grown WO_3 thin films on the FTO surface were removed from the vessel, cleaned with deionized water and dried in a vacuum oven for 30 min at 60 °C. Dried WO_3 thin films were calcined in a muffle furnace at 500 °C for 1 hour to get monoclinic WO_3 thin film. For comparison, we have used different weight percent of $InCl_3$ (2 wt%, 3 wt%, 4 wt%) by repeating the following procedure. The total synthesis procedure for In-doped WO_3 thin film has been given below in **Scheme 3.2.1** with the graphical for better understanding.

The pristine WO_3 thin films with nanoblocks shape were synthesized using the same procedure described above, without the addition of indium(III) chloride.

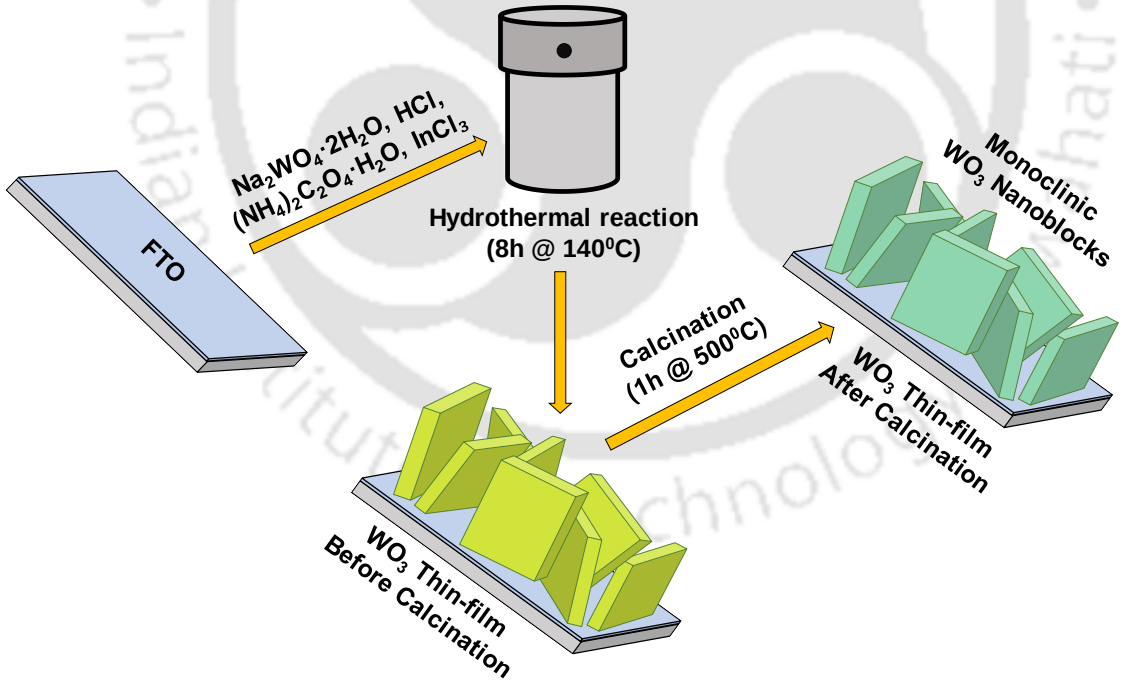

Scheme 3.2.1 Fabrication of in-situ grown In-doped monoclinic WO_3 nanoblocks growing directly over FTO without any seed layer.

Part of this chapter has been published in **Chem Asian J. 2020, 15, 3886**.

3.3 RESULTS AND DISCUSSIONS

3.3.1 Powder x-ray diffraction (XRD) and Rietveld refinement analysis

Figure 3.3.1(a) represents the XRD patterns of pristine WO_3 and In-doped WO_3 photoanodes for their crystal structure and phase purity. The monoclinic phase of bare WO_3 photoanode is confirmed by the diffraction peaks, which are matched with the JCPDS card number 01-072-0677.[18] The diffraction peaks for all the modified In-doped WO_3 photoanodes are similar as that of the undoped WO_3 photoanode, which confirms that there is no induced transformation of phase due to In-doping. Microstructure and phase purity of bare WO_3 and modified In-doped WO_3 nanoblocks were well investigated using Rietveld refinement analysis, as shown in **figure 3.3.1(b,c)**. Crystallography open database (COD) with ID number 2106382 having space group $P1\ 2_1/n1$ (a=7.306 Å, b=7.54 Å, c=7.692 Å, α=90°, β=90.881°, γ=90°, cell volume=423.681 $Å^3$) has been used for Rietveld refinement of monoclinic bare WO_3 and In-doped WO_3 nanoblocks by

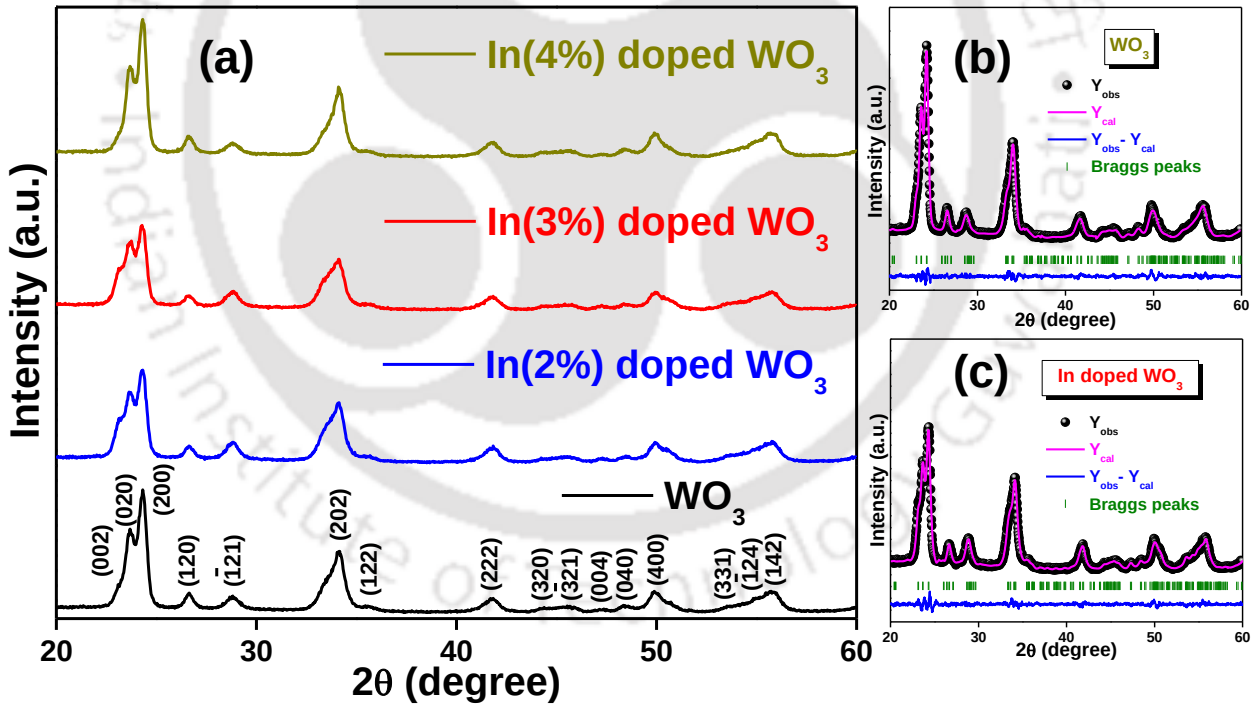

Figure 3.3.1 (a) XRD patterns of pristine WO_3 photoanode with monoclinic phase, and In doped WO_3 photoanodes with varying concentrations of indium (2 wt%, 3 wt%, 4 wt%). Rietveld refinement analysis of (b) undoped monoclinic WO_3 and (c) In-doped monoclinic WO_3. The CIF file containing the necessary parameters of the crystal structure of WO_3 (COD ID 2106382) was achieved from COD database implemented in Fullprof software to simulate the observed XRD patterns using Rietveld refinement.

Part of this chapter has been published in **Chem Asian J. 2020, 15, 3886**.

using Fullprof software. The Rietveld refinement analysis confirmed that the leading diffraction peak of bare WO_3 photoanode (200) has been shifted from θ=24.26° to θ=24.32° for the In-doped modified WO_3 photoanode. All the refined cell parameter values and cell volumes of pristine and In-doped WO_3 nanoblocks are listed below in **table 3.3.1**. The change in cell parameters and cell volume for In-doped WO_3 nanoblocks and bare monoclinic WO_3 nanoblocks confirms the shifting of diffraction peaks for In-doped WO_3 towards higher 2θ values. The overall crystal phase (monoclinic) and the space group ($P1\ 2_1/n1$) for both bare and modified WO_3 nanoblocks remained the same (**table 3.3.1**).

Table 3.3.1 Rietveld refined powder XRD data of bare and modified In-doped WO_3 nanoblocks.

Photoanode	a (Å)	b (Å)	c (Å)	α	β	γ	Volume (Å^3)	R_{wp}	R_{ex}	χ^2
WO_3	7.35	7.54	7.72	90°	89.15°	90°	427.50	8.39	6.11	1.89
In-doped WO_3	7.32	7.52	7.69	90°	90.70°	90°	422.99	7.53	5.66	1.77

3.3.2 UV-visible absorption spectra and Tauc plots

Figure 3.3.2(a) represents the normalized UV-Visible absorption spectra for undoped and In-doped WO_3 photoanodes. These spectra confirm the effect of optical absorption properties of WO_3 thin film by In-doping. The absorption edge of the bare and modified photoanodes were recorded at 460 nm, which are well-matched with the reported literature.[19] Tauc plots for both bare and optimized In-doped photoanodes were plotted on the basis of UV-Visible absorption spectra (**figure 3.3.2(b)**). The band gap values for bare monoclinic WO_3 and In-doped WO_3 thin films were calculated to

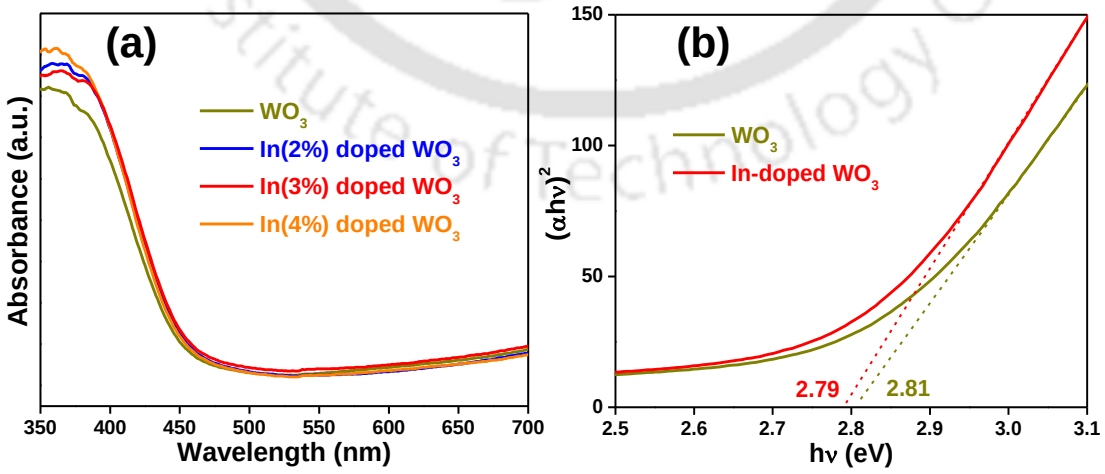

Figure 3.3.2 (a) Normalized UV-Visible absorption spectra for undoped and In-doped WO_3 photoanodes; (b) Tauc plots of bare WO_3 and optimized In-doped WO_3 photoanodes in addition to their energy band gaps.

Part of this chapter has been published in **Chem Asian J. 2020, 15, 3886**.

be 2.81 eV and 2.79 eV, respectively. The required amount of overpotential was weakened slightly due to the reduced energy band gap, which helps in amplifying photogenerated charge separation for higher efficacy.

3.3.3 Materials morphology

Morphological and elemental analysis of pristine monoclinic WO_3 and the modified In-doped WO_3 nanoblocks were carried out by the FESEM and EDX analysis (**figure 3.3.3**). **Figure 3.3.3(a)** (bare WO_3) and **figure 3.3.3(b)** (In-doped WO_3) show the enlarged FESEM images, which confirms the uniformly grown nanoblock shape of both bare and the modified WO_3 photoanodes over the FTO surface. **Figure 3.3.3(c)** represents the cross-sectional view of modified In-doped WO_3 thin film, which illustrates the vertical growth of WO_3 nanoblocks over the FTO surface. The shape and size of both bare and modified photoanodes are similar, having an average edge length of 800 nm to 1 μm.

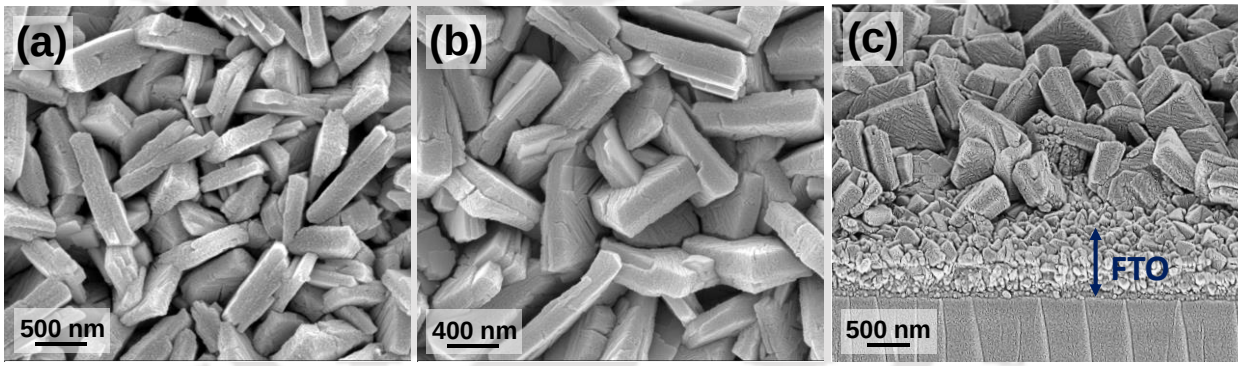

Figure 3.3.3 FESEM images of (a) WO_3 nanoblocks (b) In-doped WO_3 nanoblocks directly grown over FTO by in situ method without deposition of any seed layer and (c) cross-sectional view of In-doped WO_3 thin film.

Since doping of foreign elements forms the basis of the present study, we have validated an accurate percentage of In dopant in the In-doped WO_3 thin films using FESEM-EDX analysis of bare WO_3 and other In-doped WO_3 photoanodes (**figure 3.3.4**). From EDX data, the values of 0.0 wt% (0.0 At%), 0.6 wt% (0.3 At%), 0.9 wt% (0.5 At%) and 1.1 wt% (0.6 At%) Indium were found for bare WO_3, In(2%)-doped WO_3, In(3%)-doped WO_3 and In(4%)-doped WO_3 respectively.

Part of this chapter has been published in **Chem Asian J. 2020, 15, 3886**.

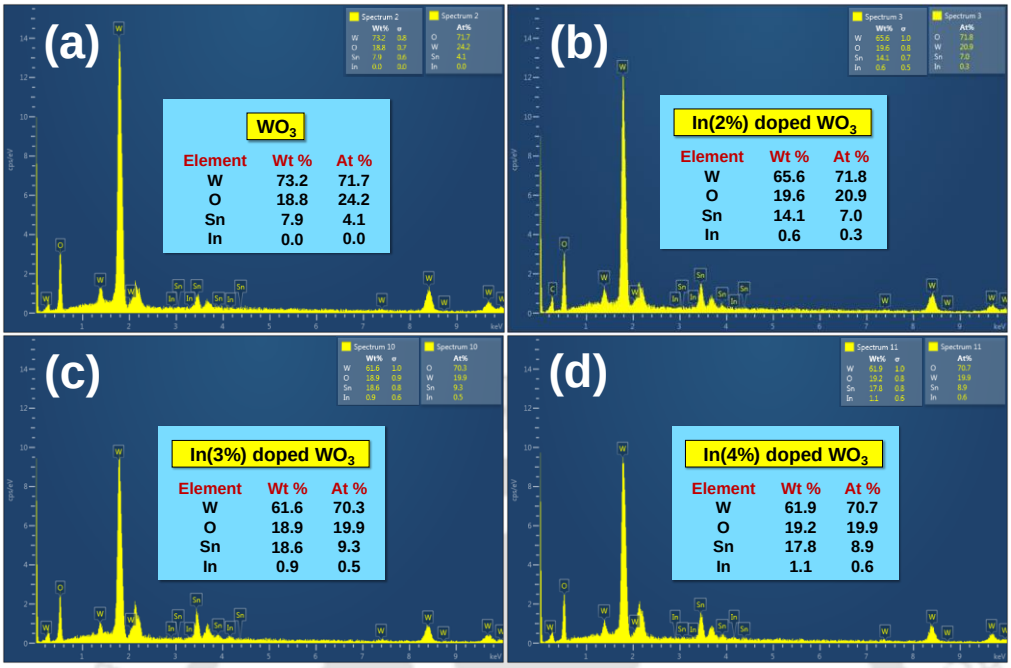

Figure 3.3.4 EDX analysis data of bare and modified In-doped WO_3 photoanodes.

Figure 3.3.5(a) is the FETEM image of monoclinic In-doped WO_3 photoanode material, which evidences the synthesis of nanoblock structures. **Figure 3.3.5(b)** shows the high-resolution transmission electron microscopy (HR-TEM) image and the inverse fast Fourier transform (IFFT) pattern of In-doped WO_3 composite. IFFT patterns indicate an average interplanar spacing of ~ 0.37 nm which is well agreeing to (200) crystal plane of monoclinic WO_3.[20] FETEM-EDX analysis was carried out to confirm the presence of individual elements (**figure 3.3.6 (i-iv)**), which are uniformly distributed, i.e., tungsten (red), oxygen (green) and indium (cyan).

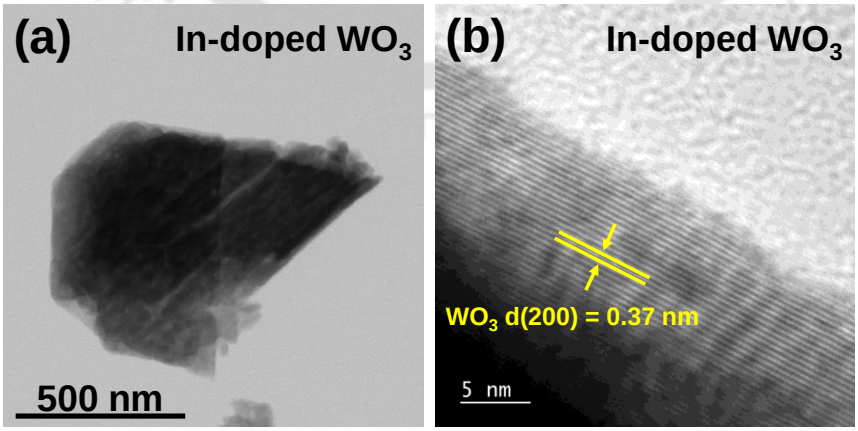

Figure 3.3.5 (a) FETEM (b) HR-TEM images of In-doped WO_3 photoanode.

Part of this chapter has been published in **Chem Asian J. 2020, 15, 3886**.

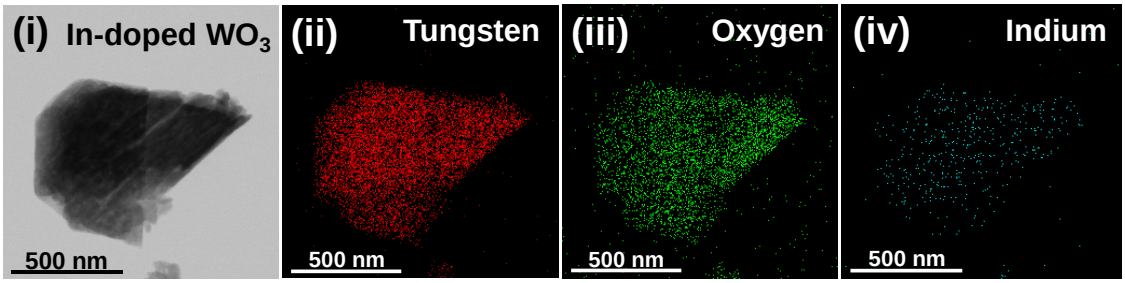

Figure 3.3.6 (i) STEM image and corresponding individual elemental mapping figures of In-doped WO_3 photoanode having (ii) tungsten, (iii) oxygen and (iv) indium.

3.3.4 X-ray photoelectron spectroscopy (XPS) analysis

In order to explain the electronic structure of both bare WO_3 and In-doped WO_3 photoanodes, XPS study was carried out, as shown in **figure 3.3.7**. **Figure 3.3.7(a)** is the survey spectra of pristine WO_3 and In-doped WO_3 thin films, which confirms the presence of elements such as tungsten and oxygen in both the photoanodes. All the characteristic peaks for undoped and doped WO_3 thin films are well-matched with the XPS spectra of W 4f, O 1s and In 3d in the reported literature.[21,22] **Figure 3.3.7(b)** indicates the O 1s peaks for bare WO_3 and In-doped WO_3 photoanodes. The asymmetric O 1s peaks for both photoanodes were fitted with two different peaks, i.e., lattice oxygen peak and surface oxygen vacancy peak. The lattice oxygen peak for WO_3 photoanode was observed to be at ~ 530.55 eV binding energy, which was shifted to lower binding energy ~ 530.50 eV with In-doping. Amount of surface oxygen vacancies for modified photoanodes were increased by approximately 7% compared to its bare counterpart. The increased oxygen vacancies can be attributed to the doping of In^{3+}, replacing W^{6+}, which induces non-stoichiometry into the compound, leading to oxygen vacancies. However, due to the minimal amount of Indium doping and the ionic radii match, no structural and chemical changes were observed. The W^{6+} $4f_{7/2}$ and W^{6+} $4f_{5/2}$ peaks for monoclinic WO_3 were observed to be at ~ 35.79 eV and ~ 37.92 eV (**figure 3.3.7(c)**). With In-doping, these two W $4f_{7/2}$ and W $4f_{5/2}$ peaks shifted towards the lower binding energies i.e., ~ 35.74 eV and ~ 37.87 eV, respectively. The characteristic peaks at ~ 444.27 eV and ~ 451.82 eV represents In^{3+} $3d_{5/2}$ and In^{3+} $3d_{3/2}$, respectively, which suggests the presence of In^{3+} ions in In-doped WO_3 photoanode (**figure 3.3.7(d)**). The ionic radius of In^{3+} (0.8 Å) is similar to that of the ionic radius of W^{6+} (0.74 Å), which illustrates that In^{3+} ions are partially occupying W^{6+} ions in modified In-doped WO_3 photoanode.

Part of this chapter has been published in **Chem Asian J. 2020, 15, 3886**.

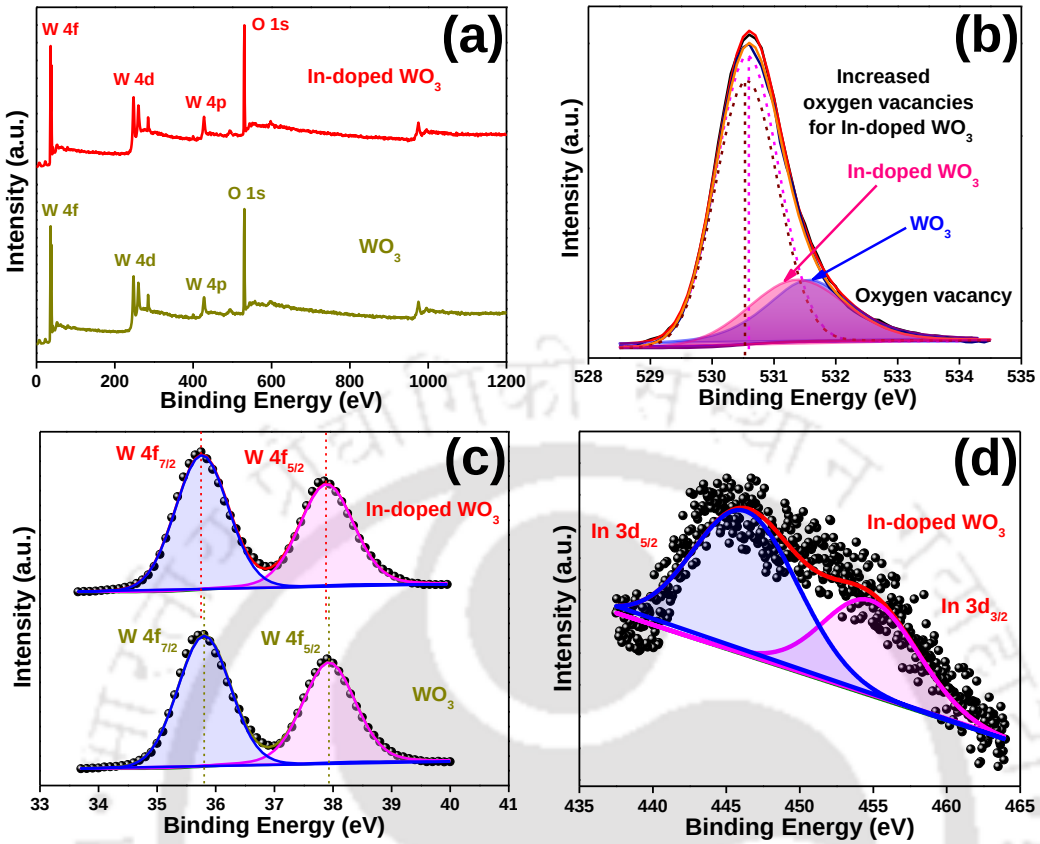

Figure 3.3.7 XPS spectra of both bare WO_3 and In-doped WO_3 photoanodes (a) Survey spectra (b) Oxygen 1s peaks fitted with lattice oxygen and surface oxygen vacancy peaks (c) W^{6+} $4f_{7/2}$ and W^{6+} $4f_{5/2}$ peaks of pristine WO_3 and In-doped WO_3 thin films (d) In^{3+} $3d_{5/2}$ and In^{3+} $3d_{3/2}$ peaks for In-doped WO_3 thin film.

3.3.5 Photoelectrochemical characterizations

PEC water oxidation activities of bare WO_3 and In-doped WO_3 photoanodes were carried out in 0.1M Na_2SO_4 neutral electrolyte under dark and light illumination to know the effect of In-doping on WO_3 photoanode (**figure 3.3.8**). **Figure 3.3.8(a)** represents the linear sweep voltammetry (LSV) curves of bare WO_3 and In-doped WO_3 photoanodes. The photocurrent density value of 0.71 mA/cm^2 at 1.23V vs. RHE was recorded for the bare monoclinic WO_3 photoanode. In order to optimize the In-doped WO_3 thin film, we have analyzed the doping concentration of indium from 2 wt% to 4 wt%, as shown in **figure 3.3.8(b)**. The current density values for 2 wt%, 3 wt% and 4 wt% In-doped WO_3 were recorded to be 1.43 mA/cm^2, 2.18 mA/cm^2 and 1.31 mA/cm^2 at 1.23V vs. RHE, respectively. Finally, the optimized In-doped WO_3 photoanode with 3 wt% indium doping provided the maximum current density value of 2.18 mA/cm^2 at 1.23V vs. RHE, which is approximately 3-fold higher than that of undoped monoclinic WO_3 photoanode.

Part of this chapter has been published in **Chem Asian J. 2020, 15, 3886**.

The overloaded In^{3+} concentration over the WO_3 surface i.e., (4 wt%) reduces the current density efficiency, which is ascribed to the possible photogenerated electron-hole recombination. The 3-fold enhancement in PEC water oxidation by indium doping is attributed to better charge separation and transfer due to reduced energy band gap. The chronoamperometric analysis was carried out to know the change in photocurrent response due to indium doping on the WO_3 photoanode (**figure 3.3.8(c)**). Current density (J) vs. time (t) curves were recorded under ON-OFF conditions by chopping the light at an interval of 20 seconds at the fixed biased potential of 1.23 V vs. RHE. Photo responses for both bare WO_3 and In-doped WO_3 are similar to the photocurrent densities of LSV curves.

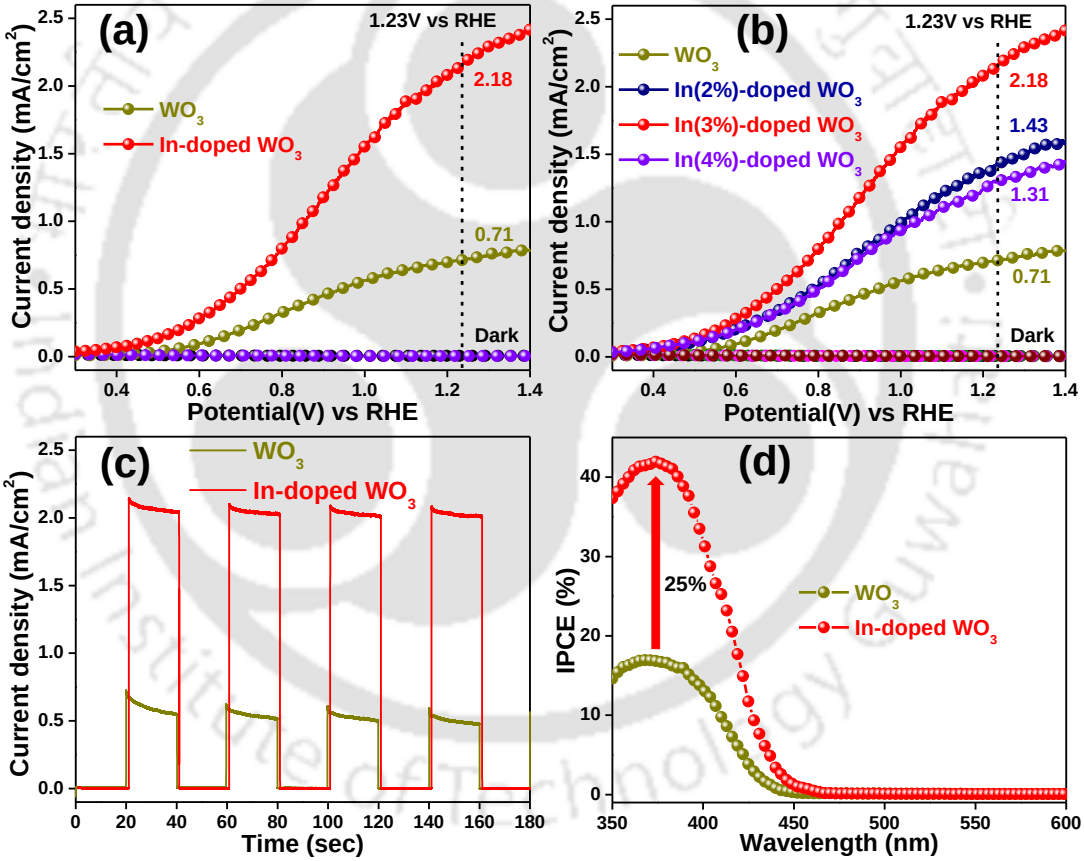

Figure 3.3.8 (a) LSV curves of bare WO_3 and optimized In-doped WO_3 photoanodes; (b) LSV curves of bare WO_3 and different concentrations of In-doped WO_3 photoanodes; and (c) chronoamperometric J–t curves of bare WO_3 and optimized In-doped WO_3 photoanodes. All the PEC water oxidation activities were carried in 0.1 M Na_2SO_4 neutral medium electrolyte out under 1 Sun illumination @ 10 mV/s scan rate at 1.23 V vs. RHE. (d) IPCE spectra of WO_3 and In-doped WO_3 photoanodes at 1.23V vs. RHE under monochromatic light of specific wavelength.

Part of this chapter has been published in **Chem Asian J. 2020, 15, 3886**.

IPCE spectra analysis was carried to study the effect of photoconversion efficiency for WO_3 photoanode by In-doping at 1.23V vs. RHE under monochromatic light of specific wavelength as shown in **figure 3.3.8(d)**. In the case of bare monoclinic WO_3 thin film, a strong photo-response was observed at 350-440 nm range, having a maximum 17% IPCE value at ~ 365.5 nm wavelength. The maximum IPCE value for optimized (3 wt%) In-doped WO_3 photoanode was reached up to 42% at ~ 373.7 nm wavelength with a broad light response region from 350 to 450 nm. The IPCE value for In-doped WO_3 photoanode was enhanced by ~ 25% as compared to pristine monoclinic WO_3 photoanode. The increased IPCE value indicates that the enlarged, visible light absorption by In-doped WO_3 gives more PEC activities at the UV region as compared to the bare one.

3.3.6 Electrochemical impedance spectroscopy (EIS) analysis

In order to inspect the effect of In-doping on the WO_3 photoanode, EIS measurements were analyzed under 1 Sun illumination at 1.23V vs. RHE, as shown in **figure 3.3.9**. **Figure 3.3.9(a)** indicates the Nyquist plots of bare monoclinic WO_3 and In-doped WO_3 photoanodes in addition to their fitted curves. For clarification, we have proposed an equivalent circuit model for fitting the impedance measurement data, as shown in **figure 3.3.9(a)**. The recorded R_{ct} values for WO_3 and In-doped WO_3 are 937.4 Ω and 546.8 Ω, respectively, which confirms the increment in electrical conductivity and interfacial charge transfer between semiconductor and electrolyte due to In-doping on WO_3 photoanode. The recorded R_{trap} values for WO_3 and In-doped WO_3 photoanodes are 280 Ω and 49.95 Ω, respectively, which reveals the depletion of trap sites on WO_3 photoanode with boosted hole transfer property due to In-doping. The above resistance parameters illustrate that the reduced charge transfer resistance at the semiconductor-electrolyte interface for modified In-doped WO_3 thin film could be the reason behind enhanced PEC water oxidation kinetics. All the recorded Nyquist plot parameters in addition to the charge carrier densities of bare WO_3 and In-doped WO_3 photoanodes, are listed below in **table 3.3.2**.

Figure 3.3.9(b) shows the Mott−Schottky (MS) plots for WO_3 and In-doped WO_3 photoanodes. MS plots gave the carrier density values for both WO_3 and In-doped WO_3 thin films to identify the effect of charge carrier property due to In-doping on monoclinic WO_3 photoanode. The positive slopes for both undoped and doped photoanodes confirm the nature of n-type semi-conductivities, but the positive slope of undoped WO_3 is higher than that of doped WO_3. The

Part of this chapter has been published in **Chem Asian J. 2020, 15, 3886**.

calculated charge carrier density values for both WO_3 and In-doped WO_3 photoanodes were found to be 1.34×10^{21} cm^{-3} and 3.86×10^{21} cm^{-3}, respectively. The effect of In-doping on WO_3 photoanode is significant and the charge carrier density for In-doped WO_3 was enhanced by 3 times compared to the bare WO_3 photoanode. According to reported literature, the enhanced charge density is the reason behind improved electrical conductivity and higher PEC efficacy.[2] In the case of In-doped WO_3 thin film, In^{3+} ions act as the donor dopants, which help in improving charge carrier density by providing additional charge carriers. The recorded E_{FB} value for In-doped WO_3 photoanode is 0.5 eV, which was shifted by ~ 0.03 eV from the E_{FB} value of bare WO_3, i.e., 0.47 eV. After modification with In^{3+} doping, the small positive shifting in E_{FB} value is because of the enhanced charge carrier density, reduced bandgap and shifted energy band positions.

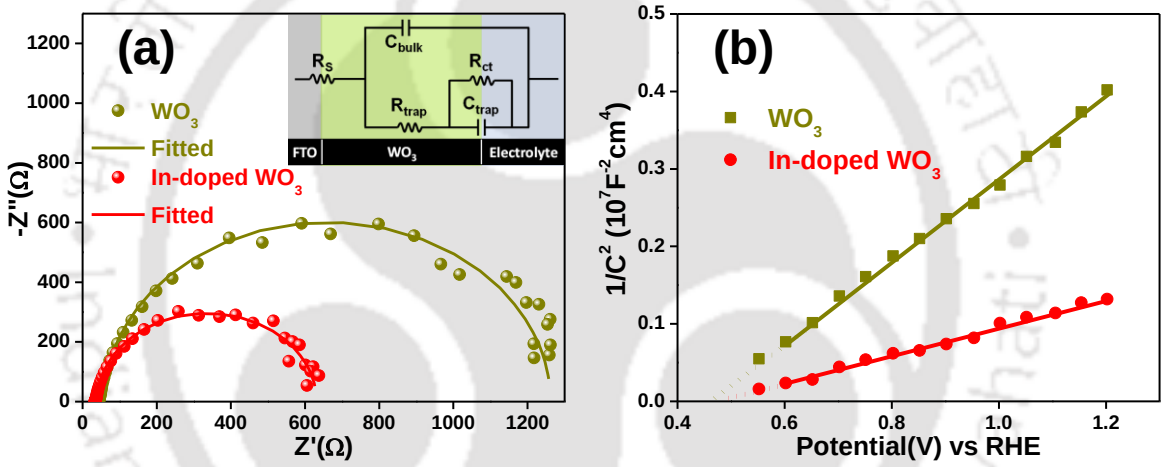

Figure 3.3.9 (a) Nyquist plots of bare WO_3 and modified In-doped WO_3 photoanodes in addition to their fitted curves under 1 Sun illumination and (b) Mott–Schottky plots for WO_3 and In-doped WO_3 photoanodes.

Table 3.3.2 Fitting parameters of Nyquist plots for bare WO_3 and In-doped WO_3 photoanodes in addition to their charge carrier densities.

Photoanode	$R_s(\Omega)$	$R_{trap}(\Omega)$	$R_{ct}(\Omega)$	$N_D(cm^{-3})$
WO_3	44.26	280	937.4	1.34×10^{21}
In doped WO_3	34.14	49.95	546.8	3.86×10^{21}

3.3.7 Charge separation and charge injection efficiencies

Hole-scavenger test for bare WO_3 and In-doped WO_3 semiconductors was carried out to get the effect of In-doping on charge separation efficiency and charge injection efficiency for bare WO_3 (**figure 3.3.10(a)**). The hole scavenger test was analyzed by the addition of 0.03 M Na_2SO_3

Part of this chapter has been published in **Chem Asian J. 2020, 15, 3886**.

with 0.1 M Na_2SO_4 electrolyte.[8] The recorded current density values for undoped and In-doped WO_3 photoanodes were 1.64 mA/cm^2 and 2.65 mA/cm^{2,} respectively. The current densities were enhanced by 2.3 fold and 1.2 fold with hole scavenger for bare WO_3 and In-doped WO_3 photoanodes, respectively. In addition to those current densities, the onset potentials were also shifted by ~ 0.4 eV towards lower potentials in both cases i.e., from 0.5 eV to 0.1 eV. The huge shifting of onset potentials is attributed to enhancement in catalytic activities i.e., overpotential reduction which indicates that the photogenerated holes were facilitated significantly from our photoanodes towards electrolyte solution at a lower bias. In-doped WO_3 photoanode gave 2.18 mA/cm^2 current density without any hole scavenger, which is 1.34 times higher than that of bare WO_3 with hole scavenger. From this experiment, it was clear that more number of holes are available for hole scavenging in normal Na_2SO_4 electrolyte by In-doping on monoclinic WO_3 nanoblocks in comparison to undoped WO_3 in Na_2SO_4 and Na_2SO_3 electrolyte. The charge separation efficiency was found to be 66% by In-doping on WO_3 photoanode, which is ~ 25% higher than that of bare WO_3 (**figure 3.3.10(b)**). This result illustrates the better and faster charge separation capability of modified WO_3 photoanode by doping with indium as compared to that of bare WO_3 photoanode. Similarly, the charge injection efficiency of ~ 82% for modified In-doped WO_3, was found to be ~ 38% higher than that of undoped WO_3 (**figure 3.3.10(c)**). In^{3+} ions play a vital role in the improvement of charge carrier densities and higher carrier mobility. Because of these factors, charge injection and charge separation efficiency were improved.

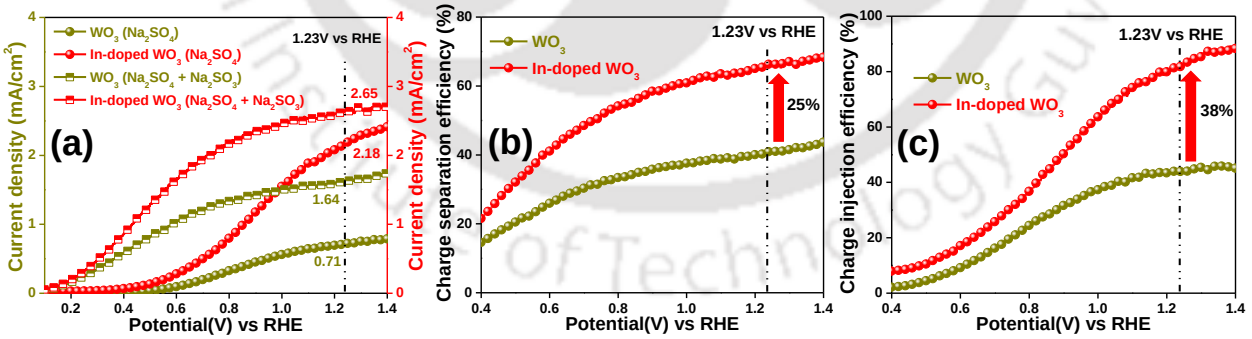

Figure 3.3.10 (a) LSV curves in the presence of neutral medium Na_2SO_3 hole scavenger electrolyte, (b) charge separation efficiencies, (c) charge injection efficiencies of WO_3 and In-doped WO_3 photoanodes at 1.23V vs. RHE under 1 Sun illumination.

Part of this chapter has been published in **Chem Asian J. 2020, 15, 3886**.

3.3.8 Faradaic yield and stability of the photoanode

Figure 3.3.11(a) illustrates the Faradaic yield measurements of In-doped WO_3 photoanode for hydrogen and oxygen evolutions. In-doped WO_3 photoanode gave ~ 90% and ~ 94% of Faradaic efficiencies for PEC water oxidation and reduction, respectively, after 1 h of experiment. **figure 3.3.11(b)** indicates the operational stability effect of In-doping on WO_3 thin film. The experiment was carried out for both undoped and doped thin WO_3 films in 1M Na_2SO_4 electrolyte at 1.23V vs. RHE under 1 Sun illumination. From 1 hour of experiment, it was clear that both photoanodes have almost similar stabilities.

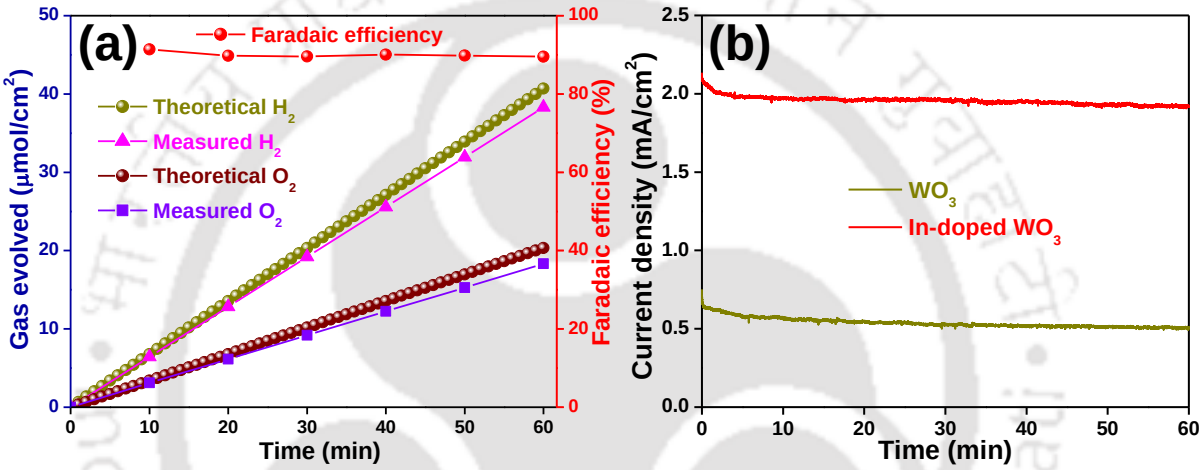

Figure 3.3.11 (a) Faradaic efficiency plot of modified In-doped WO_3 photoanode for PEC water oxidation in addition to the evolution of both hydrogen and oxygen gas; (b) stability taste for both undoped and doped WO_3 thin film. Both (a) and (b) analysis were carried out at a fixed potential of 1.23V vs. RHE under 1 Sun illumination.

3.3.9 Probable mechanism

Valence band-XPS spectra of bare WO_3 and optimized In-doped (3 wt%) WO_3 photoanodes are shown in **figure 3.3.12(a)**. VB position for optimized In-doped WO_3 photoanode was found to be 2.9 eV, which was shifted by ~ 0.1 eV downward from the VB position of bare WO_3 photoanode, i.e., 2.8 eV. However, the reduction in bandgap energy and the downward shifting of the Fermi energy level of WO_3 photoanode due to In-doping were already confirmed from optical absorption spectra and MS plot analysis data. By analyzing the above results, it was found that the conduction band (CB) position for the modified photoanode was shifted by 0.12 eV downward due to In-doping. Both VB and CB positions of WO_3 photoanode were altered to higher values by the addition of In-dopant, which is attributed to enhanced PEC water oxidation efficacy. The probable schematic band position analysis of bare WO_3 and optimized In-doped (3 wt%) WO_3

Part of this chapter has been published in **Chem Asian J. 2020, 15, 3886**.

photoanodes based on their optical absorption, Mott−Schottky and VB-XPS spectra analysis data, is provided below in **figure 3.3.12(b)**.

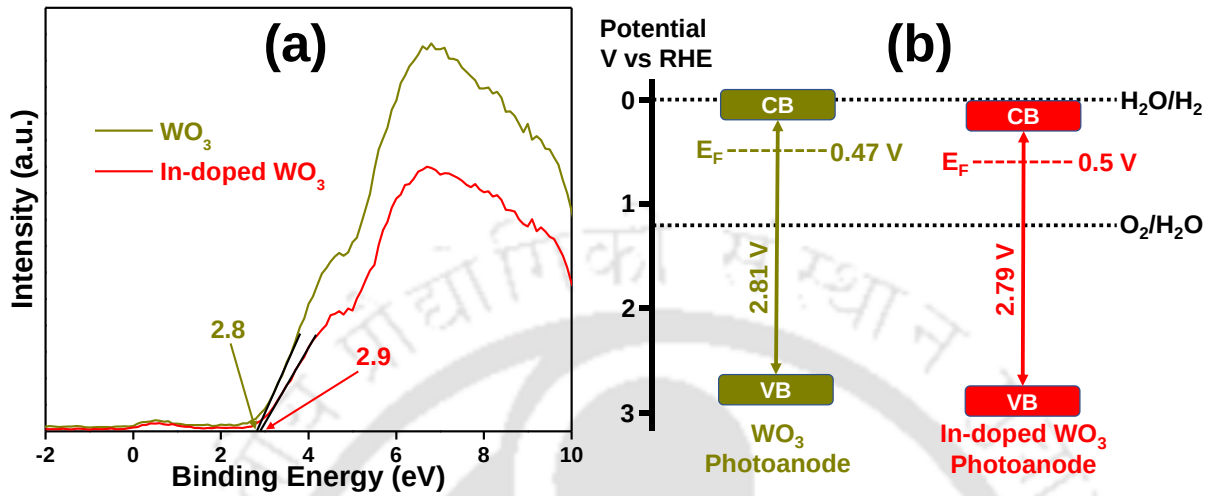

Figure 3.3.12 (a) Valence band-XPS spectra (b) Schematic band position analysis of bare WO_3 and optimized In-doped (3 wt%) WO_3 photoanodes.

3.4 CONCLUSIONS

In conclusion, we have examined the effect of In^{3+} dopant on monoclinic WO_3 nanoblocks, growing vertically over FTO without seed layer deposition. After modification with In^{3+} dopant, it was found that W^{6+} ions are being occupied partially by In^{3+} ions in the modified In-doped WO_3 photoanode. These In^{3+} ions are providing additional carriers for amplifying the number of carrier densities. An impressive current density value of 2.18 mA/cm^2 has been achieved by the optimized In-doped WO_3 photoanode at 1.23V vs. RHE, which is ~ 3 times higher than the undoped monoclinic WO_3 photoanode. The charge carrier density was enhanced by ~ 3 times for In-doped WO_3 thin film in comparison to bare WO_3. The modified photoanode with In-doping provided ~ 90% of Faradaic efficiency for PEC water oxidation. Higher charge carrier density amplified by In^{3+} dopants on WO_3 nanoblocks helps in boosting photogenerated charge separation and suppressing charge recombination. This work leads to better efficiency with an inexpensive eco-friendly strategy for WO_3 based PEC water oxidation process.

Part of this chapter has been published in **Chem Asian J. 2020, 15, 3886**.

3.5 REFERENCES

1. S. S. K. Ma, K. Maeda, R. Abe and K. Domen, *Energy Environ. Sci.*, 2012, **5**, 8390-8397.
2. T. Zhang, Z. L. Zhu, H. N. Chen, Y. Bai, S. Xiao, X. L. Zheng, Q. Z. Xue and S. H. Yang, *Nanoscale*, 2015, **7**, 2933.
3. W. Wei, S. Shaw, K. Lee and P. Schmuki, *Chem.–Eur. J.*, 2012, **18**, 14622.
4. G. Zheng, J. Wang, H. Liu, V. Murugadoss, G. Zu, H. Che, C. Lai, H. Li, T. Ding, Q. Gao and Z. Guo, . *Nanoscale*, 2019, **11**, 18968−18994.
5. H. Zhang, W. Tian, Y. Li, H. Sun, M. O. Tade and S. Wang, *J. Mater. Chem. A*, 2018, **6**, 6265–6272.
6. F. Ronconi, Z. Syrgiannis, A. Bonasera, M. Prato, R. Argazzi, S. Caramori, V. Cristino and C. A. Bignozzi, *J. Am. Chem. Soc.*, 2015, **137**, 4630–4633.
7. Y. Li, L. Zhang, R. Liu, Z. Cao, X. Sun, X. Liu and J. Luo, *ChemCatChem*, 2016, **8**, 2765–2770.
8. B. Jin, E. Jung, M. Ma, S. Kim, K. Zhang, J. I. Kim, Y. Son and J. H. Park, *J. Mater. Chem. A*, 2018, **6**, 2585-2592.
9. L. Li, J. Li, J. Bai, Q. Zeng, L. Xia, Y. Zhang, S. Chen, Q. Xu and B. Zhou, *Nanoscale*, 2018, **10**, 18378−18386.
10. B. Cole, B. Marsen, E. Miller, Y. Yan, B. To, K. Jones and M. Al- Jassim, *J. Phys. Chem. C*, 2008, **112**, 5213−5220.
11. A. J. E. Rettie, K. C. Klavetter, J. –F. Lin, A. Dolocan, H. Celio, A. Ishiekwene, H. L. Bolton, K. N. Pearson, N. T. Hahn, and C. B. Mullins, *Chem. Mater.*, 2014, **26**, 1670–1677.
12. B. Yang and V. Luca, *Chem. Commun*., 2008, **37**, 4454–4456.
13. W. Erbs, J. Desilvestro, E. Borgarello, and M. Grätzel, *J. Phys. Chem.*, 1984, **88**, 4001-4006.
14. Y. Liu, J. Li, W. Li, Y. Yang, Y. Li and Q. Chen, *The Journal of Physical Chemistry C*, 2015, **119**, 14834-14842.
15. S. S. Kalanur and H. Seo, *J. Colloid Interface Sci.*, 2018, **509**, 440–447.
16. S. S. Kalanur, I.-H. Yoo, K. Eom and H. Seo, *J. Catal.*, 2018, **357**, 127– 137.
17. X. Zhong, H. He, M. Yang, G. Ke, Z. Zhao, F. Dong, B. Wang, Y. Chen, X. Shi and Y. Zhou, *J. Mater. Chem. A*, 2018, **6**, 10456– 10465.

Part of this chapter has been published in **Chem Asian J. 2020, 15, 3886**.

18. J. Yang, W. Li, J. Li, D. Sun and Q. Chen, *J. Mater. Chem.*, 2012, **22**, 17744−17752.
19. Y. Li, Z. Liu, Z. Guo, M. Ruan, X. Li and Y. Liu, *ACS Sustainable Chem. Eng.*, 2019, **7** (14), 12582–12590.
20. N. Zhang, C. Chen, Z. Mei, X. Liu, X. Qu, Y. Li, S. Li, W. Qi, Y. Zhang, J. Ye, V. A. R. Roy and R. Ma, *ACS Appl. Mater. Interfaces*, 2016, **8**, 10367–10374.
21. L. Wang, C. S. Tsang, W. Liu, X. Zhang, K. Zhang, E. Ha, W. M. Kwok, J. H. Park, L. Y. Suk Lee and K. Y. Wong, *J. Mater. Chem. A*, 2019, **7**, 221– 227.
22. B. Pujilaksono, U. Klement, L. Nyborg, U. Jelvestam, S. Hill and D. Burgard, *Mater. Charact.*, 2005, **54**, 1–7.

Part of this chapter has been published in **Chem Asian J. 2020, 15, 3886**.

CHAPTER 4

Hexagonal boron nitride as a superior hole extractor for efficient charge separation in WO_3-based photoelectrochemical water oxidation

This chapter demonstrates the modification of stable monoclinic WO_3 nanoblocks with hexagonal boron nitride quantum dots (h-BNQDs) incorporation to improve the photogenerated electron−hole separation and additionally to hinder the charge recombination process. A comprehensive morphological, optical and photoelectrochemical properties of the BNQDs modified WO_3 photoanode are presented to understand the hole extraction mechanism by BNQDs for efficient PEC water oxidation performance.

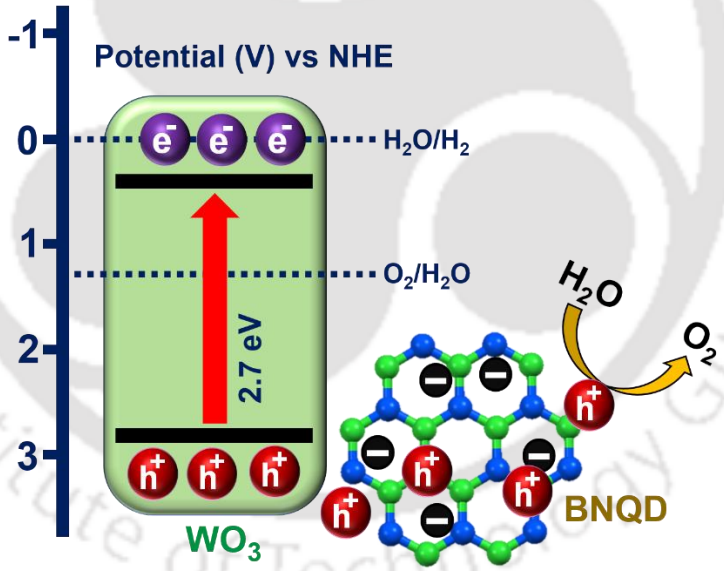

ACS APPLIED ENERGY MATERIALS

M. K. Mohanta *et al.*, 2019, **2**, 7457

4.1 INTRODUCTION

As per discussion in the previous chapter, to improve the experimental efficiency of WO_3, various methods like heterojunction strategy for better charge separation, the addition of metal dopants to increase carrier density, the addition of electron charge collectors for better charge separation, deposition of overlayer for faster oxygen evolution reaction (OER) kinetics have been applied.[1-4] Photogenerated electron-hole pair separation is a key factor to enhance efficiency for PEC water oxidation. The incorporation of two-dimensional materials such as reduced graphene oxide (RGO) has been extensively utilized as a photogenerated charge carrier vehicle to facilitate the photogenerated electron-hole separation.[5] Graphene-like boron nitride (BN), also known as "white graphene" is a structural analogue of graphene having in-plane high thermal conductivity, chemical and thermal stability, and minimal toxicity.[6] Carbon and graphene quantum dots have been sensitized with photoanodes to enhance the PEC performance previously.[7] The h-BNQDs, synthesized from two-dimensional boron nitride nanosheets have been recently explored as hole-extracting agents in photocatalysis. From the literature, it is known that BNQDs are negatively charged species dominantly at the edge geometry.[8-10] By quenching the size of hexagonal BN to the quantum dot level, BNQDs show the edge effects and defect centers.[9] Thus, BNQDs is a suitable candidate to extract the photogenerated holes which can enhance the charge separation, thereby the water oxidation efficacy. In the present work, we have studied the effect of BNQDs incorporation on *in-situ* grown monoclinic WO_3 nanoblocks directly over Fluorine-doped tin oxide (FTO) surface without using any seed layer. The present method of design and fabrication of the photoanode materials are simple, effective and may have several applications with respect to other photoanode materials.

4.2 EXPERIMENTAL METHODS

4.2.1 *In-situ* growth of WO_3 nanoblocks

WO_3 nanoblocks were synthesized directly over the FTO by hydrothermal method.[11] In a typical synthesis, 0.250 g of sodium tungsten dihydrate ($Na_2WO_4 \cdot 2H_2O$) was dissolved in 30 mL of deionized water under constant stirring at room temperature. Then, 10 mL of 3 M HCl was added dropwise to get a white precipitated solution. At the same time, 0.235 g of ammonium oxalate monohydrate ($(NH_4)_2C_2O_4 \cdot H_2O$) was dissolved in 30ml of deionized water and stirred for 30 minutes at room temperature. The precursor solution of ammonium oxalate was added to white

Part of this chapter has been published in **ACS Appl. Energy Mater. 2019, 2, 7457.**

precipitated tungsten precursor solution with continuous stirring up to 1 hour to get a transparent colorless solution. The clear solution was then transferred to a 100 mL Teflon lined stainless steel autoclave. Four pieces of FTO glass substrates, which were ultrasonically cleaned with deionized water, acetone and isopropanol in sequence and finally dried and ozonized, were immersed and leaned against the wall of the Teflon-vessel with the conducting side facing down. Then, the autoclave was closed and put inside an oven for the hydrothermal reaction at 140 °C for 8 h. The Teflon vessel was allowed to cool down at room temperature, then *in-situ* growth of WO_3 thin films were properly washed with deionized water and dried in an oven at 70 °C for 15 minutes. After that, dried substrates were annealed at 500 °C for 1 h in a muffle furnace to form WO_3 thin films.

4.2.2 Synthesis of BNQDs

BNQDs were synthesized hydrothermally.[12] Firstly, 0.100 g of boric acid was dissolved in 10 mL of deionized water with continuous stirring for a few minutes at room temperature. After dissolving boric acid, 0.034 g of melamine was added to the same precursor solution under constant stirring for 30 minutes. Then, the solution mixture was transferred to a 25 mL Teflon autoclave and was placed in the oven for the hydrothermal reaction at 200 °C for 15 h. After completion of the reaction, the Teflon vessel was allowed to cool down to room temperature, and finally, the solution containing BNQDs was collected by filtering the reaction solution with a 0.22 µm syringe filter.

4.2.3 Synthesis of WO_3-BN Photoanode

WO_3-BN photoanodes were synthesized by the chemical bath deposition (CBD) technique. Briefly, as synthesized BNQDs stock solution was diluted to half, one-third and one-fourth by adding deionized water and marked as A, B and C, respectively. Then, previously synthesized WO_3 thin films were immersed in those diluted BNQDs solution of different concentrations and placed inside a vacuum oven under temperature 70 °C for 12 h. After completion of the CBD reaction, the films with the solution were allowed to cool at room temperature and then the films were rinsed properly with deionized water. The films were dried in the oven at temperature 70 °C for 1h and annealed by using a hot plate under different temperatures of 200 °C, 300 °C and 400 °C for 1 h. Different annealing temperatures i.e., 200 °C, 300 °C and 400 °C were marked as 200, 300 and 400, respectively. All the modified photoanodes were marked with respect to concentration

Part of this chapter has been published in **ACS Appl. Energy Mater. 2019, 2, 7457.**

and temperature such as WO_3-BN-X-Y, where X corresponds to concentration and Y corresponds to temperature. For a better understanding, a graphical representation of the complete synthesis procedure has been given below in **Scheme 4.2.1**.

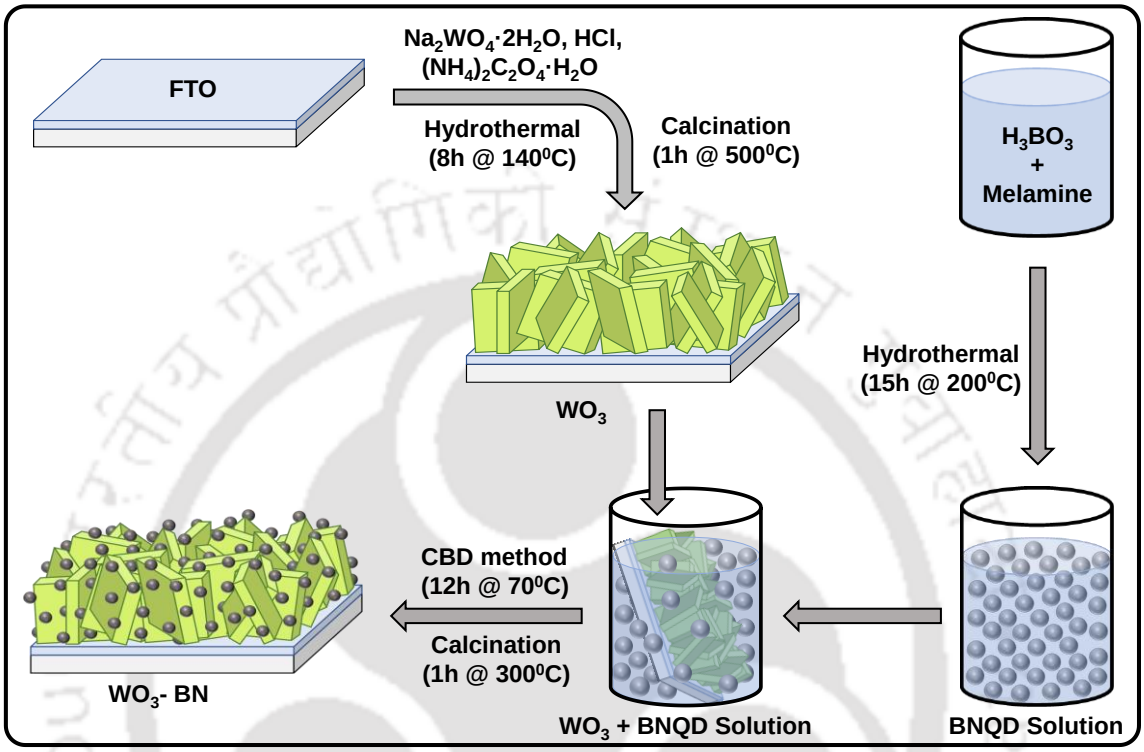

Scheme 4.2.1 The fabrication process of *in-situ* grown WO_3 photoanode directly over FTO and the modification of WO_3-BN photoanode with the incorporation of BNQDs by CBD method.

4.3 RESULTS AND DISCUSSION

4.3.1 Thin-film XRD and FT-IR analysis

The crystal structure and phase purity of as prepared photoanodic materials were characterized by thin film XRD measurements, as shown in **figure 4.3.1(a)**. The diffraction peaks of WO_3 thin film (after annealing) represent the monoclinic phase of WO_3 which corresponds to JCPDS number 01-072-0677. The leading diffraction peak (200) of WO_3 nanoblocks at $2\theta = 24.27^{\circ}$ confirms the pure monoclinic phase.[11] No change in peak positions and no extra peaks for BNQDs were found from the XRD pattern of WO_3-BN by comparing with the XRD pattern of WO_3. No peaks for BNQDs was found in the composite may be due to the very low concentration of BNQDs. In order to confirm the presence of BNQDs in WO_3-BN composite, the FT-IR spectra for as-synthesized WO_3 photoanode, BNQDs, and modified WO_3-BN photoanode were carried

Part of this chapter has been published in **ACS Appl. Energy Mater. 2019, 2, 7457.**

out (**figure 4.3.1(b)**). In case of WO_3 photoanode, significant peaks at 3432 cm^{-1}, 1632cm^{-1} and 821cm^{-1} indicate the presence of WO_3-H_2O interactions, W-OH interactions (bending vibrations) and W-O-W stretching vibrations, respectively.[13] For BNQDs, the significant peaks at 3208 cm^{-1}, 1413 cm^{-1}, 1181 $cm^{-1,}$ and 715 cm^{-1} indicate the presence of B-OH interactions, hexagonal B-N, BN-O bonding interactions, and B-N bonding interactions, respectively.[14] The FT-IR spectrum of the modified WO_3-BN photoanode indicates the presence of all the significant peaks of WO_3 as well as BNQDs, which illustrates the proper incorporation of BNQDs on the surface of WO_3 nanoblocks.

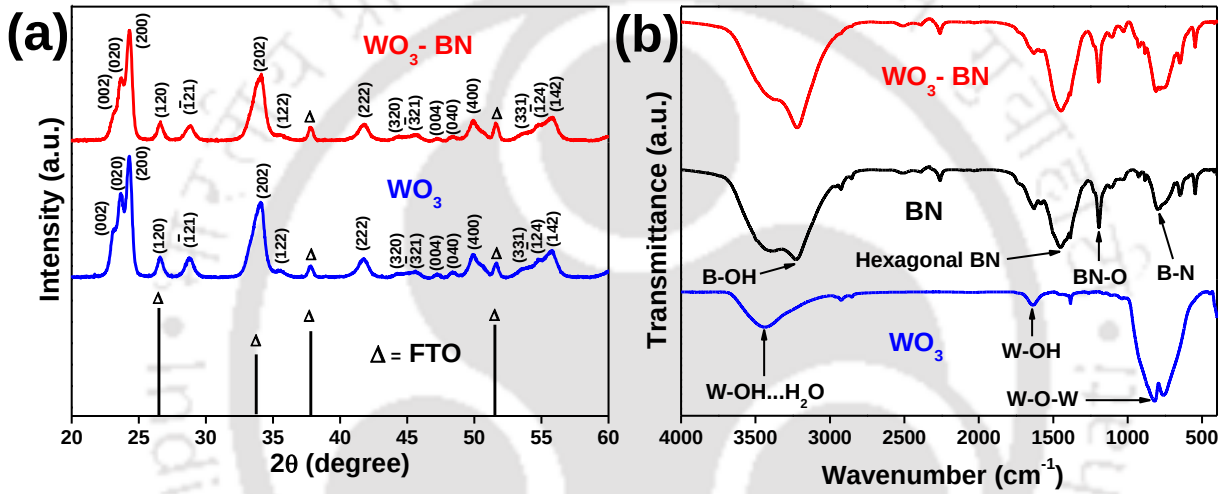

Figure 4.3.1 (a) Thin film XRD plots of FTO, bare WO_3 and WO_3-BN composite; (b) FT-IR Spectra of as-synthesized WO_3 photoanode, BNQDs, and modified WO_3-BN photoanode.

4.3.2 UV-visible absorption spectra, Tauc plot and PL spectra analysis

Figure 4.3.2(a) shows the Tauc plot extrapolated from absorption spectra for both bare and modified photoanodes for bandgap energy calculations. The absorption bands for both photoanodes are similar at 2.86 eV, and the region was found to be 400-500 nm for both cases, whereas the absorption band of BNQD was found at a lower wavelength, i.e., at 200-300 nm region. The UV-visible spectra and PL spectra of BNQDs (**figure 4.3.2(b)**) are inconsistent with the reported results.[6] Tauc plots illustrate that there was no significant change in band gap energy value by modification of WO_3 photoanode. In overall, the optical response for WO_3 photoanode was not significantly influenced after the BN modification.

Part of this chapter has been published in **ACS Appl. Energy Mater. 2019, 2, 7457.**

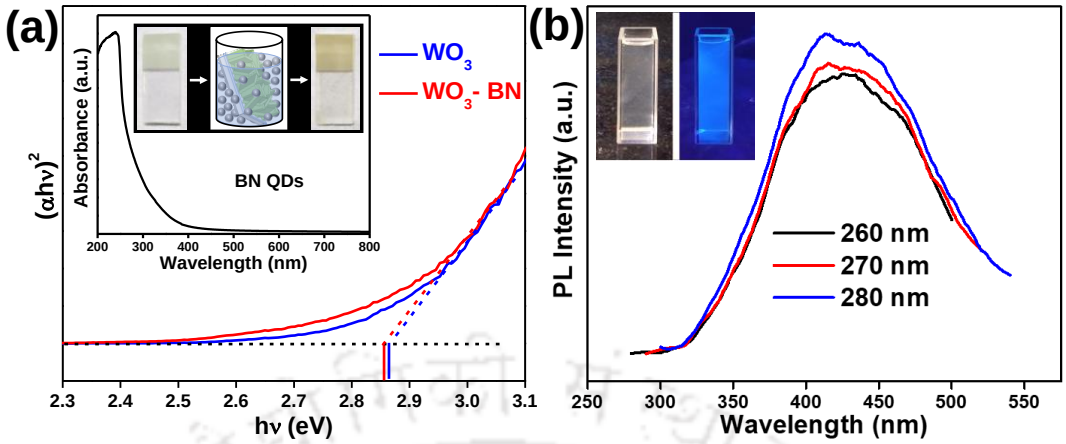

Figure 4.3.2 (a) Tauc plots for energy band gap determination of pristine WO_3 and modified WO_3-BN photoanodes along with UV-Visible absorption spectrum of BNQDs; (b) PL spectra of BNQDs at different excitation wavelengths from 260 to 280 nm.

4.3.3 Materials morphology

In order to know the morphology of monoclinic WO_3 thin film directly grown over FTO without any seed layer deposition, the FESEM analysis was carried out (**figure 4.3.3**). The top view of WO_3 thin film shown in **figure 4.3.3(a, b)** indicates the uniform distribution of WO_3 nanoblock structures. Incorporation of BNQDs over WO_3 photoanode does not change the

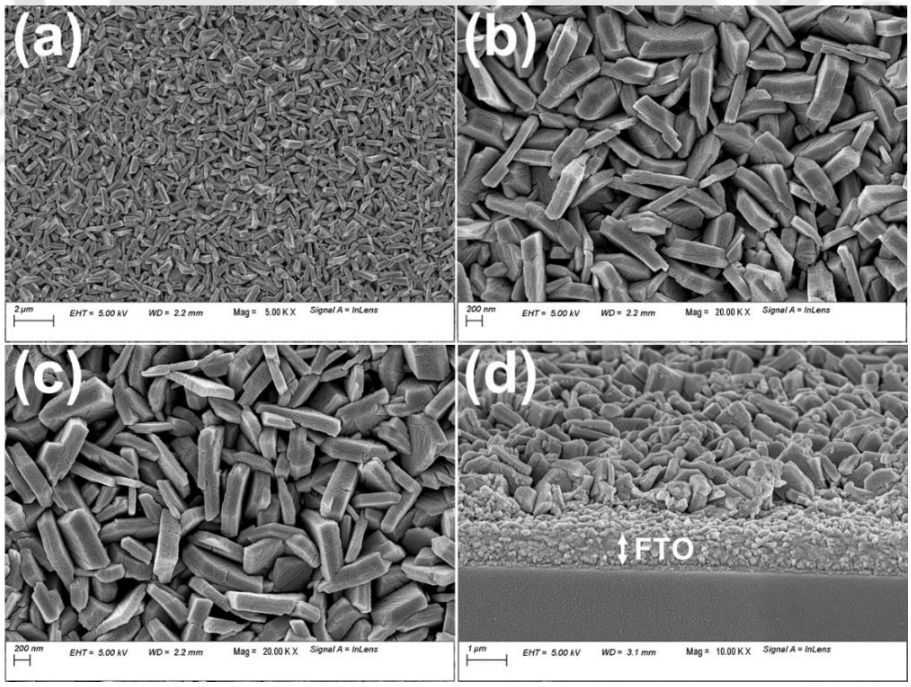

Figure 4.3.3 (a and b) FESEM images of WO_3 thin film directly grown over FTO by *in-situ* method, (c) FESEM image of WO_3-BN and (d) cross-sectional view of WO_3-BN thin film.

Part of this chapter has been published in **ACS Appl. Energy Mater. 2019, 2, 7457.**

morphology of WO_3, as seen from **figure 4.3.3(c)**. The cross-sectional view of the modified WO_3-BN composite shown in **figure 4.3.3(d)** confirms the vertical growth of WO_3 photoanode over FTO substrate with an average edge length of ~ 800 nm to 1μm.

FETEM analysis was carried out to further probe the crystal structures and features of the *in-situ* grown WO_3 nanoblocks with larger magnification. **Figure 4.3.4(a)** represents the FETEM image of monoclinic WO_3 photoanode, which confirms the formation nanoblock structure. **Figure 4.3.4(b)** shows the FETEM of WO_3-BN composite where BNQDs are distributed over the surface of WO_3. The size of the BNQDs are found to be of around 5 nm. The enlarged image shown in **figure 4.3.4(c)** further confirms the incorporation of BNQDs over the surface of WO_3 nanoblocks. **Figure 4.3.4(d)** represents the HRTEM image of WO_3-BN composite and the inverse fast Fourier transform (IFFT), where an average interplanar distance of about 0.37 nm corresponds to the (200) crystal plane of monoclinic WO_3 and interplanar distance of around 0.21 nm corresponds to the (100) crystal plane of BNQD.[15,16,12] According to the reported literatures, UV absorption spectrum, PL spectra and FETEM analysis confirms the QDs characteristics of our as-synthesized BNQDs.[6,35]

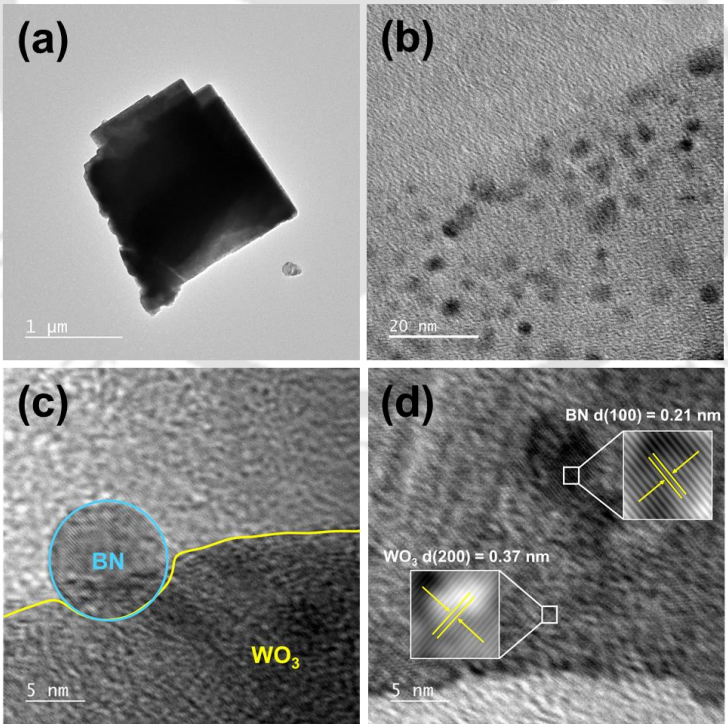

Figure 4.3.4 FETEM images of monoclinic (a) WO_3 nanoblock, (b) WO_3-BN composite showing the presence of BNQDs over the surface of WO_3 nanoblock, (c) incorporated BNQDs over the surface WO_3 nanoblock and (d) HRTEM image of WO_3-BN composite. The inset of (d) shows the IFFT pattern of both WO_3 nanoblock and BNQD.

Part of this chapter has been published in **ACS Appl. Energy Mater. 2019, 2, 7457.**

Figure 4.3.5 represents the scanning transmission electron microscopy (STEM) images of *in-situ* grown WO_3-BN composite to illustrate the distribution of elements and individual elemental uniformity in the composite material. **Figure 4.3.5(a)** signifies the high-angle annular dark-field STEM (HAADF-STEM) image of WO_3-BN, whereas **figure 4.3.5(b)** denotes the complete elemental mapping of tungsten, oxygen, boron, and nitrogen. **Figure 4.3.5(i)-(iv)** represents the individual mappings of tungsten (red), oxygen (green), boron (cyan), and nitrogen (yellow), respectively, which confirms the presence and uniform distribution of all the elements.

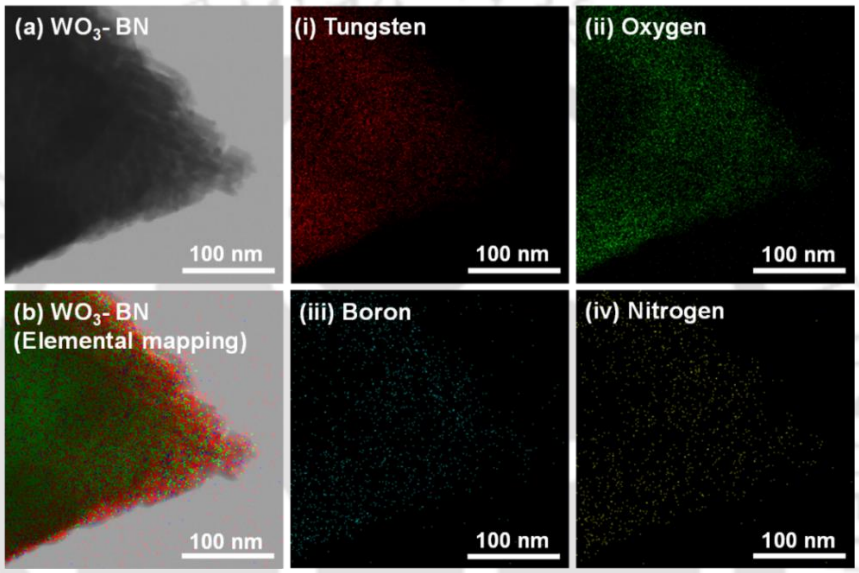

Figure 4.3.5 (a) STEM image of WO_3-BN, (b) complete elemental mapping of WO_3-BN and individual elemental mapping showing (i) W, (ii) O, (iii) B and (iv) N.

4.3.4 Photoelectrochemical characterizations

In order to know the influence of BNQDs on WO_3 photoanode, the photocurrent density of all the photoanodes were measured under dark and light illumination condition with Na_2SO_4 electrolyte solution. The photocurrent density of bare WO_3 was found to be 0.69 mA/cm^2 at potential 1.23V vs. RHE as shown in **Figure 4.3.6(a)**. Further, the WO_3 photoanode was modified with different concentrations of BNQDs solution and treated at different temperatures. From **figure 4.3.6(b)**, the current density values for WO_3-BN-A-200, WO_3-BN-A-300 and WO_3-BN-A-400 photoanodes were found to be 0.93 mA/cm^2, 1.15 mA/cm^2 and 0.74 mA/cm^2 respectively. Similarly from **figure 4.3.6(c)** and **4.3.6(d)**, the current densities for WO_3-BN-B-200, WO_3-BN-B-300, WO_3-BN-B-400, WO_3-BN-C-200, WO_3-BN-C-300 and WO_3-BN-C-400 were found to be 1.20 mA/cm^2, 1.24 mA/cm^2, 0.99 mA/cm^2, 1.39 mA/cm^2, 1.63 mA/cm^2 and 1.11 mA/cm^2,

Part of this chapter has been published in **ACS Appl. Energy Mater. 2019, 2, 7457.**

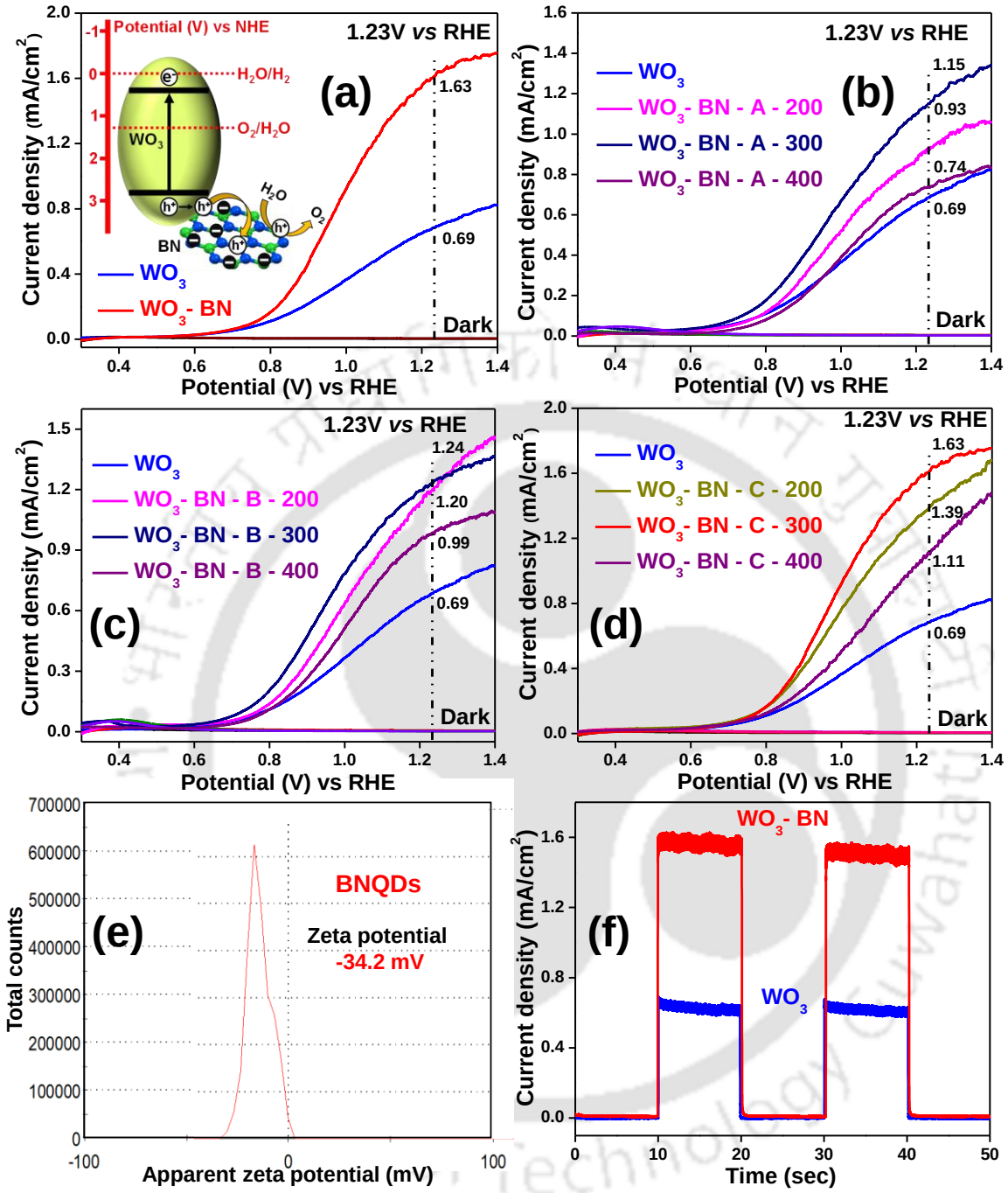

Figure 4.3.6 J-V curves of (a) WO_3 and optimized WO_3-BN photoanodes, (b) WO_3 along with WO_3-BN-A-200, WO_3-BN-A-300 and WO_3-BN-A-400 photoanodes, (c) WO_3, WO_3-BN-B-200, WO_3-BN-B-300 and WO_3-BN-B-400 photoanodes, (d) WO_3, WO_3-BN-C-200, WO_3-BN-C-300 and WO_3-BN-C-400 photoanodes under 1 Sun illumination at a scan rate of 10 mV/s in 0.1 M Na_2SO_4 electrolyte at 1.23V vs. RHE; (e) zeta potential (ς) plot for BNQDs at room temperature; (f) J-t curves of bare WO_3 and optimized WO_3-BN photoanodes under 1 Sun illumination at a scan rate of 10 mV/s in 0.1 M Na_2SO_4 electrolyte at 1.23V vs. RHE.

Part of this chapter has been published in **ACS Appl. Energy Mater. 2019, 2, 7457.**

respectively. With optimized concentration and temperature, the photocurrent density of WO_3-BN composite (i.e. WO_3-BN-C-300) was found to be 1.63 mA/cm^{2,} which is 2.4 times higher than bare WO_3. As per earlier reports, the hole extraction capability of negatively surface charged h-BN could be responsible for the photogenerated electron-hole separation.[8] In order to confirm the hole-extracting ability of BNQDs, zeta potential measurement was carried out (**figure 4.3.6(e)**). Zeta potential (ς) for BNQDs solution was found to be highly negative -34.2 mV, which attributes the ability of BNQDs to extract positive ions (holes). The increment in photocurrent density for modified photoanodes could be attributed to the exceptional hole extraction property of BNQDs, which results in efficient charge separation. The probable hole extraction mechanism is represented in the inset of **figure 4.3.6(a)**. **Figure 4.3.6(f)** explains the chronoamperometric analysis, i.e., current density (J) vs. time (t) curves of bare WO_3 along with the modified WO_3-BN photoanodes under light ON-OFF condition. These chronoamperometric measurements were taken by chopping the light at a regular interval of 10 seconds at a fixed biased potential of 1.23V vs. RHE. Photocurrent density values for both photoanodes are similar, which indicates the similar stabilities for both bare and modified photoanodes. By comparing chronoamperometric measurements with J-V curves, similar photocurrent responses for WO_3 and WO_3-BN photoanodes were found.

4.3.5 Electrochemical impedance spectroscopy (EIS) analysis

EIS measurements were carried out to explore the effect of incorporation of BNQDs on the surface of the *in-situ* grown WO_3 nanonblocks under 1 Sun illumination at 1.23V vs. RHE. **Figure 4.3.7(a)** represents the Nyquist plots for WO_3 and WO_3-BN photoanodes along with their fitted curves. An equivalent circuit model was proposed to fit and explain all the impedance data (inside **figure 4.3.7(a)**). The R_{ct} values for pristine WO_3 photoanode and modified WO_3 (WO_3-BN) photoanode were found to be 2330 Ω and 1649 Ω, respectively. The improvement in electrical conductivity was confirmed by these R_{ct} values. These values also confirmed the interfacial charge transfer process, which was more favorable in case of modified WO_3 photoanode as compared to that pristine one. At the same time, the R_{trap} values for pristine WO_3 photoanode and WO_3-BN photoanode were found to be 486.2 Ω and 57.75 Ω, respectively which confirms the presence of lesser trap sites in case of WO_3-BN as compared to bare WO_3. All the fitting parameters of Nyquist plots along with the charge carrier densities for bare as well as modified WO_3 photoanodes have been mentioned in **table 4.3.1**.

Part of this chapter has been published in **ACS Appl. Energy Mater. 2019, 2, 7457.**

Figure 4.3.7(b) illustrates the Mott-Schottky (MS) plots for WO_3 as well as WO_3-BN along with their calculated N_D values which give the idea about enhanced charge carrier property by incorporation of BNQDs on the surface of WO_3 nanoblocks. The n-type semiconducting behavior of both WO_3 and WO_3-BN photoanodes was proved by the positive slopes of MS plots in both cases. The charge carrier density values for pristine WO_3 and modified WO_3-BN photoanodes were 1.3×10^{21} cm^{-3} and 3.2×10^{21} $cm^{-3,}$ respectively. The charge carrier density value of the modified WO_3-BN photoanode was improved significantly, i.e. approximately 2.44 times higher than that bare one, which illustrates the improvement in electrical conductivity. In the case of WO_3-BN photoanode, the BNQDs extract the holes from valence band position of WO_3, which is the main cause for the improvement in charge carrier density as well as the reduction in electron-hole recombination.

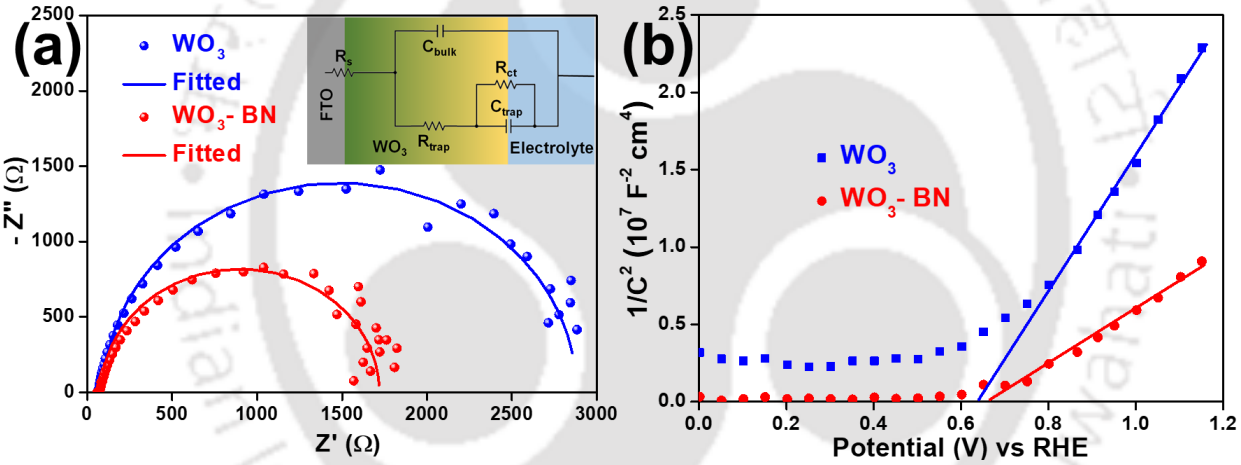

Figure 4.3.7 (a) The Nyquist plots of WO_3 and WO_3-BN photoanodes along with their fitted curves under light illumination and (b) the MS plots for WO_3 and WO_3-BN photoanodes.

Table 4.3.1 Fitting parameters of Nyquist plots for WO_3 and WO_3-BN photoanodes along with their charge carrier density values.

Photoanode	R_s (Ω)	R_{trap} (Ω)	10^{-6} C_{bulk} (F)	R_{ct} (Ω)	10^{-5} C_{trap} (F)	N_D (cm^{-3})
WO_3	63.57	486.2	39.46	2330	1.927	1.3×10^{21}
WO_3-BN	57.75	27.96	7.576	1649	2.443	3.2×10^{21}

Part of this chapter has been published in **ACS Appl. Energy Mater. 2019, 2, 7457.**

4.3.6 Charge separation and injection efficiencies along with operational stability

In order to calculate the charge separation efficiencies along with charge injection efficiencies due to the incorporation of BNQDs, photocurrent densities for both bare and modified WO_3 photoanodes were measured by the addition of a neutral medium hole-scavenger in the electrolyte as shown in **figure 4.3.8(a)**. As a neutral medium hole-scavenger electrolyte, 0.03 M Na_2SO_3 was added with 0.1M Na_2SO_4 electrolyte to overcome the interfacial hole transfer barrier for water oxidation.[3] By comparing photocurrent densities for pristine and modified WO_3 photoanodes with and without hole scavenger, it was found that both photocurrent densities and onset potentials were increased. The Na_2SO_3 helps in scavenging the photogenerated holes and transports to the surface of WO_3 nanoblocks.[17] Current density value for bare WO_3 photoanode was found to be 1.55 mA/cm^2 with hole scavenger which is 2.25 times higher than that of bare WO_3 without hole scavenger. At the same time, current density of modified WO_3-BN photoanode without hole scavenger was 1.63 mA/cm^2, which is still higher than that of bare WO_3 photoanode

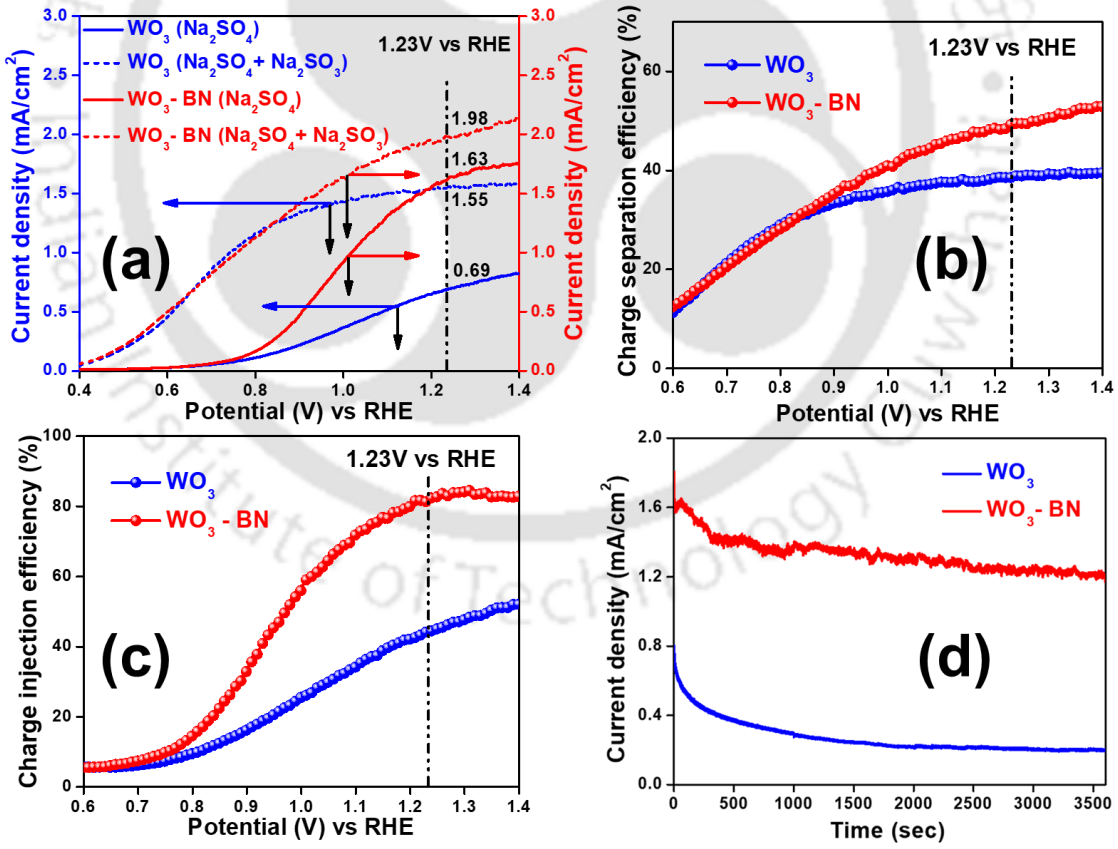

Figure 4.3.8 (a) J-V curves in the presence of hole-scavenger Na_2SO_3, (b) Charge separation efficiency, (c) Charge injection efficiency as a function of applied potential and (d) stability test for both bare WO_3 and modified WO_3-BN photoanodes under 1 Sun illumination at 1.23V vs RHE.

Part of this chapter has been published in **ACS Appl. Energy Mater. 2019, 2, 7457.**

with hole scavenger. The hole scavenger test proves that BNQD is a superior hole extractor which can extract more number of holes from the WO_3 surface as compared to the hole scavenging action of Na_2SO_3. The hole separation efficiency for the modified WO_3-BN photoanode was reached up to 50%, which is 1.3 times higher than that of bare one (**figure 4.3.8(b)**). Higher charge separation efficiency for modified photoanode confirms the better and faster charge separation due to the incorporation of BNQDs, as a superior hole extractor. Charge injection efficiency for WO_3-BN photoanode was found to be 83%, which is 1.85 times higher than the pristine one (**figure 4.3.8(c)**). The increment in charge separation and injection efficiencies illustrates the photogenerated hole extraction role of BNQDs above the surface of WO_3 nanoblocks which leads to get better water oxidation efficiency. **Figure 4.3.8(d)** is the investigation for the operational stability test of the bare WO_3 as well as the modified WO_3-BN photoanodes in Na_2SO_4 electrolyte at a fixed potential of 1.23V vs. RHE under 1 Sun illumination. Both have similar stabilities and both photoanodes were stabilized approximately after 1h of experiment.

4.3.7 IPCE and Faradaic efficiency

Figure 4.3.9(a) illustrates the IPCE spectra of pristine and modified WO_3 photoanodes at 1.23V vs RHE. For modified WO_3-BN photoanodes, the IPCE value was reached up to 32%, which is 2.1 fold higher than that of bare one. The higher value of IPCE for modified photoanode confirms the effect of charge separation induced by the incorporation of BNQD as a hole extractor. **Figure 4.3.9(b)** corresponds to the evolution of oxygen and hydrogen gas along with the Faradaic

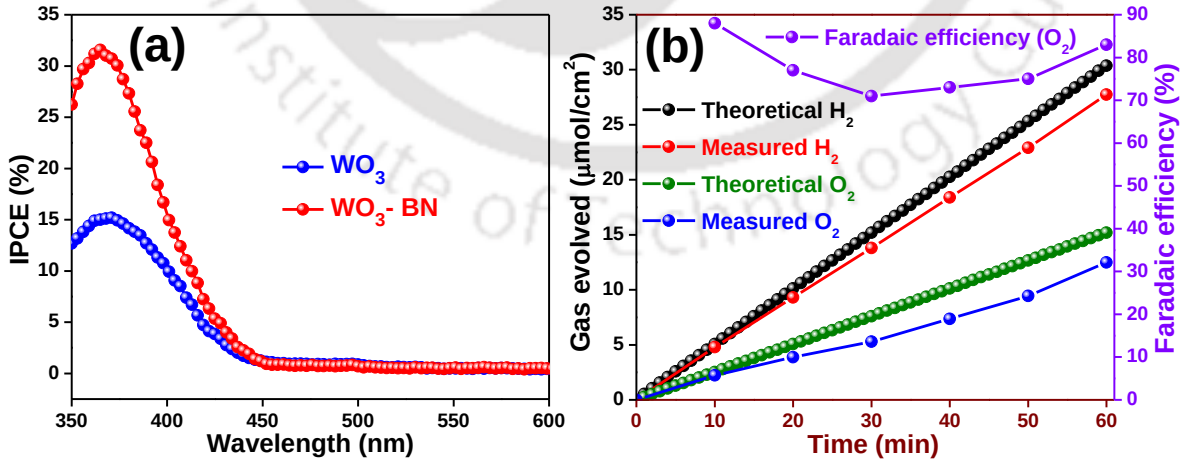

Figure 4.3.9 (a) IPCE spectra for bare WO_3 and WO_3-BN photoanodes and (b) the amount of oxygen and hydrogen gas evolved by WO_3-BN photoanode along with the Faradaic efficiency of WO_3-BN photoanode for water oxidation at a fixed potential of 1.23V vs. RHE under 1 Sun illumination with time.

Part of this chapter has been published in **ACS Appl. Energy Mater. 2019, 2, 7457.**

efficiency O_2 evolution of modified WO_3-BN photoanode. This analysis was carried out through online GC under 1 Sun illumination in 0.1 M Na_2SO_4 electrolyte at a fixed potential of 1.23V vs. RHE. The experimental value of oxygen and hydrogen evolved were compared with the theoretical value of oxygen and hydrogen evolved to get the Faradaic efficiency value. Approximately 83% of Faradaic efficiency was found for water oxidation after 1h.

4.4 CONCLUSIONS

In summary, we have modified the pristine monoclinic WO_3 photoanode by incorporation of an excellent noble hole extracting agent, i.e., BNQDs above the surface of WO_3 nanoblocks. After modification of WO_3 photoanode, the photocurrent density value for the modified WO_3-BN photoanode was found to be 1.63 mA/cm^2, which is approximately 2.4 fold higher than the pristine one. The charge carrier density value for modified WO_3-BN was improved up to 3.2×10^{21} cm^{-3}, which is around 2.44 times higher than that of bare WO_3 photoanode. BNQDs help in better efficient charge separation as well as retard electron-hole recombination. A huge number of holes are available for better water oxidation with faster charge transfer kinetics due to the action of BNQDs. This work offers a magnificent strategy to achieve higher efficiency.

4.5 REFERENCES

1. F. Ronconi, Z. Syrgiannis, A. Bonasera, M. Prato, R. Argazzi, S. Caramori, V. Cristino and C. A. Bignozzi, *J. Am. Chem. Soc.*, 2015, **137**, 4630 – 4633.
2. Y. Li, L. Zhang, R. Liu, Z. Cao, X. Sun, X. Liu and J. Luo, *ChemCatChem*, 2016, **8**, 2765–2770.
3. B. Jin, E. Jung, M. Ma, S. Kim, K. Zhang, J. I. Kim, Y. Son and J. H. Park, *J. Mater. Chem. A*, 2018, **6**, 2585–2592.
4. L. Li, J. Li, J. Bai, Q. Zeng, L. Xia, Y. Zhang, S. Chen, Q. Xu and B. Zhou, *Nanoscale*, 2018, **10**, 18378–18386.
5. L. Sun, Y. Wang, F. Raziq, Y. Qu, L. Bai and L. Jing, *Sci. Rep.*, 2017, **7**, 1303 – 1312.
6. B. Liu, S. Yan, Z. Song, M. Liu, X. Ji, W. Yang and J. Liu, *Chem. – Eur. J.*, 2016, **22**, 18899–18907.
7. Y. Tang, R. Wang, Y. Yang, D. Yan and X. Xiang, *ACS Appl. Mater. Interfaces*, 2016, **8**, 19446–19455.
8. S. Meng, X. Ye, X. Ning, M. Xie, X. Fu and S. Chen, *Appl. Catal., B*, 2016, **182**, 356–368.

Part of this chapter has been published in **ACS Appl. Energy Mater. 2019, 2, 7457.**

9. Y. Yang, C. Zhang, D. Huang, G. Zeng, J. Huang, C. Lai, C. Zhou, W. Wang, H. Guo, W. Xue, R. Deng, M. Cheng and W. Xiong, *Appl. Catal., B*, 2019, **245**, 87–99.
10. X. Fu, Y. Hu, Y. Yang, W. Liu and S. Chen, *J. Hazard. Mater.*, 2013, **244**, 102–110.
11. M. K. Mohanta, T. K. Sahu and M. Qureshi, *Chem. – Asian J.*, 2020, **15**, 3886–3896.
12. B. Huo, B. Liu, T. Chen, L. Cui, G. Xu, M. Liu and J. Liu, *Langmuir*, 2017, **33**, 10673-10678.
13. V. B. Kumar and D. Mohanta, *Bull. Mater. Sci.*, 2011, **34**, 435–442.
14. B. Singh, G. Kaur, P. Singh, K. Singh, B. Kumar, A. Vij, M. Kumar, R. Bala, R. Meena, A. Singh, A. Thakur and A. Kumar, *Sci. Rep.*, 2016, **6**, 35535.
15. Y. Y. Bu, J. Ren, H. W. Zhang, D. J. Yang, Z. Y. Chen and J. P. Ao, *J. Mater. Chem. A*, 2018, **6**, 8604–8611.
16. N. Zhang, C. Chen, Z. Mei, X. Liu, X. Qu, Y. Li, S. Li, W. Qi, Y. Zhang and J. Ye, *ACS Appl. Mater. Interfaces*, 2016, **8**, 10367–10374.
17. R. Zhang, Y. Fang, T. Chen, F. Qu, Z. Liu, G. Du, A. M. Asiri, T. Gao and X. Sun, *ACS Sustainable Chem. Eng.*, 2017, **5**, 7502–7506.

CHAPTER 5

Surface charge directed borophene - phosphorous nitride heterojunction formation for enhanced electrochemical performance in tungsten oxide based photoanodes

This chapter determines the widely explored zero-dimensional (0D) non-metal based materials for photoelectrochemical (PEC) electrode modification due to their faster charge transfer and better light harvesting abilities. Herein, we have designed a complimentary charged nanosized 0D-0D hybrid assemble of positively charged phosphorous nitride dots (PNDs) and negatively charged borophene dots (BDs) having favorable type-II heterojunction approach among them. A model system has been studied using WO_3 as a semiconductor for showing the effectiveness of PNDs-BDs for PEC water oxidation. The oppositely charged 0D-0D hybrid model provides rapid carrier separation along with minimized carrier recombination to metal oxide based semiconductor for enhanced PEC water oxidation.

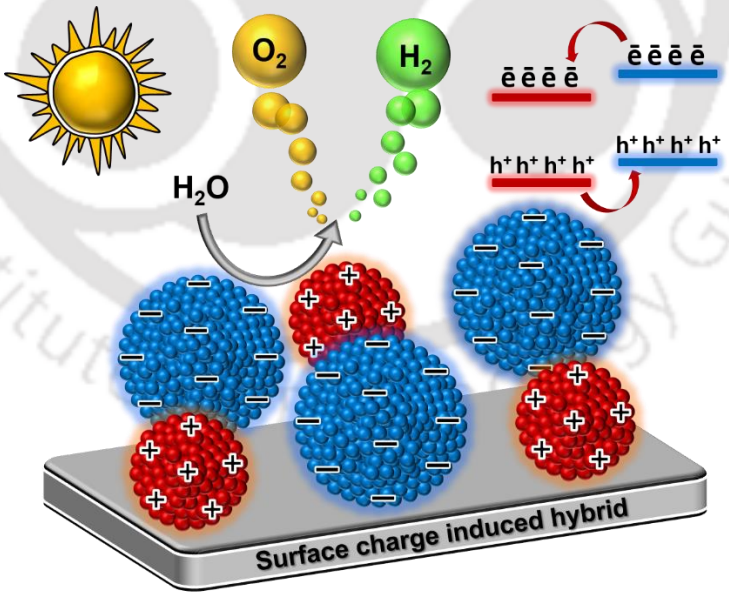

ChemComm

M. K. Mohanta *et al.*, 2023, **59**, 1955

5.1 INTRODUCTION

As per discussion in the previous chapter, the heterojunction approach for better charge separation can enhance the photoelectrochemical performance of WO_3 photoanode.[1-3] In recent times, non-metal based quantum dots (QDs) incorporation over PEC photoanodes have been widely explored for their faster charge transfer and better light harvesting behavior. Zheng et al. have achieved faster charge separation and transportation by the incorporation of black phosphorus QDs above TiO_2 surface.[4] Kai-Hang Ye et al. have broadened the light absorption range of $BiVO_4$ by modification with carbon QDs to achieve higher photoanodic performance.[5] Boron nitride QDs with hexagonal phase has received greater attention for its hole extracting ability to minimize the photogenerated carrier recombination in the semiconductors.[6,7] The edge effect is the major advantage of these nanodots (0D), which leads the more charge accumulation compared to their corresponding 2D morphologies. These 0D nanodots provide superior light absorption, faster charge separation with minimized charge recombination and tunable surface for efficient PEC performance.[8] Similarly, phosphorus nitride (PN), another metal-free semiconductor having favorable band alignments and bandgap (~ 3.2 eV) has the potential to exhibit better performance.[9-11] Atomically thin 2D boron (B), also called "borophene", has been considered to be another promising 2D alternative in semiconductor industries such as batteries and supercapacitors, etc. Borophene has fascinating physical and chemical properties, high carrier mobility, tunable bandgap, superconductivity and high chemical stability.[12-15] To date, widely investigated boron nanostructures having low dimensions corresponds to nano-cones (2D), nanotubes (1D), nanowires (1D), nanosheets (2D) and nanoribbons (2D).[16] The synthesis and applications of 0D boron dots are reported sparsely. Herein, we have designed a type II heterojunction model between PN and borophene by synthesizing 0D crystalline PN dots (PNDs) and amorphous 0D borophene dots (BDs). Interestingly, these PNDs-BDs hybrid catalysts are having a complementary electrostatic attraction i.e. positively surface-charged PNDs and negatively surface-charged BDs. Further, we have designed a hybrid model of WO_3 photoanode for enhanced PEC water oxidation application using PNDs-BDs hybrid. Due to the band energy positions, there is type-II heterojunction formation between bare WO_3 and the PNDs-BDs hybrid system.

Part of this chapter has been published in **Chem. Commun. 2023, 59, 1955**.

5.2 EXPERIMENTAL METHODS

5.2.1 Synthesis of nano-sized phosphorus nitride dots (PNDs)

The PNDs were synthesized by the solvothermal method.[11] In a typical synthesis, 20 mg phosphonitrilic chloride trimer (PCT) were mixed with 20 mL ethanol and transferred into a Teflon-lined autoclave and treated at 180 °C for 12 h. After the completion of the hydrothermal reaction, this autoclave was allowed to cool down at room temperature and the obtained solution was filtered through 0.22 μm syringe filter, in order to separate the larger particles. The obtained PNDs were kept at room temperature for further use.

5.2.2 Synthesis of 0D borophene Dots (BDs)

BDs were synthesized by two steps, i.e., sonication and hydrothermal methods. In the first step, 30 mL of DMF solution containing 30 mg of boron powder was ultrasonicated at 400 W for 5 h to obtain the 2D sheets.[16] Afterwards, the solution was centrifuged for 30 min at 1500 rpm. The brown-colored surfactant containing 2D borophene was decanted to a 50 mL Teflon-lined stainless autoclave for 12h thermal reaction at 180 °C. After the reaction, the suspension was cooled down and filtered through a syringe filter of 0.22 μm to collect the desired size of 0D BDs.

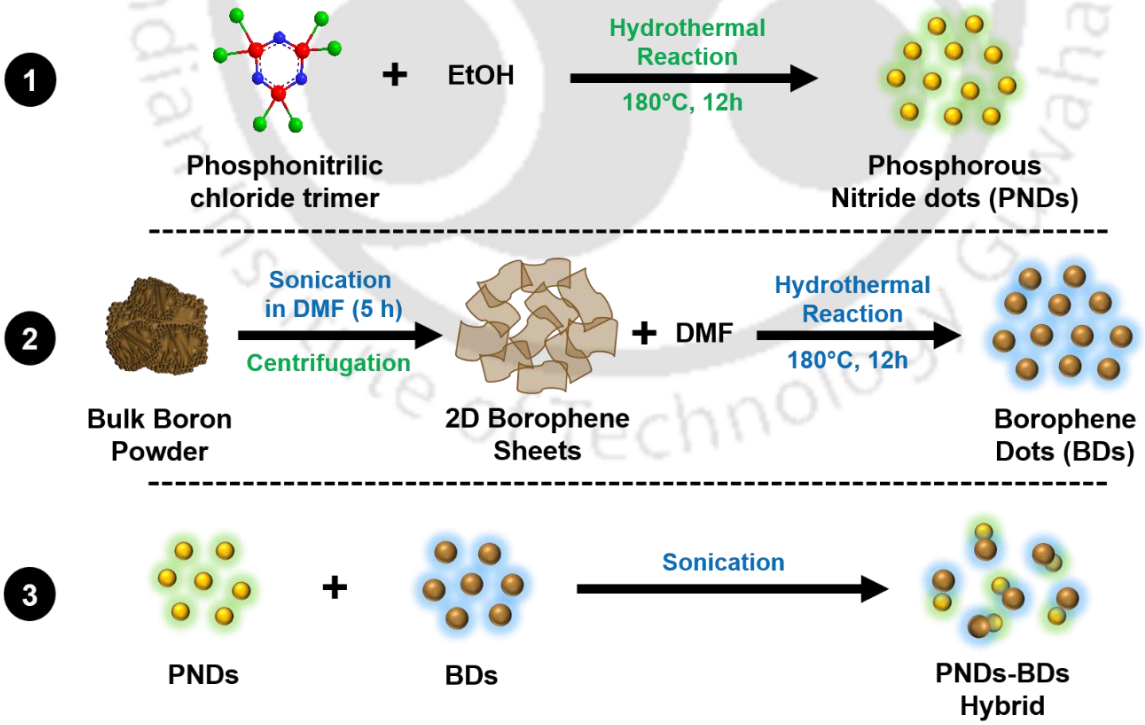

Scheme 5.2.1 Step wise synthesis of phosphorous nitride nanodots, borophene nanodots and hybrid nanodots of phosphorous nitride and borophene, respectively.

Part of this chapter has been published in **Chem. Commun. 2023, 59, 1955**.

5.2.3 Preparation of PND-BDs hybrid

The PNDs-BDs hybrids were prepared by adding 1 ml of BDs solution to 1 ml of PNDs solution and sonicated for 10 min. The obtained hybrid nanodots were kept at room temperature for further experiments. A detailed schematic of PNDs, BDs and PNDs-BDs hybrid synthesis has been given below in **scheme 5.2.1**.

5.2.4 Synthesis of WO_3 photoanode

Nanoblock-featured WO_3 photoanode was synthesized directly over fluorine-doped tin oxide (FTO) followed by the hydrothermal process.[3] Firstly, two different 15 mL aqueous precursor solutions of sodium tungsten dihydrate ($Na_2WO_4 \cdot 2H_2O$) (0.125 g) and ammonium oxalate monohydrate ($(NH_4)_2C_2O_4 \cdot H_2O$) (0.118 g) were prepared in distilled water. After 30 min of stirring, the colorless tungsten precursor solution was converted to white suspension by dropwise addition of 3M HCl (5 mL), which was again converted to clear solution by adding ammonium oxalate precursor solution to it. After half an hour of stirring, the final mixture was decanted to a 50 mL Teflon-lined stainless autoclave for 8h thermal reaction at 140 °C, having well-placed FTOs with conducting side faced down. Afterward, the in-situ grown WO_3 samples were cleaned properly with deionized water and dried in the oven at 60 °C for 30 min. The WO_3 substrates were annealed at 500 °C in a muffle furnace for 1 hour to obtain WO_3 thin films with a monoclinic phase.

5.2.5 Preparation of WO_3/PNDs, WO_3/BDs and WO_3/PNDs-BDs photoanodes

WO_3 photoanodes were prepared according to a reported chemical bath deposition (CBD) method. As prepared WO_3 photoanodes were sensitized in a fixed concentration of PNDs and BDs solution separately for 10 h at room temperature to fabricate WO_3/PNDs and WO_3/BDs, respectively. After the sensitization process, the films were cleaned with DI water to remove the excess PNDs and BDs at the surface of WO_3 photoanodes. Then the films were then dried at 100°C for 6 h. In order to fabricate WO_3/PNDs-BDs photoanodes, the same CBD process was followed by immersing those WO_3/PNDs photoanodes to BDs solutions for 10h. A detailed schematic of bare WO_3 and composite WO_3/PNDs-BDs photoanodes fabrication has been given below in **scheme 5.2.2**.

Part of this chapter has been published in **Chem. Commun. 2023, 59, 1955**.

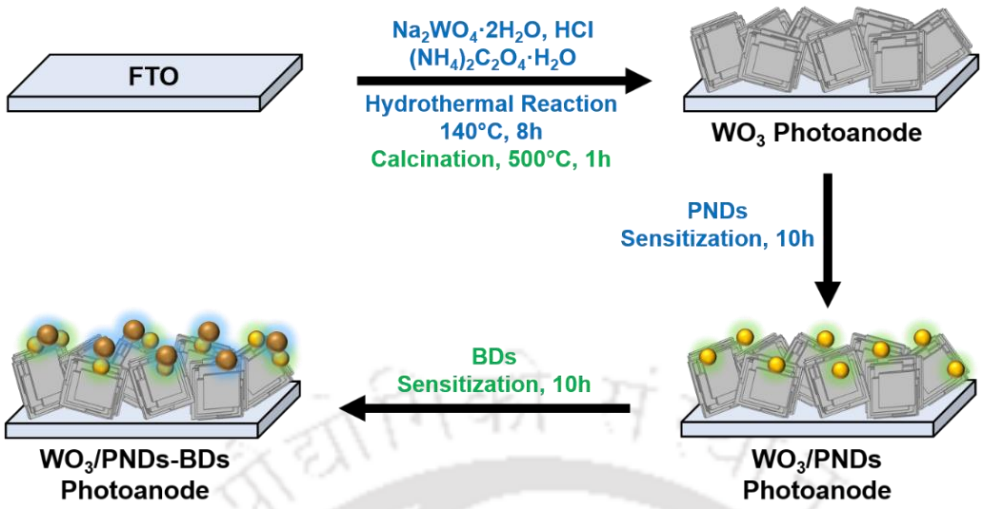

Scheme 5.2.2 Step-wise fabrication of bare WO_3 and composite WO_3/PNDs-BDs photoanodes.

5.2.6 Fabrication of PNDs photoelectrode

1mL of PNDs (1 mg/mL) solution in ethanol was mixed with 50 μL of Nafion and sonicated for 1 h to make a uniform solution. 50 μL of the above solution was drop-casted over a cleaned FTO substrate and dried at 60 °C for 2 h. This procedure was repeated four times to make the PNDs film. After the drop-casting and drying process, the films were heated at 100 °C for 3 h to obtain the PNDs photoelectrode film.

5.2.7 Fabrication of BDs photoelectrode

1mL of BDs (1 mg/mL) solution in DMF was mixed with 50 μL of Nafion and sonicated for 1 h to make a uniform solution. 50 μL of the above solution was drop-casted over a cleaned FTO substrate and dried at 60 °C for 2 h. This procedure was repeated four times to make the BDs film. After the drop-casting and drying process, the films were heated at 100 °C for 3 h to obtain the BDs photoelectrode film.

5.2.8 Fabrication of PNDs-BDs photoelectrode

Firstly, 50 μL of the above PNDs solution was drop-casted over a cleaned FTO substrate and dried at 60 °C for 2 h. This procedure was repeated two times to make the PNDs film. Secondly, 50 μL of the above BDs solution was drop-casted over the PNDs film and dried at 60 °C for 2 h. This procedure was repeated two times to make the BDs film. After the drop-casting and drying process, the films were heated at 100 °C for 3 h to obtain the PNDs-BDs photoelectrode film.

Part of this chapter has been published in **Chem. Commun. 2023, 59, 1955**.

5.3 RESULTS AND DISCUSSION

5.3.1 Analysis for PNDs and BDs (XRD, FETEM and XPS analysis)

Synthesis of PNDs and BDs has been evidenced by structural, crystalline and electronic structure analysis as shown in figure 1. From XRD analysis, the peaks related to PNDs were well defined with cubic phase (**figure 5.3.1**).[11] The well-dispersed PNDs with average particle size of 6 nm was confirmed from FETEM analysis (**figure 5.3.2(a)**). The HRTEM analysis provides an interplanar spacing of 0.19 nm corresponding to (200) crystal plane of PNDs (**figure 5.3.2(b)**). The high-resolution X-ray photoelectron spectroscopy (XPS) data shows the chemical states of individual elements P and N with electronic interactions, as shown in **figure 5.3.2(e)** and **figure 5.3.2(f)**. The complete XPS analysis with the binding energies were corrected with respect to C 1s i.e., 284.8 eV. The XPS core-level spectra of P 2p for PNDs is shown in figure 1(e). The binding energy of 133.8 eV in PNDs corresponds to N−P=N, π-conjugated system having P and N elements.[17] The P 2p core-level spectra was fitted with assigned peaks of $2p_{3/2}$ at 133.6 eV and $2p_{1/2}$ at 134.5 eV, respectively. Similarly, **figure 5.3.2(f)** provides the N 1s spectra of PNDs having two peaks at 399.8 eV related to the N-P bond and 401.2 eV related to N-O.[18,19]

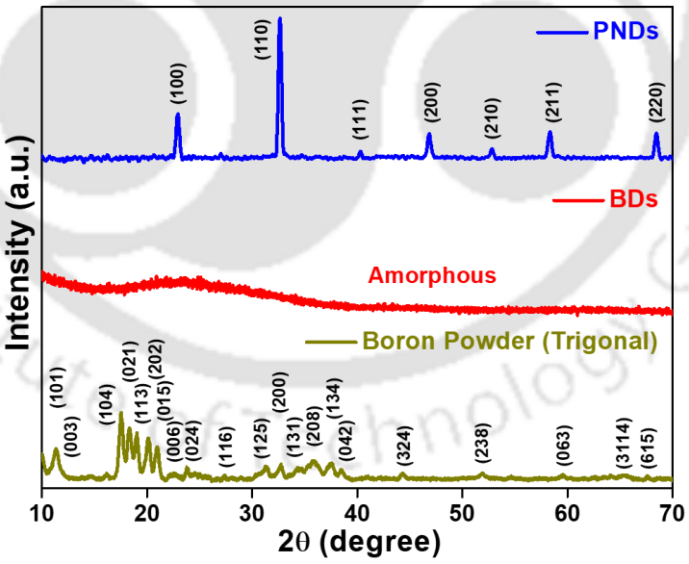

Figure 5.3.1 XRD analysis of phosphorous nitride dots (PNDs), boron powder and borophene dots (BDs).

From XRD analysis, boron powder is indexed to JCPDS no 48-0083. The BDs were found to be X-ray amorphous in nature (**figure 5.3.1**). The FETEM analysis confirms that the average particle size of dispersed BDs i.e., 10 nm (**figure 5.3.2(c)**). **Figure 5.3.2(d)** represents the HRTEM

Part of this chapter has been published in **Chem. Commun. 2023, 59, 1955**.

analysis of BDs, with diffused ring pattern in selected area electron diffraction (SAED) indicating the amorphous nature of BDs. **Figure 5.3.2(g)** provides the high-resolution B 1s core level XPS spectra of BDs. The binding energies of well-agreeing Gaussian peaks for B-N and B-O bond were found to be at 188.8 eV and 192.5 eV.[19]

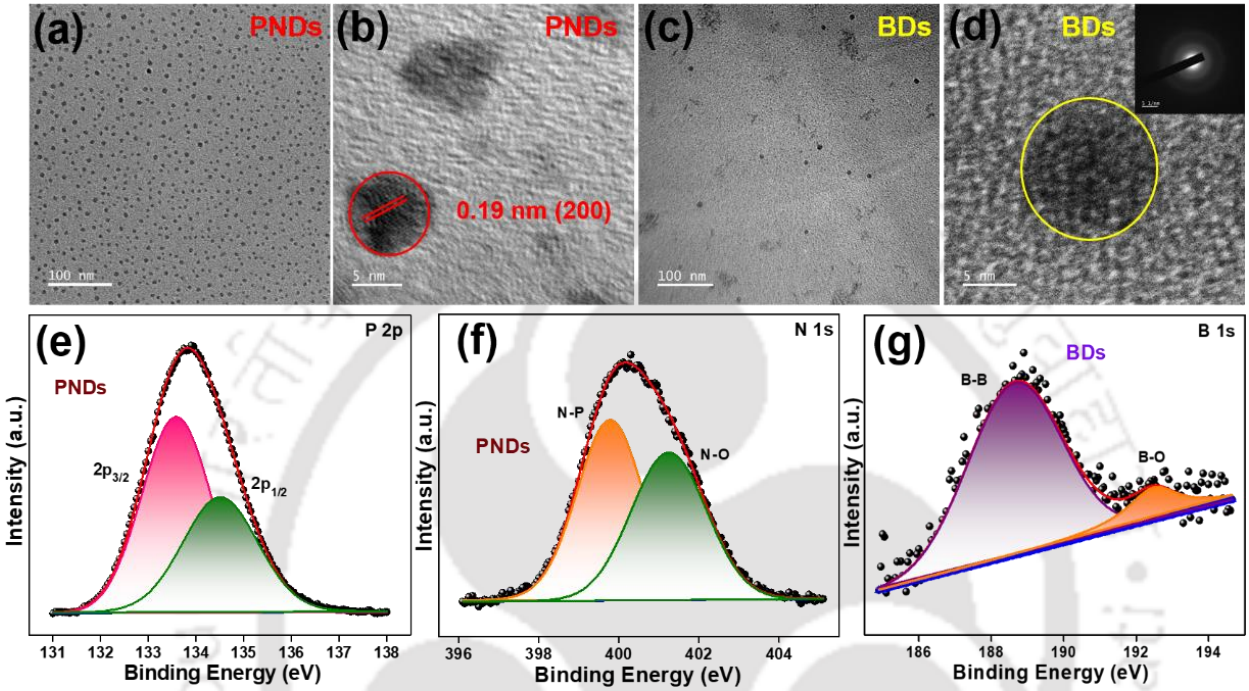

Figure 5.3.2 (a) FETEM and (b) HRTEM image of PNDs; (c) FETEM and (d) HRTEM image of BDs; Core level XPS spectra of (e) P 2p, (f) N 1s and (g) B 1s for PNDs and BDs.

5.3.2 Analysis for formation of PNDs-BDs hybrid (XRD, FETEM and XPS analysis)

The prepared hybrid nanodots of PNDs and BDs were confirmed by the FETEM and XPS analysis as shown in **figure 5.3.3**. **Figure 5.3.3(a)** is the FETEM of the PNDs-BDs hybrid and **figure 5.3.3(b)** represents the HRTEM images of the hybrid nanodots i.e., PNDs-BDs. The interplanar spacing of 0.19 nm within the yellow-colored circle corresponding to (200) crystal plane of PNDs and the dark spot within the red-colored circle corresponding to amorphous BDs, evidences the unaffected structural features of PNDs and BDs. The surface charge analysis of PNDs, BDs and the hybrid nanodots was carried out through zeta potential measurements, as shown in **figure 5.3.3(c)**. A positive surface charge potential of $\varsigma = +9.5$ mV and a negative surface charge potential of $\varsigma = -26.2$ mV were found for PNDs and BDs, respectively. These PNDs and BDs tend to form a heterojunction due to the columbic interactions via their oppositely charged surfaces, which is confirmed from HRTEM analysis (**figure 5.3.3(b)**) as well as the zeta potential

Part of this chapter has been published in **Chem. Commun. 2023, 59, 1955**.

values of the fused PNDs and BDs which is compensated to a net value of -11.5 mV. The presence of the characteristic peaks for P 2p (**figure 5.3.3(d)**), N 1s (**figure 5.3.3(e)**) and B 1s (**figure 5.3.3(f)**), confirms the existence of PNDs and BDs in the hybrid system. The shift in peak positions of P 2p, N 1s and B 1s towards higher binding energy indicates the component interactions in the PNDs-BDs hybrid.

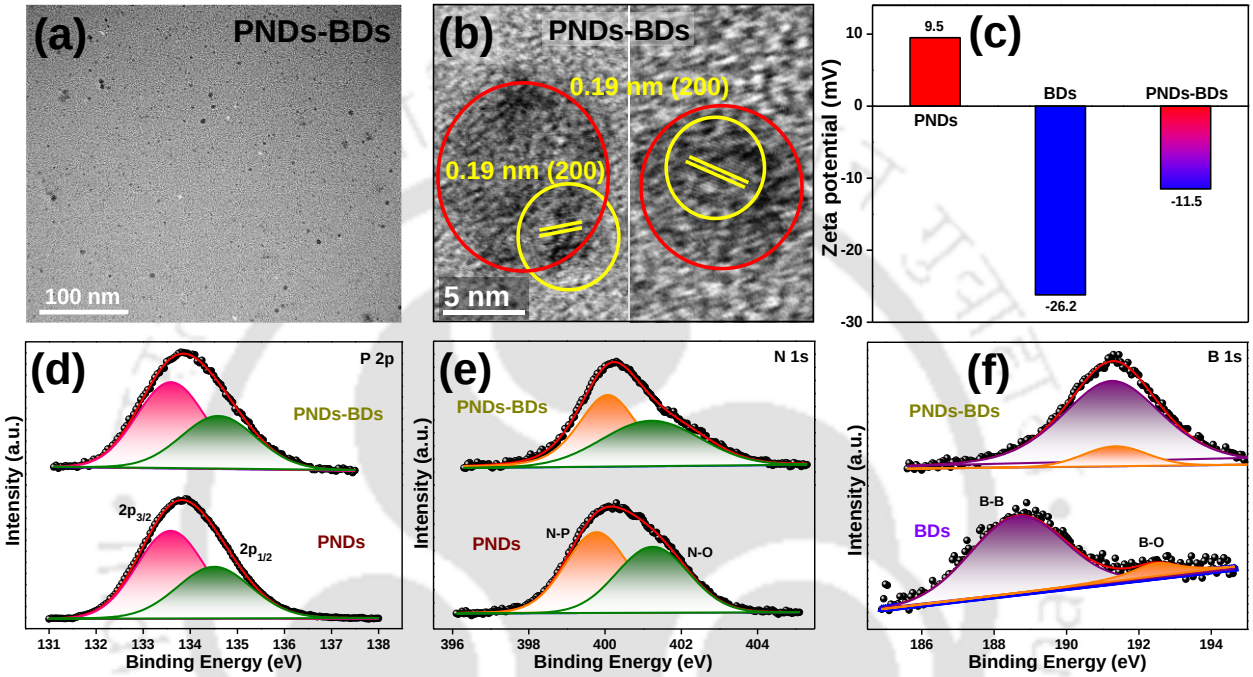

Figure 5.3.3 (a) FETEM and (b) HRTEM images of PNDs-BDs hybrid; (c) Zeta potential (ς) measurements of PNDs, BDs and PNDs-BDs hybrid; Core level XPS spectra of (d) P 2p, (e) N 1s and (f) B 1s for PNDs-BDs hybrid.

5.3.3 UV-visible absorption spectra, Tauc plot, PL and TRPL spectra analysis for PNDs, BDs and PNDs-BDs hybrid

In order to investigate the optical response with respect to the band gap of PNDs and BDs, the UV-visible absorption spectra, Tauc analysis and steady-state and dynamic PL spectra were analyzed. The absorption peaks for PNDs and BDs were recorded to be at 348 nm and 354 nm, respectively (**figure 5.3.4(a)**). These absorption peaks are related to the bandgaps of 3.06 eV and 3.26 eV for PNDs and BDs, respectively (**figure 5.3.4(b)**).

The photoluminescence (PL) and time-resolved photoluminescence (TRPL) with corresponding decay analysis have been performed to know the charge transfers between PNDs and BDs (**figure 5.3.5**). Both PNDs and BDs show blue emission peaks at around 424 nm and 457 nm, with the PNDs-BDs hybrid shows a blue emission peak at 438 nm (**figure 5.3.5(a)**).

Part of this chapter has been published in **Chem. Commun. 2023, 59, 1955**.

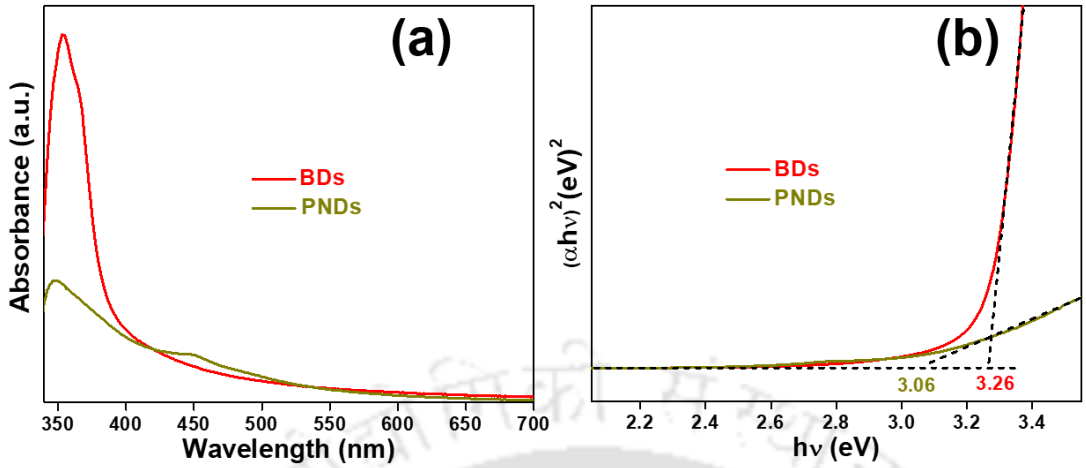

Figure 5.3.4 (a) UV-visible absorption spectra and the corresponding (b) Tauc's plots of PNDs and BDs.

The decay patterns have been fitted with a bi-exponential function and the average lifetime of these nanodots can be calculated as follows:

$$< \tau > = \frac{a_1\tau_1^2+a_2\tau_2^2}{a_1\tau_1+a_2\tau_2} \quad \text{.....(5.1)}$$

The average lifetime of PNDs and BDs were calculated to be 3.99 and 8.48 ns, respectively (**figure 5.3.5(b)**). The average lifetime of PNDs-BDs hybrid was calculated to be 5.83 ns, which is differed from the average lifetime of PNDs and BDs. These change in average lifetime suggests a possible charge transfer among PNDs and BDs in PNDs-BDs hybrid. The fitted parameters related to the lifetime of different nanodots and their hybrid composite are given below in **table 5.3.1**.

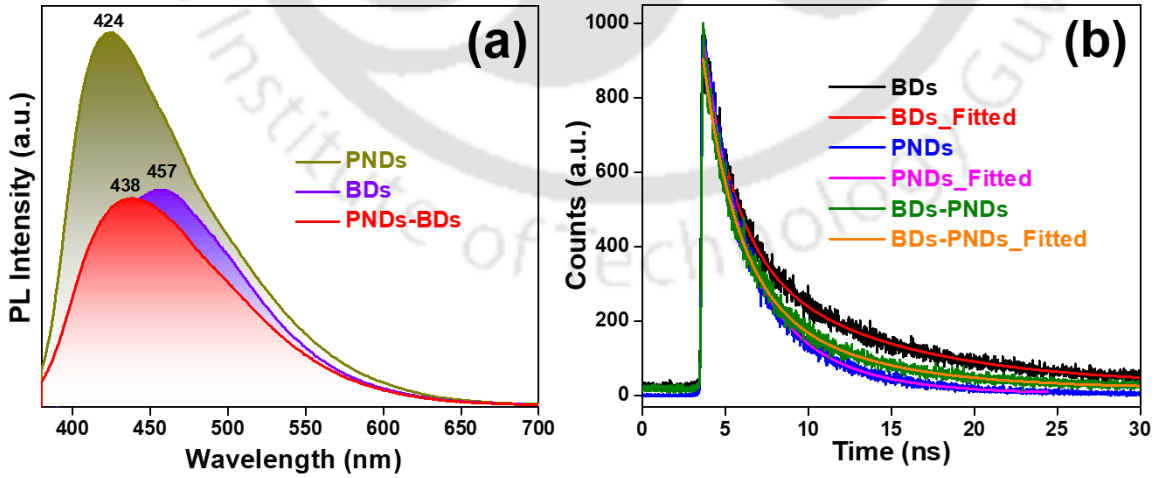

Figure 5.3.5 (a) Photoluminescence (PL) and (b) Time-resolved photoluminescence (TRPL) spectra of PNDs, BDs and PNDs-BDs hybrid.

Part of this chapter has been published in **Chem. Commun. 2023, 59, 1955**.

Table 5.3.1 TRPL fitted parameters of PNDs, BDs and PNDs-BDs hybrid.

Materials	τ_1	τ_2	α_1	α_2	$\langle\alpha\rangle$ (ns)
PNDs	1.798	4.419	32.224	67.776	3.99
BDs	1.915	9.137	32.369	67.631	8.48
PNDs-BDs hybrid	1.963	6.669	42.361	57.639	5.83

5.3.4 Band position analysis for PNDs-BDs hybrid

The XPS valence band spectra of PNDs and BDs were analyzed to gain insight into the band positions which leads to the carrier movement across the hybrids, are shown in **figure 5.3.6**. The valence bands (VB) for PNDs and BDs were noted to be at 2.8 eV and 2.5 eV. The bandgap energies of PNDs and BDs were fixed from the UV-visible absorption spectra. The above analysis confirms the conduction band (CB) positions of PNDs and BDs at – 0.3 eV and – 0.8 eV, respectively with reference to the vacuum level. The type-II heterojunction approach between PNDs and BDs was determined from the band position analysis (**figure 5.3.7(a)**). Based on the FETEM, band position and zeta potential analysis, a probable type-II heterojunction based electrostatic interactions between positively surface-charged PNDs and negatively surface-charged BDs has been shown in **figure 5.3.7(b)**.

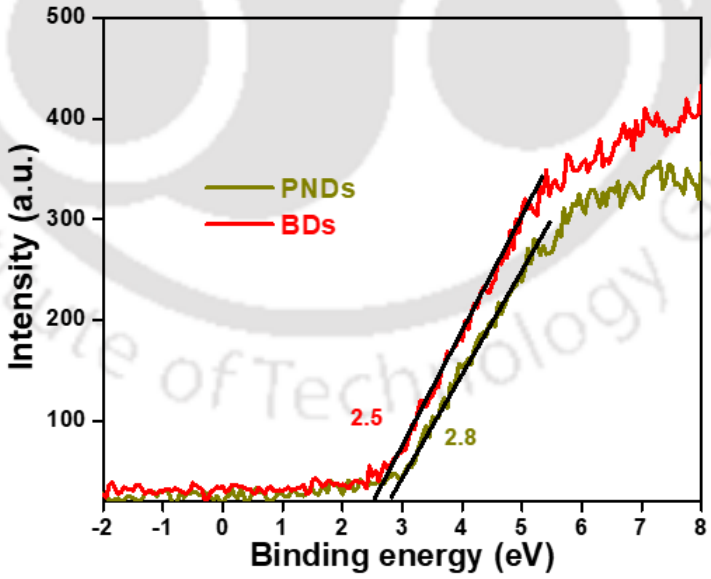

Figure 5.3.6 XPS valence band spectra of PNDs and BDs.

Part of this chapter has been published in **Chem. Commun. 2023, 59, 1955**.

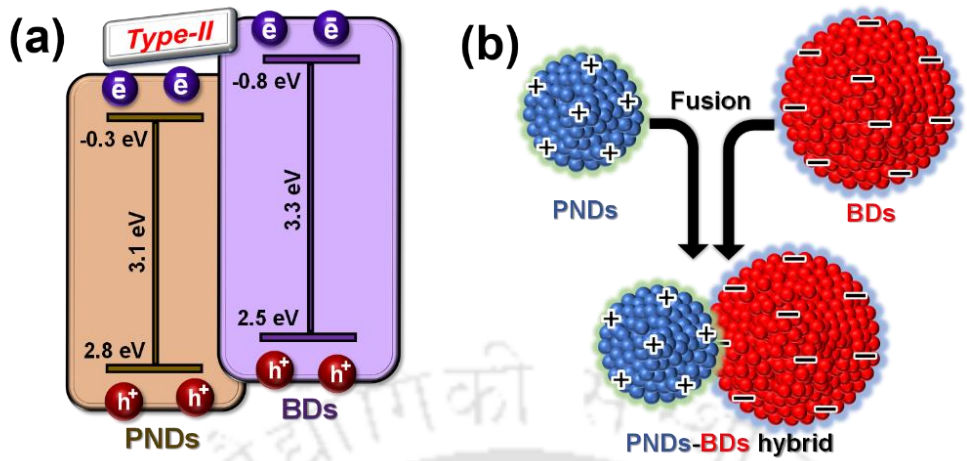

Figure 5.3.7 (a) schematic band position analysis of PNDs and BDs; (b) schematic of type-II heterojunction based electrostatic attraction between PNDs and BDs.

5.3.5 Analysis of WO_3/PNDs-BDs composite (XRD, FETEM and XPS analysis)

The above type-II heterojunction based charge transfer interactions of PND and BDs have been applied to PEC water oxidation based application using WO_3 as a metal oxide based model semiconductor. Synthesis of WO_3 and the composite WO_3/PNDs-BDs photoanodes has been confirmed through structural, morphological and electronic state analysis. The peaks of bare WO_3 photoanode are matched with peaks of JCPDS no. 01-072-0677, which confirms the monoclinic phase of WO_3 (**figure 5.3.8**).

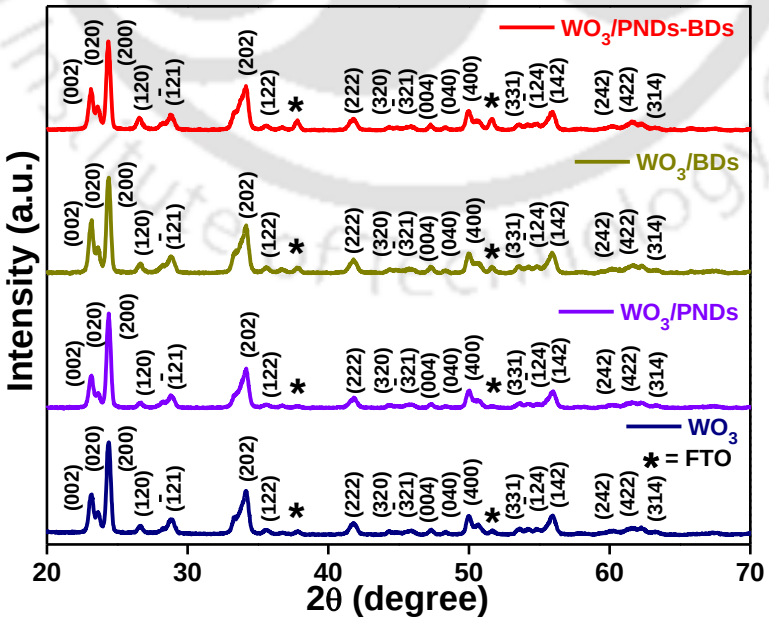

Figure 5.3.8 XRD analysis of WO_3, WO_3/PNDs, WO_3/BDs and WO_3/PNDs-BDs photoanodes.

Part of this chapter has been published in **Chem. Commun. 2023, 59, 1955**.

FESEM image of bare WO_3 thin film evidences the uniformly grown block-shaped WO_3 with an average size of 800 nm above the FTO surface (**figure 5.3.9(a)**). Morphology of WO_3 photoanode was not altered with PNDs, BDs and PNDs-BDs hybrid modifications, as shown in **figures 5.3.9(b)**, **figure 5.3.9(c)** and **figure 5.3.9(d)**. **Figure 5.3.9(b)** and **figure 5.3.10(a)** are the

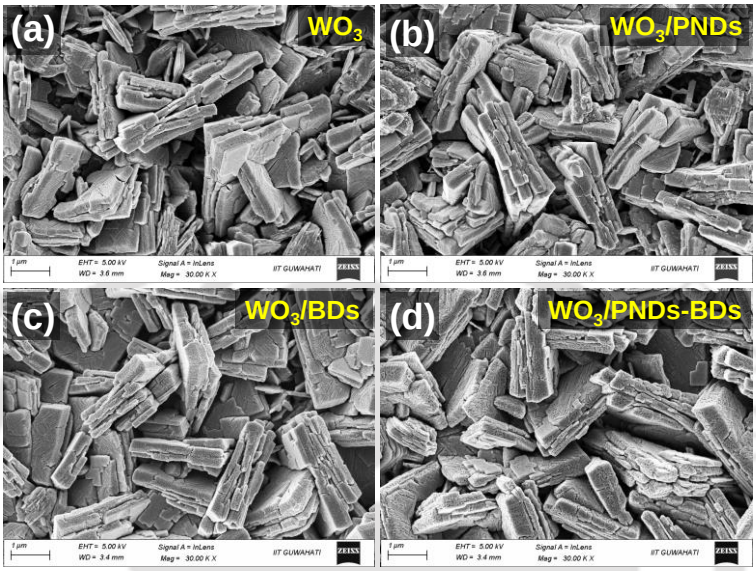

Figure 5.3.9 FESEM image of (a) WO_3, (b) WO_3/PNDs, (c) WO_3/BDs; and WO_3/PNDs-BDs photoanode.

FETEM images of the WO_3/PNDs-BDs composite photoanode. The HRTEM image of the composite shows 0.37 nm d-spacing related to (200) plane of WO_3 and 0.19 nm d-spacing related to (200) plane of PNDs (**figure 5.3.10(b)**). Uniformly distributed individual W, O, P, N and O elements were confirmed from the elemental mapping by scanning transmission electron microscopy (STEM) (**figure 5.3.10(i)-(vi)**).

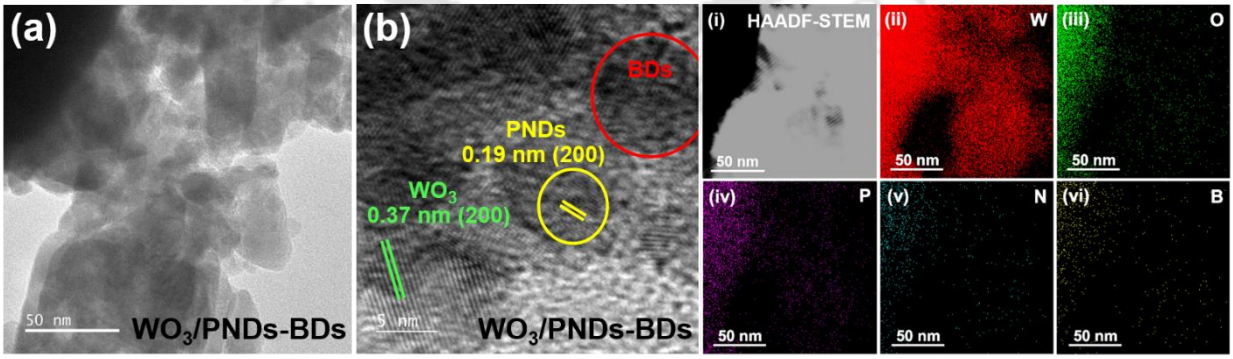

Figure 5.3.10 (a) FETEM and (b) HRTEM images of WO_3/PNDs-BDs composite; (i) STEM image and corresponding individual EDS mapping figures of WO_3/PNDs-BDs having (ii) W, (iii) O, (iv) P, (v) N , (vi) B.

Part of this chapter has been published in **Chem. Commun. 2023, 59, 1955**.

The peaks at 35.77 eV for $4f_{7/2}$ and 37.79 eV for $4f_{5/2}$ attributes to the +6 oxidation state of W in WO_3 photoanode (**figure 5.3.11(b)**). The O 1s spectra of WO_3 is having two signals at 530.17 eV related to lattice oxygen (O_L) and 531.35 eV related to oxygen vacancies (O_V) (**figure 5.3.11(c)**). **Figure 5.3.11(a)** represents the XPS survey spectra of composite photoanode having the corresponding characteristic signals of W, O, P, N and B. A small shift in positions of $4f_{7/2}$, $4f_{5/2}$, and O_L towards lower binding energies indicates the electronic interactions within the base semiconductor and the nanodots. Also, the shift in signals of other elements P, N and B for WO_3/PNDs-BDs photoanode compared to PNDs, BDs and PNDs-BDs hybrid proves the electronic interactions among those components of the composite (**figure 5.3.11(d)**, **figure 5.3.11(e)**, **figure 5.3.11(f)**).

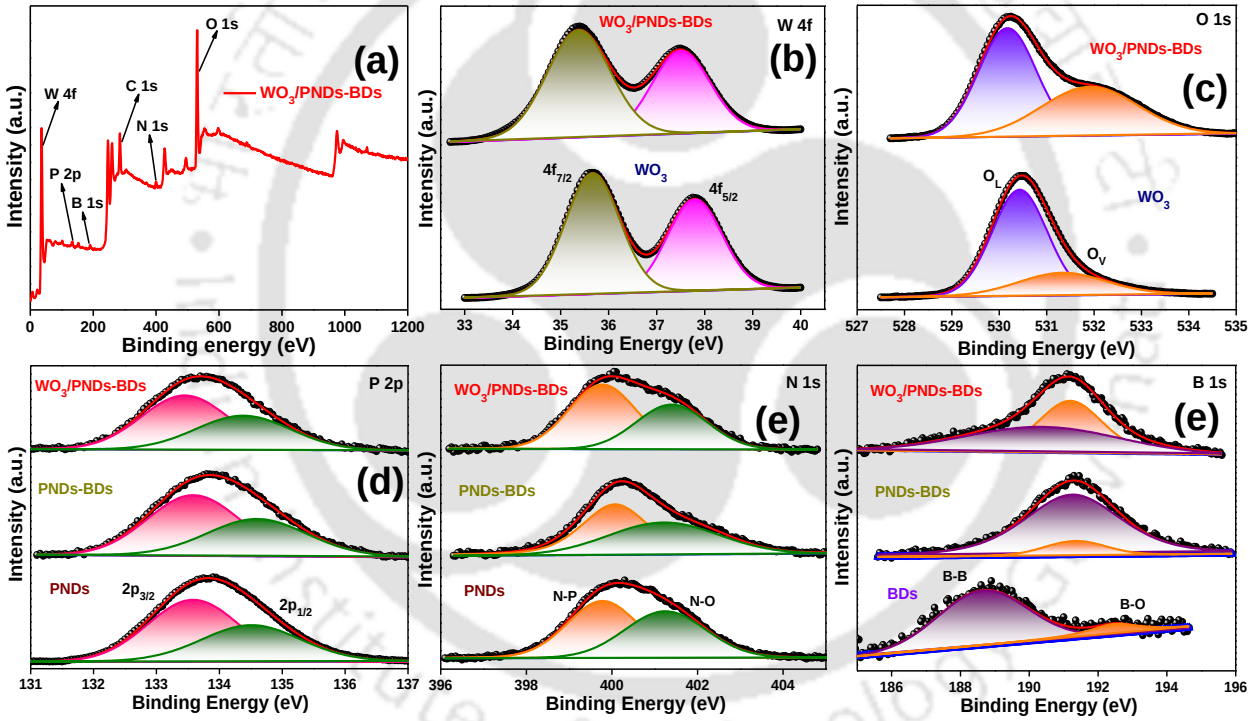

Figure 5.3.11 (a) XPS survey spectra of fabricated WO_3/PNDs-BDs photoanode; Core level XPS spectra of (b) W 4f, (c) O 1s (d) P 2p, (e) N 1s and (f) B 1s.

5.3.6 UV-visible absorption spectra, Tauc plot and TRPL spectra analysis for WO_3/PNDs-BDs composite

The absorption edges and bandgaps for bare and other modified photoanodes were noted to be at ~ 393 nm and ~ 2.82 eV, respectively, which indicates that the modification with PNDs and BDs doesn't have any impact on the optical properties of WO_3 photoanode (**figure 5.3.12**).

Part of this chapter has been published in **Chem. Commun. 2023, 59, 1955**.

The average lifetime of the composite photoanode was calculated to be 5.32 ns, which was reduced by 2.2 times compared to the average lifetime of pristine WO_3 photoanode, i.e., 11.61 ns (figure 5(d)). These lifetime decay results evidence the enhanced charge transfer activities among WO_3, PNDs and BDs in composite photoanode. The fitted parameters related to the lifetime of different photoanodes are given below in **table 5.3.2**.

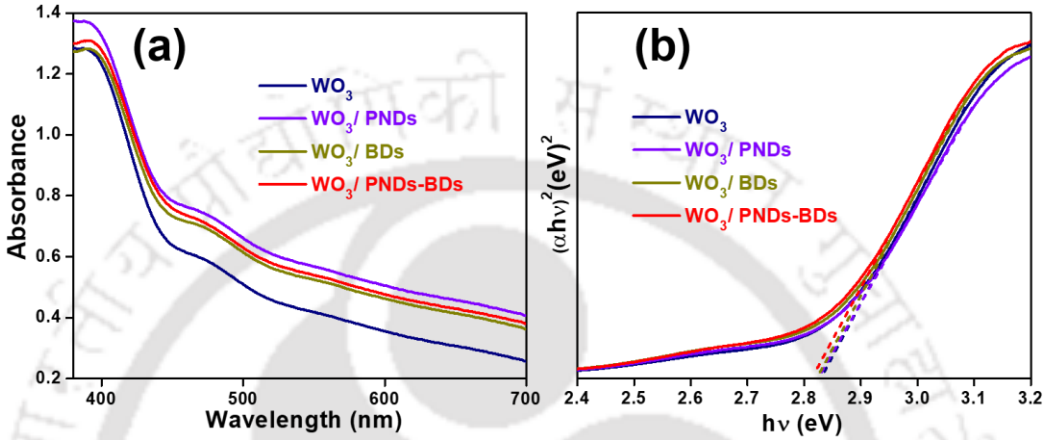

Figure 5.3.12 (a) UV-visible absorption spectra and the corresponding (b) Tauc's plots of WO_3, WO_3/PNDs, WO_3/BDs and WO_3/PNDs-BDs photoanodes.

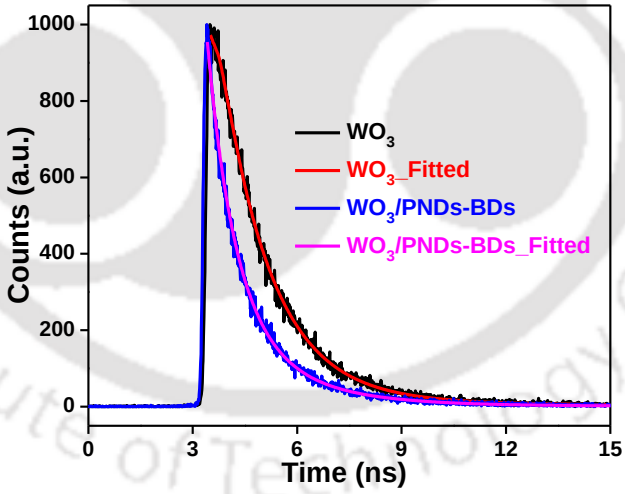

Figure 5.3.13 TRPL spectra of WO_3 and WO_3/PNDs-BDs photoanodes.

Table 5.3.2 TRPL fitted parameters of WO_3 and WO_3/PNDs-BDs photoanodes.

Photoanode	τ_1	τ_2	α_1	α_2	$\langle\alpha\rangle$ (ns)
WO_3	1.429	6.673	91.506	8.494	11.61
WO_3/PNDs-BDs	0.805	2.113	71.384	28.616	5.32

Part of this chapter has been published in **Chem. Commun. 2023, 59, 1955**.

5.3.7 Photoelectrochemical characterizations

To know the photoelectrochemical activity of PNDs and BDs with WO_3 photoanode, linear sweep voltammetry (LSV) measurements of the pristine and altered photoanodes were carried out under 1 Sun illumination in presence of neutral medium (pH=6) 0.1 M Na_2SO_4 electrolyte (**figure 5.3.14(a)**). Pristine monoclinic WO_3 photoanode results only 0.7 mA/cm^2 current density at 1.23 V vs RHE, which is too low in comparison to the theoretical current density (~ 4.0 mA/cm^2)value for WO_3 photoanode. WO_3 photoanode with PNDs sensitization results a 1.5 mA/cm^2 current density at 1.23 V vs RHE, which indicates the minimization of photogenerated electron-hole recombination rate. The type-II heterojunction between WO_3 and PNDs provides 2 fold increment in current density with better carrier separation and minimized carrier recombination.[11] The BDs sensitized WO_3 photoanode results a 2.4 times enhanced (1.7 mA/cm^2) current density at 1.23 V vs RHE in comparison to bare WO_3 photoanode, which evidences the improved photogenerated carrier separation. The hybrid dots sensitized (i.e., PNDs and BDs) WO_3 photoanode gives a maximum current density of 2.8 mA/cm^2 @ 1.23 V vs RHE. The optimization of BDs loading over WO_3/PNDs photoanodes has been provided in **figure 5.3.14(b)**. A high 4 fold increment in current density of WO_3 photoanode due to PNDs and BDs sensitizations resulted in maximized charge separation and minimized charge recombination towards high PEC water oxidation performance.

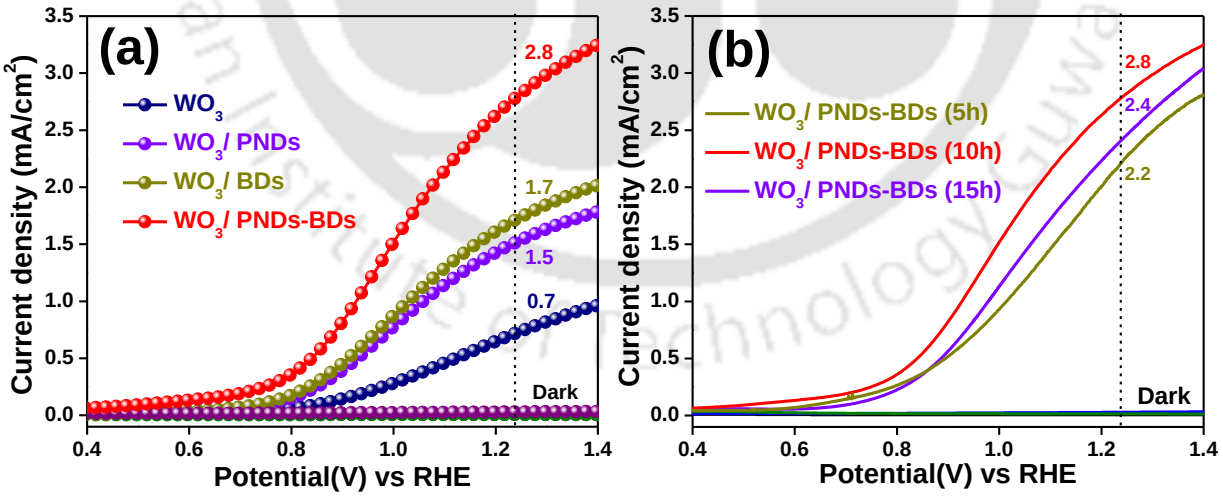

Figure 5.3.14 (a) LSV curves of WO_3, WO_3/PNDs, WO_3/BDs and WO_3/PNDs-BDs photoanodes; (b) LSV curves WO_3/PNDs-BDs photoanodes with respect to different dipping time for loading BDs over WO_3/PNDs. All these LSV measurements were operated in neutral medium electrolyte (0.1M Na_2SO_4) under 1 Sun illumination @ 1.23 V vs. RHE.

Part of this chapter has been published in **Chem. Commun. 2023, 59, 1955**.

To know the photo response behavior of WO_3 photoanode, chronoamperometry analysis of WO_3, WO_3/PNDs, WO_3/BDs and WO_3/PNDs-BDs photoanodes were carried out under 1 Sun light ON and OFF state at 1.23 V vs RHE (**figure 5.3.15(a)**). The anodic spikes of WO_3 photoanode were diminished significantly due to the incorporation of PNDs and BDs which indicates the minimization of photogenerated carrier recombination due to type II heterojunction approach. The chronoamperometry analysis of PNDs, BDs and PNDs-BDs thin-films were carried out to know the photo-response property (**figure 5.3.15(b)**). Although PNDs and BDs show a very less current densities in $\mu A/cm^2$ as compared to current density of WO_3 thin-film, still the light harvesting capability of photo responsive material PNDs and BDs is confirmed. As the photo-response property of PNDs-BDs hybrid is higher (~ 0.2 $\mu A/cm^2$) as compared to the individual photo-response property of PNDs (~ 0.1 $\mu A/cm^2$) and BDs (~ 0.1 $\mu A/cm^2$), that indicates the maximized charge separation and minimized charge recombination due to formation PNDs-BDs hybrid.

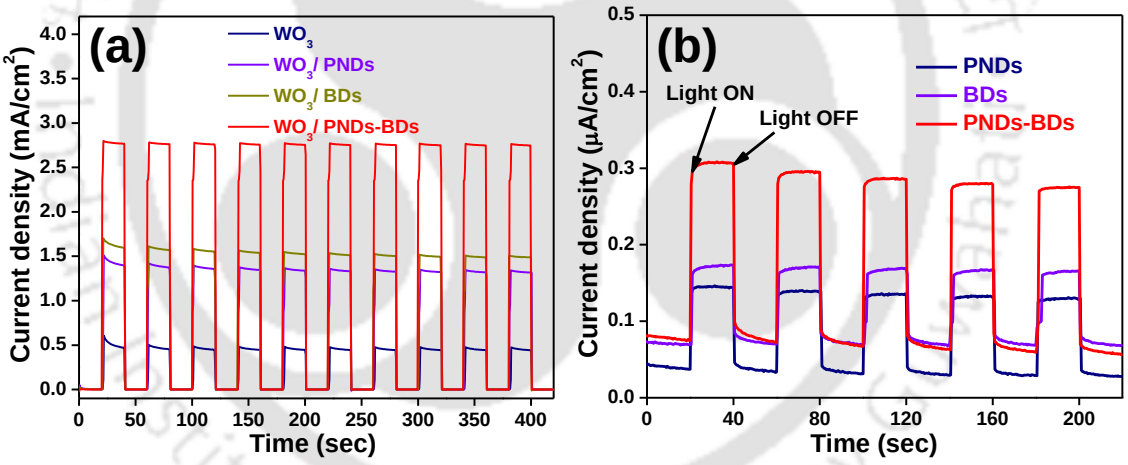

Figure 5.3.15 Chronoamperometry curves of (a) WO_3, WO_3/PNDs, WO_3/BDs and WO_3/PNDs-BDs photoanodes,(b) PNDs, BDs and PNDs-BDs hybrid under 1 Sun illumination in 0.1 M Na_2SO_4 electrolyte at 1.23 V vs RHE.

5.3.8 Electrochemical impedance spectroscopy (EIS) analysis

In order to know the carrier transport behavior across the interfaces of PNDs, BDs and PNDs-BDs, EIS measurements were analyzed under 1 Sun illumination at 1.23 V vs RHE. **Figure 5.3.16** shows the Nyquist plots for PNDs, BDs and PNDs-BDs films having experimental data and fitted data w.r.t. equivalent circuit model (inset in **figure 5.3.16**). The radius of semicircles related to PNDs and BDs films are smaller due to the formation of PNDs-BDs hybrid. The equivalent circuit parameters related to Nyquist plots for the photoanodes have been provided in **table 5.3.3**.

Part of this chapter has been published in **Chem. Commun. 2023, 59, 1955**.

The R_{ct} value for PNDs and BDs were reduced from 241 kΩ and 163 kΩ to 15 kΩ due to PNDs-BDs formation. These results confirm the improved charge transfer properties are due to the formation of type-II heterojunction based PNDs-BDs hybrid.

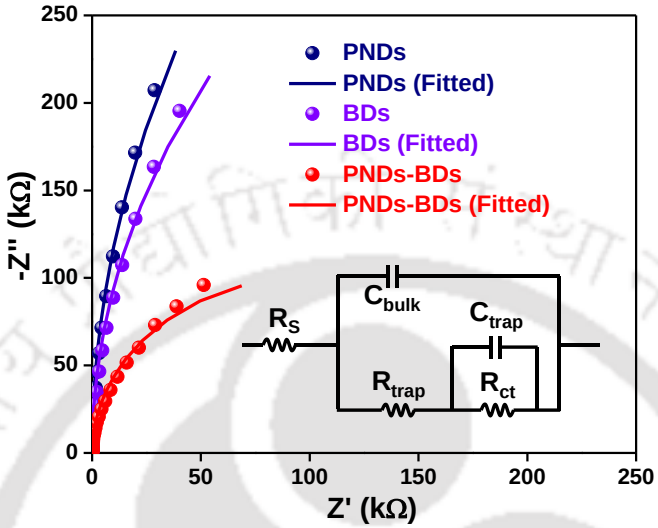

Figure 5.3.16 Nyquist plots of PNDs, BDs and PNDs-BDs electrodes having their fitted curves w.r.t. equivalent circuit model under 1 Sun illumination at 1.23 V vs RHE.

Table 5.3.3 Fitting parameters for Nyquist plots of PNDs, BDs and PNDs-BDs thin films.

Electrodes	R_s(Ω)	R_{trap}(kΩ)	R_{ct}(kΩ)
PNDs	33.9	1173	241
BDs	40.7	751	163
PNDs-BDs	34.8	187	15

In order to know the carrier transport behavior across the interfaces of WO_3 photoanode by modification with PNDs and BDs, EIS measurements for the photoanodes were analyzed under 1 Sun illumination at 1.23 V vs RHE. **Figure 5.3.17(a)** represents the Nyquist plots for the photoanodes having spherical symbols for experimental data and solid lines for fitted data w.r.t. equivalent circuit model (inserted in **figure 5.3.17(a)**). The semicircle related to WO_3 photoanode was getting reduced due to modifications with PNDs and BDs, which attributes to the improved charge transport property of WO_3 with PNDs and BDs. The equivalent circuit parameters related to Nyquist plots for the photoanodes are provided below in **table 5.3.4**. The R_{ct} value of WO_3 photoanode was reduced regularly with PNDs and BDs modifications such as 1906 Ω, 1374 Ω, 1293 Ω, and 978 Ω for WO_3, WO_3/PNDs, WO_3/BDs and WO_3/PNDs-BDs,

Part of this chapter has been published in **Chem. Commun. 2023, 59, 1955**.

respectively. These reduced R_{ct} numbers confirm that the loaded PNDs and BDs over WO_3 photoanode facilitate charge separation and transportation property of WO_3 photoanode. Similarly, the R_{trap} value of WO_3 photoanode was minimized with modifications, i.e., 80.9 Ω , 77.4 Ω , 75.7 Ω and 72.4 Ω for WO_3, WO_3/PNDs, WO_3/BDs and WO_3/PNDs-BDs, respectively. These results confirm the minimized trap sites and maximized charge transfer pathways of WO_3 photoanode due to modifications with PNDs and BDs.

The MS-analysis was carried out to know the change in total carrier density (N_D) of WO_3 photoanode with PNDs and BDs modifications, as shown in **figure 5.3.17(b)**. The positive slops confirm the n-type conductivity of the bare and modified photoanodes. The calculated charge carrier densities are 1.5×10^{20} cm^{-3} for WO_3 photoanode, 2.1×10^{20} cm^{-3} for WO_3/PNDs photoanode, 2.5×10^{20} cm^{-3} for WO_3/BDs photoanode and 4×10^{20} cm^{-3} for WO_3/PNDs-BDs

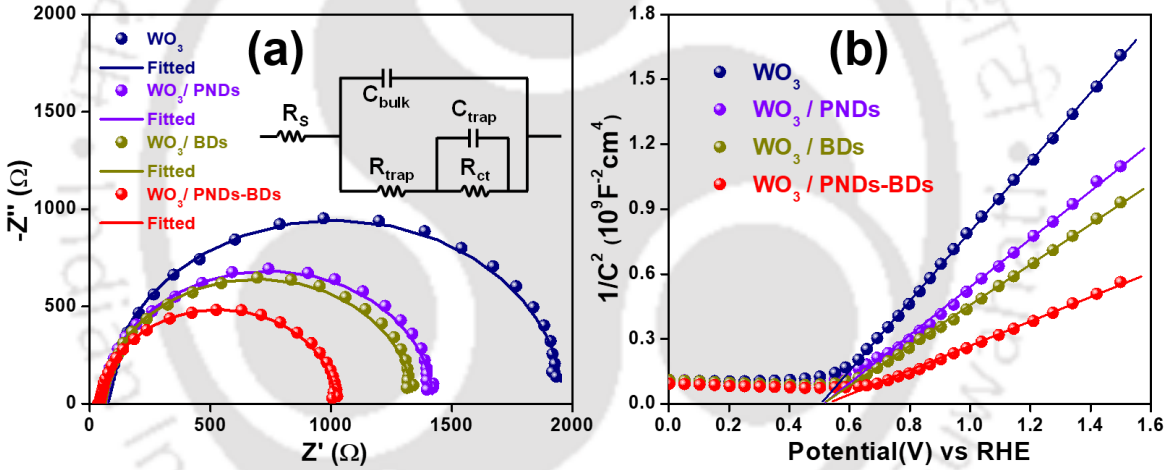

Figure 5.3.17 (a) Nyquist plots of WO_3, WO_3/PNDs, WO_3/BDs and WO_3/PNDs-BDs photoanodes having their fitted curves w.r.t. equivalent circuit model under 1 Sun illumination at 1.23 V vs RHE and (b) Mott−Schottky plots of WO_3, WO_3/PNDs, WO_3/BDs and WO_3/PNDs-BDs photoanodes.

Table 5.3.4 Fitting parameters for Nyquist plots and total charge carrier densities of WO_3, WO_3/PNDs, WO_3/BDs and WO_3/PNDs-BDs photoanodes.

Photoanode	R_s(Ω)	R_{trap}(Ω)	C_{bulk}(μF)	R_{ct}(Ω)	C_{trap}(μF)	N_D(cm^{-3})
WO_3	51.8	80.9	26.0	1906	24.9	**1.5×10^{20}**
WO_3/PNDs	46.6	77.4	27.9	1374	15.5	2.1×10^{20}
WO_3/BDs	43.4	75.7	30.6	1293	16.4	2.5×10^{20}
WO_3/ PNDs-BDs	38.4	72.4	31.6	978	18.1	**4.0×10^{20}**

Part of this chapter has been published in **Chem. Commun. 2023, 59, 1955**.

photoanode, respectively. The synergistic effects between positively charged PNDs and negatively charged BDs provide improved charge carrier densities to the WO_3 photoanode, which facilitate the electrical conductivity of the photoanode for higher oxidation activity.

5.3.9 Charge separation and injection efficiencies

To know the improvement in charge separation efficiency (η_{sep}) and charge injection efficiency (η_{inj}) by PNDs and BDs modifications on WO_3 photoanode, hole scavenger (HS) test of the photoanodes was performed under 1 Sun illumination in 0.1 M Na_2SO_4 electrolyte having 0.03 M Na_2SO_3 hole scavenger (**figure 5.3.18**).[7] The current densities from LSV data were recorded to be ~ 2.9, ~ 1.5, ~ 1.4 and ~ 1.1 times higher in presence of hole scavenger in comparison to corresponding photoanodes in absence of the hole scavenger for WO_3, WO_3/PNDs, WO_3/BDs and WO_3/PNDs-BDs photoanodes, respectively (**figure 5.3.18(a)** and **figure 5.3.18(b)**).

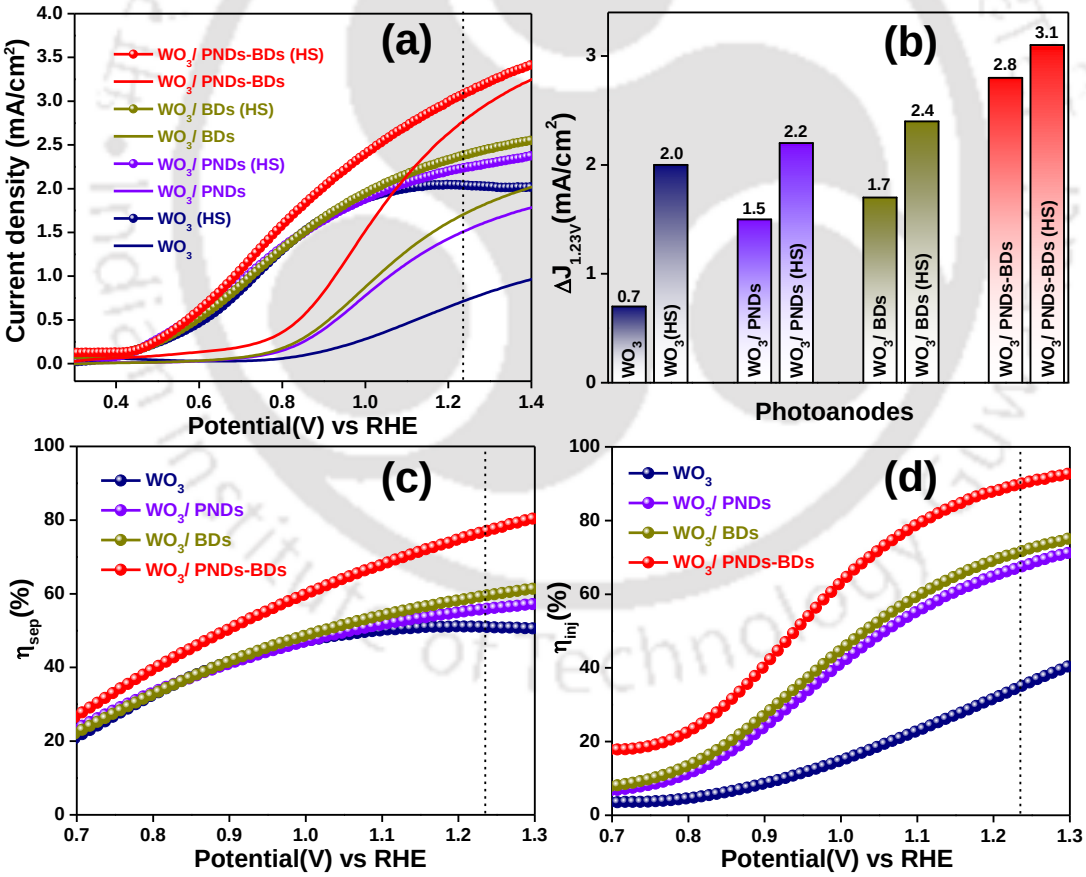

Figure 5.3.18 (a) LSV curves in presence of hole scavenger (Na_2SO_3) at 1.23 V vs RHE in Na_2SO_4 electrolyte; (b) Current density based bar diagram at 1.23 V vs RHE of the photoanodes with and without hole scavenger; charge (c) separation and (d) injection efficiencies of the photoanodes under 1 Sun illumination.

Part of this chapter has been published in **Chem. Commun. 2023, 59, 1955**.

A very high enhancement in current density for WO_3 photoanode in comparison to other modified photoanodes confirms the maximized electrical conductivity due to modification with PNDs and BDs over WO_3 film. The calculated η_{sep} of WO_3 was enhanced from 51 % to 56 % for WO_3/PNDs, 60 % for WO_3/BDs and 77 % for WO_3/PNDs-BDs photoanodes (**figure 5.3.18(c)**), which attributes the better and faster charge separation ability of WO_3 due to dual incorporations of PNDs and BDs. Similarly, an enhanced η_{inj} of WO_3 from 35 % to 67 % for WO_3/PNDs, 72 % for WO_3/BDs and maximum 91 % for WO_3/PNDs-BDs photoanodes (**figure 5.3.18(d)**), results a maximized charge transport property at photoanode/electrolyte interface and minimized photogenerated carriers recombination of WO_3 photoanode due to the dual nanodots modifications. The very low 35 % of η_{inj} with a high 51 % of η_{sep} indicates the sluggish PEC activity of WO_3 photoanode, whereas the significant improvement in η_{inj} up to 91 % with PNDs and BDs incorporations attributes the surface charge induced heterojunction approach for boosted PEC water oxidation performance.[19]

5.3.10 IPCE, stability and Faradaic efficiency measurements

IPCE for the photoanodes was analyzed to evaluate the change in current conversion efficiency of WO_3 photoanodes with dual incorporations of PNDs and BDs over the surface, as shown in **figure 5.3.19(a)**. The IPCE of WO_3 thin film was maximized from 16 % to 31 %, 36 % and a maximum 56 % with PNDs, BDs and PNDs-BDs modifications, respectively, which confirms the better photocatalytic property of WO_3/PNDs-BDs photoanode in comparison to other unmodified and single modified WO_3 photoanodes. The IPCE details evidence the improved PEC water oxidation performance of WO_3 photoanode offered by the synergistic effects between positively charged PNDs and negatively charged BDs. To examine the operational stability, the chronoamperometry analysis of the photoanodes was performed for 10 hours (**figure 5.3.19(b)**). After 10 h of analysis, the WO_3, WO_3/PNDs, WO_3/BDs and WO_3/PNDs-BDs photoanodes were stabilized up to a very less 20 %, average of 75 % and 80 % and a very high 90 %, respectively, w.r.t. initial corresponding photocurrent densities. The modifications with PNDs and BDs, provide a significantly enhanced photostability to WO_3 photoanode. The WO_3/PNDs-BDs photoanode generated oxygen and hydrogen gases were quantified by online gas chromatography, as shown in **figure 5.3.19(c)**. An average of ~ 86 % and ~ 88 % Faradaic yield for oxygen and hydrogen gas were quantified after 180 min of analysis.

Part of this chapter has been published in **Chem. Commun. 2023, 59, 1955**.

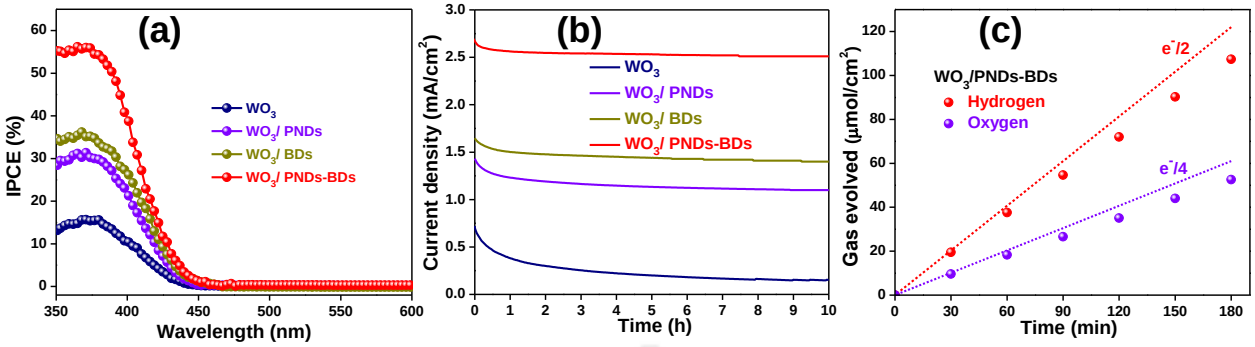

Figure 5.3.19 (a) IPCE plots of WO_3, WO_3/PNDs, WO_3/BDs and WO_3/PNDs-BDs photoanodes; (b) Photo-stabilities of WO_3, WO_3/PNDs, WO_3/BDs and WO_3/PNDs-BDs photoanodes under 1 Sun illumination at 1.23 V vs RHE; (c) Faradic yield of WO_3/PNDs-BDs photoanode for oxygen and hydrogen gas evolution.

5.3.11 Mechanism

From the XPS valence band spectra analysis, the valence band of WO_3 photoanode was calculated to be at 2.9 eV (**figure 5.3.20(a)**). The valence band and bandgap analysis, confirm the conduction band of WO_3 to be at 0.1 eV. From the Mott-Schottky analysis, the Fermi levels for WO_3, PNDs and BDs were found to be at 0.5 eV, 0.1 eV and -0.1 eV, respectively (**figure 5.3.17(b)** and **figure 5.3.20(b)**). Mechanistically, there is type-II heterojunction between bare WO_3 and the PNDs-BDs hybrid. The schematic of the composite photoanode, followed by type-II-II′ heterojunctions, proposing a detailed charge transfer mechanism within the components (a) along with the formations (b) has been shown in **figure 5.3.21**.

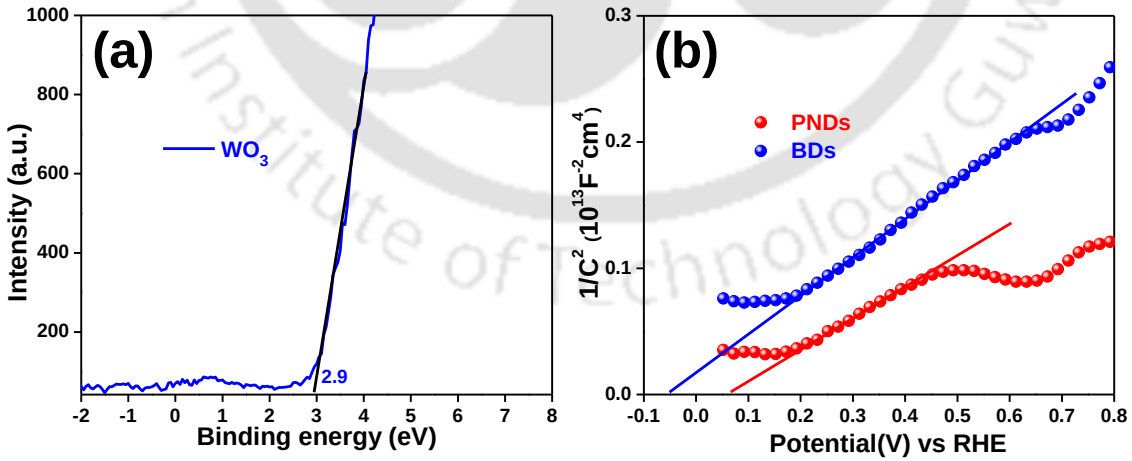

Figure 5.3.20 (a) XPS valence band spectra of WO_3; (b) Mott−Schottky plots of PNDs and BDs.

Part of this chapter has been published in **Chem. Commun. 2023, 59, 1955**.

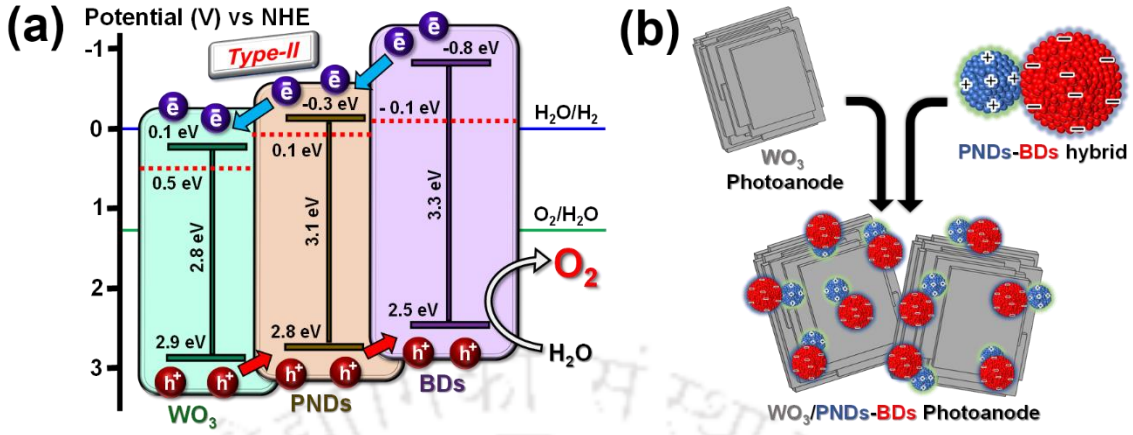

Figure 5.3.21 (a) Schematic of the type-II-II′ based WO_3/PNDs-BDs composite photoanode proposing the detailed charge transfer mechanism within the components; (b) schematic for the formation of the WO_3/PNDs-BDs hybrid.

5.4 CONCLUSIONS

Herein, a type II heterojunction model of phosphorous nitride and borophene has been designed, keeping the electrostatic interactions as the key component for the formation, which serves as a good support for WO_3 based photoelectrochemical process. Our fabricated WO_3/PNDs-BDs composite, having thin layers of PNDs and BDs over hydrothermally synthesized WO_3 film has offered a significant, 4-fold higher current density of 2.8 mA/cm^2 at 1.23 V vs RHE in comparison to the bare WO_3 photoanode. As evidenced from EIS and hole scavenger analysis, the maximized charge separation and transportation with minimized charge recombination are the major contributions by WO_3/PNDs-BDs composite for high PEC performance due to type-II-II′ heterojunctions approach. These major factors have triggered the induced carrier density as confirmed by MS-analysis. This approach might offer insight to design efficient photoelectrode for solar energy harvesting.

5.5 REFERENCES

1. F. Ronconi, Z. Syrgiannis, A. Bonasera, M. Prato, R. Argazzi, S. Caramori, V. Cristino and C. A. Bignozzi, *J. Am. Chem. Soc.*, 2015, **137**, 4630.
2. B. Jin, E. Jung, M. Ma, S. Kim, K. Zhang, J. I. Kim, Y. Son and J. H. Park, *J. Mater. Chem. A*, 2018, **6**, 2585–2592.
3. M. K. Mohanta, T. K. Sahu and M. Qureshi, *Chem. – Asian J.*, 2020, **15**, 3886–3896.

Part of this chapter has been published in **Chem. Commun. 2023, 59, 1955**.

4. L. Zheng, X. Ye, X. Deng, Y. Wang, Y. Zhao, X. Shi and H. Zheng, *ACS Sustainable Chem. Eng.*, 2020, **8**, 15906–15914.
5. K. Ye, Z. Wang, J. Gu, S. Xiao, Y. Yuan, Y. Zhu, Y. Zhang, W. Mai and S. Yang, *Energy Environ. Sci.*, 2017, **10**, 772–779.
6. T. Zhang, Z. Zhu, H. Chen, Y. Bai, S. Xiao, X. Zheng, Q. Xue and S. Yang, *Nanoscale*, 2015, **7**, 2933–2940.
7. M. K. Mohanta, T. K. Sahu, D. Gogoi, N. R. Peela and M. Qureshi, *ACS Appl. Energy Mater.*, 2019, **2**, 7457–7466.
8. H. Liu, Y. Du, Y. Deng and P. D. Ye, *Chem. Soc. Rev.*, 2015, **44**, 2732–2743.
9. W. Schnick, J. Lücke and F. Krumeich, *Chem. Mater.*, 1996, **8**, 281–286.
10. K. Landskron, H. Huppertz, J. Senker and W. Schnick, *Angew. Chem., Int. Ed.*, 2001, **40**, 2643.
11. T. K. Sahu, S. Alam, S. Bhowmick, M. K. Mohanta, M. Qureshi, *Chem. Commun.*, 2016, **8**, 563– 568.
12. B. Feng, J. Zhang, Q. Zhong, W. Li, S. Li, H. Li, P. Cheng, S. Meng, L. Chen and K. Wu, *Nat. Chem.*, 2016, **8**, 563–568.
13. G. Tai, T. Hu, Y. Zhou, X. Wang, J. Kong, T. Zeng, Y. You and Q. Wang, *Angew. Chem., Int. Ed.*, 2015, **54**, 15473–15477.
14. X. Zhang, J. Hu, Y. Cheng, H. Y. Yang, Y. Yao and S. A. Yang, *Nanoscale*, 2016, **8**, 15340–15347.
15. A. R. Oganov, J. Chen, C. Gatti, Y. Ma, Y. Ma, C. W. Glass, Z. Liu, T. Yu, O. O. Kurakevych and V. L. Solozhenko, *Nature*, 2009, **457**, 863.
16. H. Li, L. Jing, W. Liu, J. Lin, R. Tay, S. Tsang and E. Teo, *ACS Nano*, 2018, **12**, 1262–1272.
17. X. Wu, J. Shu, B. Feng, L. Yang, J. Lan, F. Li, P. Xi and F. Wang, *Chem. Commun.*, 2019, **55**, 4719–4722.
18. M. C. Zhang, Y. Li, C. Y. Bai, X. H. Guo, J. Han, S. Hu, H. Q. Jiang, W. Tan, S. J. Li and L. J. Ma, *ACS Appl. Mater. Interfaces*, 2018, **10**, 28936–28947.
19. M. K. Mohanta, T. K. Sahu, S. Bhowmick, M. Qureshi, *Electrochimica Acta*, 2022, **415**, 140269.

Part of this chapter has been published in **Chem. Commun. 2023, 59, 1955**.

CHAPTER 6

Synchronized carrier extraction and injection through boron nitride nanoplatelets in hierarchical $BiVO_4$/CoCr-layered double hydroxides for efficient water oxidation

This chapter offers the interfacial insertion of hole extractor between semiconductor photoanode and surface oxygen evolution catalyst (OECs) for amplified photoelectrochemical (PEC) water oxidation performance. Herein, modifications of bare monoclinic $BiVO_4$ photoanode with two-dimensional boron nitride nanoplatelets (BNNPs) as hole extractor and CoCr-layered double hydroxides (CoCr-LDH) as kinetics accelerator results to achieve speedy charge separation with suppressed charge recombination and accelerated PEC water oxidation kinetics. This work is promising as it fill-in the gap between the photoanode and OECs for boosting the PEC water oxidation efficiency of metal-oxide based photoanode.

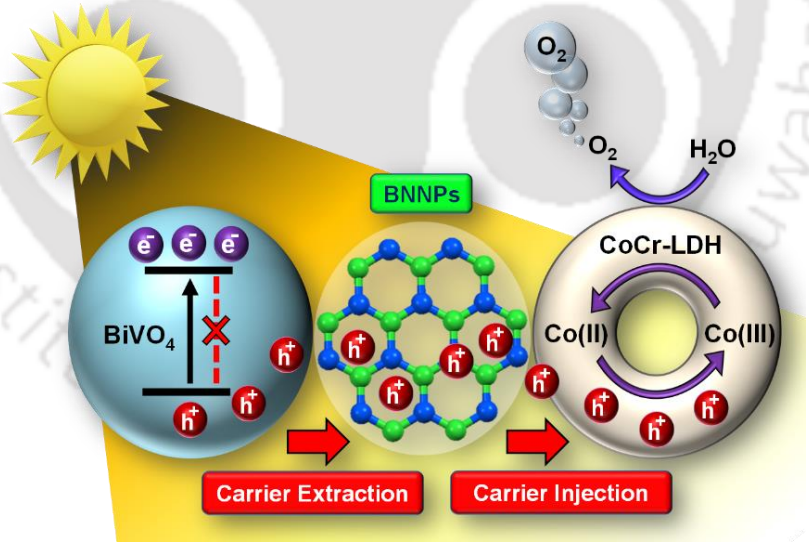

Electrochimica Acta

M. K. Mohanta *et al.,* 2022, **415,** 140269

6.1 INTRODUCTION

In recent years, polycrystalline bismuth vanadate ($BiVO_4$) photoanodes having a narrow band gap of 2.4-2.6 eV has fascinated strongly for superior light harvesting property and enhanced PEC water oxidation performance among the different n-type metal oxide semiconductors.[1,2] Nevertheless, photogenerated charge carriers recombination due to poor carrier mobility, lesser hole-diffusion length (< 70 nm), surface trap sites and poor water oxidation kinetics of $BiVO_4$ photoanode hampers the PEC performance strongly to reach theoretical solar-to-hydrogen (STH) conversion efficiency (i.e. 9.3 % with 7.5 mA cm^{-2}).[3,4] Several modifications such as structural and morphological tuning, elemental doping, variant heterojunctions, overlayer deposition and oxygen evolution co-catalysts (OECs) are operated to accelerate the water oxidation kinetics towards boosted PEC efficacy.[5-10] Separation of photogenerated electron-hole pair plays a vital role for boosted PEC water oxidation activities. Many researchers have aimed to ameliorate the kinetics of photoanodes for surface water oxidation by modification with OECs to offer more reaction channels along with reduced kinetic barriers and hole transfer efficacy.[11-18] Recently, van de Krol et al. re-stated that the performance of OECs is limited by the insufficient hole extraction from the photoanode to the OECs.[19] Zhong et al. reported the benefits of p-n junction interface for the extraction of photogenerated holes to minimize the electron-hole recombination by the deposition of p-NiO on the surface of CoO_x OECs/$BiVO_4$.[20] Zhang et al. suggested the hole extraction property of black phosphorene layer, incorporated over the $BiVO_4$ surface to accelerate the transportation of holes from $BiVO_4$ surface to co-catalyst.[2] Two-dimensional reduced graphene oxide (RGO), also known as carrier vehicle has been widely incorporated over semiconductors to accelerate the photogenerated charge separation.[21] Therefore, photogenerated hole extraction from the surface of semiconductors is crucial for enhanced PEC water oxidation activities. Notably, "White graphene" simply termed as boron nitride (BN), a structural analogue of graphene has established great attention because of its thermal and chemical stability, in-plane thermal conductivity and nominal toxicity.[22] Hexagonal boron nitride (h-BN) nanostructures has shown outstanding hole extraction capacity to maximize the photogenerated electron-hole separation.[23-25] Herein, we have focused to design composite photoanode having superior hole extraction property with accelerated surface oxidation kinetics. Firstly, we have incorporated a very thin layer of exfoliated two-dimensional boron nitride nanoplatelets (BNNPs) as an ultra-rapid hole extractor over the surface $BiVO_4$ photoanode. Secondly, an additional CoCr-LDH thin layer as an OEC has

Part of this chapter has been published in **Electrochimica Acta, 2022,415, 140269.**

been deposited hydrothermally to enhance the surface oxidation kinetics. Interfacial insertion of two dimensional BNNPs between $BiVO_4$ semiconductor and CoCr-LDH results to achieve a very high PEC water oxidation performance.

6.2 EXPERIMENTAL SECTION

6.2.1 Synthesis of $BiVO_4$ Photoanode

$BiVO_4$ photoanode was fabricated successfully over FTO conducting substrate in a step wise manner by using potassium iodide (KI), $Bi(NO_3)_3{\cdot}5H_2O$, HNO_3, p-benzoquinone, ethanol, Dimethyl sulfoxide (DMSO), vanadyl acetylacetonate ($VO(acac)_2$) and NaOH.[14] Firstly, the pH of a 50 mL aqueous solution containing 3.32 g of KI was adjusted to 1.7 pH by the addition of concentrated HNO_3 in a dropwise manner. 0.97 g of $Bi(NO_3)_3{\cdot}5H_2O$ was added to the above precursor solution with a continuous stirring up to 30 min and the Bi-contained precursor solution was named solution-A. Secondly, solution-B was prepared by addition of p-benzoquinone (0.497g) in 20 ml ethanol. In the next step, solution-A and B were combined together to get BiOI precursor solution and stirred for 30 min. The electrodeposition of BiOI over ozonized FTO, cleaned with distilled water, acetone and isopropanol was carried out by using a three-electrode system having FTO as working electrode, Ag/AgCl as reference electrode and Pt wire as counter electrode with an applied potential of -0.1 V vs Ag/AgCl for 200 seconds. The as-prepared BiOI films were washed properly with distilled water and dried overnight at 60°C inside a hot air oven. Those BiOI films were drop-casted with a DMSO solution having 0.2 M $VO(acac)_2$ and placed inside a muffle furnace at 450 °C for 2 h annealing with a maintained ramp rate of 2 °C/min. After annealing, those films were placed in 1 M NaOH solution to remove the residual amount of V_2O_5. Finally, the desired $BiVO_4$ was rinsed thoroughly with distilled water and placed inside the oven for 1h at 60 °C.

6.2.2 Synthesis of BNNPs

Hexagonal boron nitride nanoplatelets (h-BNNPs) were synthesized by two-step sonication method using the chemicals, i.e., bulk hexagonal boron nitride (h-BN) powder, ethanol, acetone and N,N-Dimethylformamide (N,N′-DMF).[26] In the first step, a 50 mL mixture solution of water, ethanol and acetone having ratio 45:3:2 containing 0.3 g of h-BN was ultrasonicated for 3 h to exfoliate the powder to platelet form. After that, the mixture solution was centrifuged for 10 min

Part of this chapter has been published in **Electrochimica Acta, 2022,415, 140269.**

at 1500 rpm. The desired surfactant containing BNNPs was collected and dried inside the furnace at 60 °C. In order to get thinner and smaller platelets, 0.1 g of as-prepared h-BNNPs was dispersed in 20 mL of DMF and ultrasonicated again for 3h in the second step. The h-BNNPs in DMF was centrifuged for 1 hr at 2000 rpm and finally, the white-colored surfactant of DMF containing BNNPs was collected.

6.2.3 Synthesis of $BiVO_4$/BNNPs photoanode

The incorporation of h-BNNPs over $BiVO_4$ photoanodes was carried out by following spin coating process. The BNNPs in DMF solution was spin coated over the as-prepared $BiVO_4$ photoanode for 1 min at 3000 rpm. In order to remove the DMF solvent from the surface of $BiVO_4$ photoanode incorporated with BNNPs were calcined for 1 h at 200 °C in an ambient atmosphere. For optimization of the $BiVO_4$/BNNPs photoanodes, the incorporations of BNNPs over bare $BiVO_4$ photoanode by spin coating process were repeated with different rpms such as 4000 rpm, 5000 rpm and 6000 rpm.

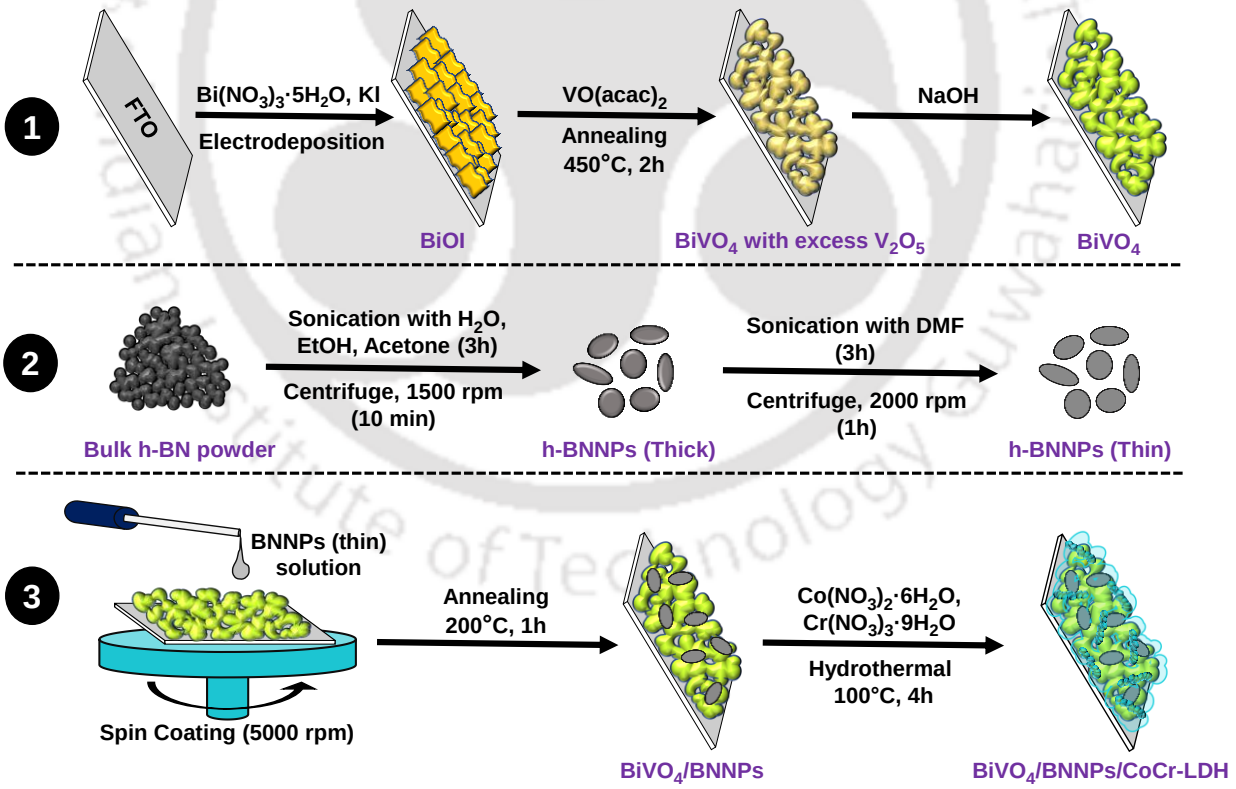

Scheme 6.2.1 Step wise synthesis operation of $BiVO_4$ photoanodes, BNNPs, $BiVO_4$/BNNPs photoanodes and $BiVO_4$/BNNPs/CoCr-LDH photoanodes, respectively.

Part of this chapter has been published in **Electrochimica Acta, 2022,415, 140269.**

6.2.4 Synthesis of $BiVO_4$/BNNPs/CoCr-LDH photoanode

Deposition of CoCr-LDH over $BiVO_4$/BNNPs photoanode was carried out hydrothermally by using $Co(NO_3)_2 \cdot 6H_2O$, $Cr(NO_3)_3 \cdot 9H_2O$, urea and ammonium fluoride (NH_4F).[27] 150 mg (0.75 mmol) of $Co(NO_3)_2 \cdot 6H_2O$, 70 mg (0.25 mmol) of $Cr(NO_3)_3 \cdot 9H_2O$, 105 mg of urea and 26 mg of NH_4F were dissolved in 35 mL of distilled water and stirred for 1 h. The precursor solution was placed in a 50 mL Teflon vessel having the as-synthesized $BiVO_4$/BNNPs photoanodes at the bottom with the composite surface facing downward. The vessel was placed inside the oven for 4 h at 100 °C. After completion of reaction, the synthesized $BiVO_4$/BNNPs/CoCr-LDH photoanode was rinsed properly with distilled water and placed inside the oven for 1 h drying at 60 °C. In order to optimize the loading of CoCr-LDH, different concentrations of $Co(NO_3)_2 \cdot 6H_2O$ (0.70 mmol and 0.80 mmol) and different concentrations of $Cr(NO_3)_3 \cdot 9H_2O$ (0.30 mmol and 0.20 mmol) were used by repeating the above procedure. A well explained graphical presentation for the complete fabrication and synthesis procedure for all $BiVO_4$ photoanodes, BNNPs, $BiVO_4$/BNNPs photoanodes and $BiVO_4$/BNNPs/CoCr-LDH photoanodes has been shown in **scheme 6.2.1**.

6.2.5 Synthesis of $BiVO_4$/Co-hydroxide and $BiVO_4$/Cr-hydroxide photoanodes

Deposition of Co-hydroxide and Cr-hydroxide over $BiVO_4$ photoanode was carried out hydrothermally by using $Co(NO_3)_2 \cdot 6H_2O$, $Cr(NO_3)_3 \cdot 9H_2O$, urea and NH_4F. 200 mg (1 mmol) of $Co(NO_3)_2 \cdot 6H_2O$, 105 mg of urea and 26 mg of NH_4F were dissolved in 35 mL of distilled water and stirred for 1 h. The precursor solution was placed in a 50 mL Teflon vessel having the as-synthesized $BiVO_4$ photoanodes at the bottom with the composite surface facing downward. The vessel was placed inside the oven for 4 h at 100 °C. After completion of the reaction, the synthesized $BiVO_4$/Co-hydroxide photoanodes were rinsed properly with distilled water and placed inside the oven for 1 h drying at 60 °C. Similarly, Cr-hydroxide was loaded over $BiVO_4$ film by replacing $Co(NO_3)_2 \cdot 6H_2O$ with 280 mg (1 mmol) of $Cr(NO_3)_3 \cdot 6H_2O$.

6.3 RESULTS AND DISCUSSION

6.3.1 Powder x-ray diffraction (XRD) analysis

Crystal phase analysis of bare $BiVO_4$, BNNPs, CoCr-LDH, and $BiVO_4$/BNNPs/CoCr-LDH photoanodes were carried out by XRD analysis as shown in **figure 6.3.1**. All the peaks of bare $BiVO_4$ photoanode are well matched with peaks of JCPDS no. 14-0688, which confirms the

Part of this chapter has been published in **Electrochimica Acta, 2022,415, 140269.**

monoclinic phase of $BiVO_4$. Hexagonal phase of BNNPs was confirmed by JCPDS no 34-0421.[28,29] The Bragg peaks of CoCr-LDH are well indexed to JCPDS no 33-0397.[30] All the peak positions for bare $BiVO_4$ and $BiVO_4$/BNNPs/CoCr-LDH are same, which indicates that no crystalline transformation of $BiVO_4$ photoanode is induced due to dual modification with BNNPs and CoCr-LDH. The XRD peaks of individual single modified $BiVO_4$/BNNPs and $BiVO_4$/CoCr-LDH composites confirm the unchanged crystalline transformation of $BiVO_4$ photoanode, as

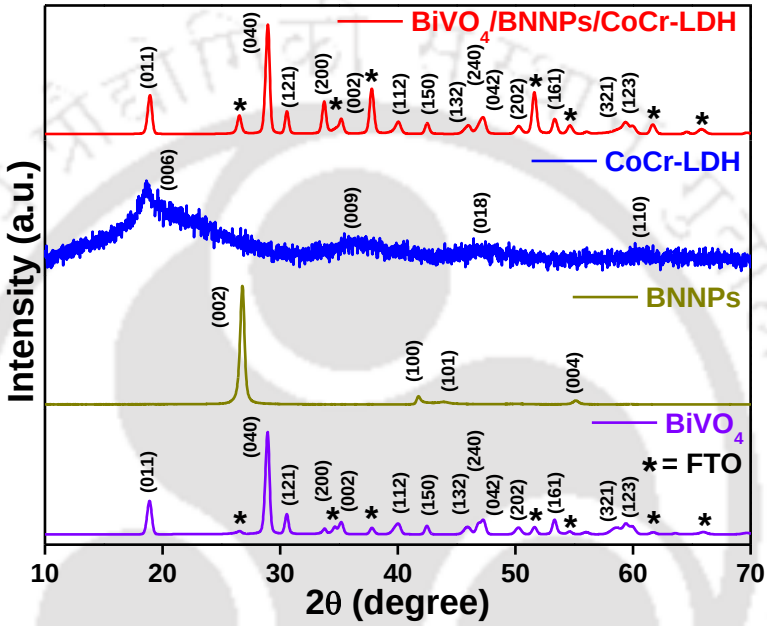

Figure 6.3.1 XRD analysis of thin film $BiVO_4$ photoanode, BNNPs powder, $BiVO_4$/BNNPs photoanode, CoCr-LDH powder, $BiVO_4$/CoCr-LDH and $BiVO_4$/BNNPs/CoCr-LDH photoanodes.

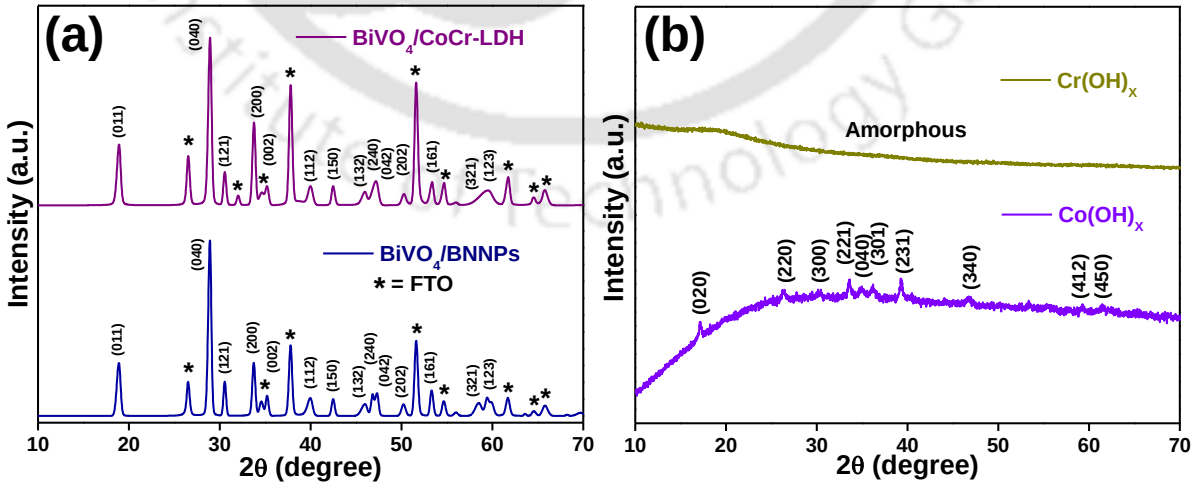

Figure 6.3.2 XRD analysis of (a) $BiVO_4$/BNNPs and $BiVO_4$/CoCr-LDH photoanodes; and (b) Co-hydroxide and Cr-hydroxide.

Part of this chapter has been published in **Electrochimica Acta, 2022,415, 140269.**

shown in **figure 6.3.2(a)**. The Co-hydroxide with $Co(OH)_x$ crystallinity was well indexed to JCPDS no 48-0083,[14] however the Cr-hydroxide was confirmed to be amorphous in nature (**figure 6.3.2(b)**).[18]

6.3.2 UV−visible absorption spectra analysis

In order to investigate the optical response with the proper band gap of bare and modified photoanodes, normalized UV-visible absorption spectra (**figure 6.3.3(a)**) and Tauc analysis (**figure 6.3.3(b)**) were analyzed. Absorption edges and bandgaps for all the photoanodes were recorded to be ~ 506 nm and 2.57 eV, respectively, which indicates that the modification with BNNPs and CoCr-LDH doesn't have any impact on the optical properties of bare $BiVO_4$ photoanode.

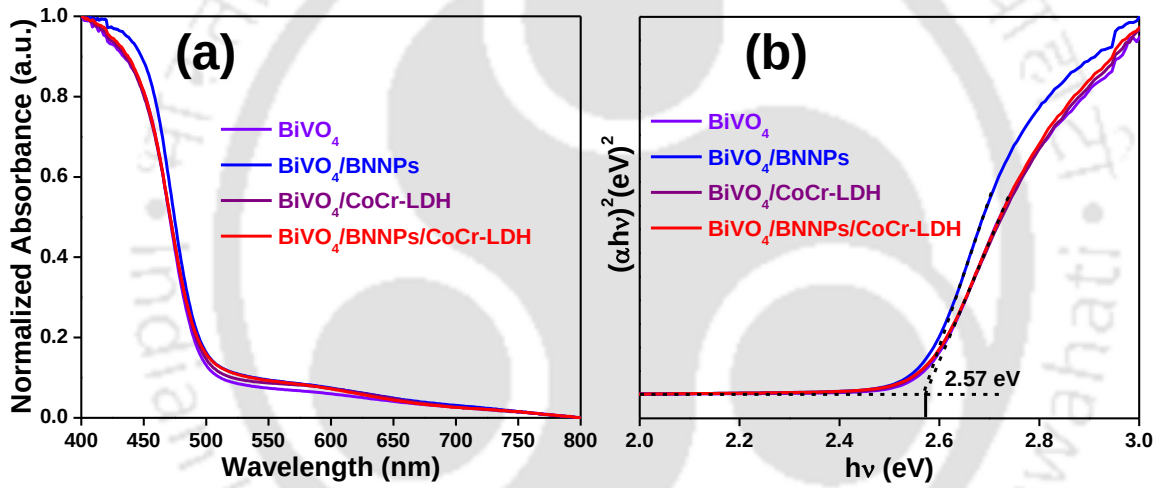

Figure 6.3.3 (a) UV-visible absorption spectra and the corresponding (b) Tauc's plots of $BiVO_4$, $BiVO_4$/BNNPs, $BiVO_4$/CoCr-LDH and $BiVO_4$/BNNPs/CoCr-LDH photoanodes.

6.3.3 Morphological analysis

The morphological features of BNNPs, CoCr-LDH, fabricated $BiVO_4$, $BiVO_4$/BNNPs, $BiVO_4$/CoCr-LDH and $BiVO_4$/BNNPs/CoCr-LDH were analyzed through FESEM technique (**Figure 6.3.4**). **Figure 6.3.4(a)** is the top view of fabricated $BiVO_4$ photoanode, which confirms the uniform growth of worm shaped $BiVO_4$ over the FTO. The cross-sectional view of $BiVO_4$ photoanode confirms the contact of $BiVO_4$ is much better to the FTO substrate making the ohmic contact better for charge collection (**figure 6.3.4(a)**). The nano-size platelet morphology of boron nitride (**figure 6.3.4(b)**) and the pollen grain like morphology of bare CoCr-LDH (**figure 6.3.4(c)**) was confirmed from FESEM analysis. **Figure 6.3.4(d)** represents the FESEM image of

Part of this chapter has been published in **Electrochimica Acta, 2022,415, 140269.**

$BiVO_4$/BNNPs photoanode, which confirms the uniform incorporation of BNNPs over the $BiVO_4$ photoanode. **Figure 6.3.4(e)** shows the top view of $BiVO_4$/CoCr-LDH photoanode which confirms that the pollen grain like CoCr-LDH was grown uniformly over the $BiVO_4$ photoanode by hydrothermal method. Similarly, **figure 6.3.4(f)** is the top view of dual modified $BiVO_4$/BNNPs/CoCr-LDH photoanode which confirms the hydrothermal incorporation of CoCr-LDH over $BiVO_4$/BNNPs photoanode. The voids of $BiVO_4$ film were reduced due to dual incorporations which also proves the incorporation of BNNPs and CoCr-LDH over the semiconductor surface.

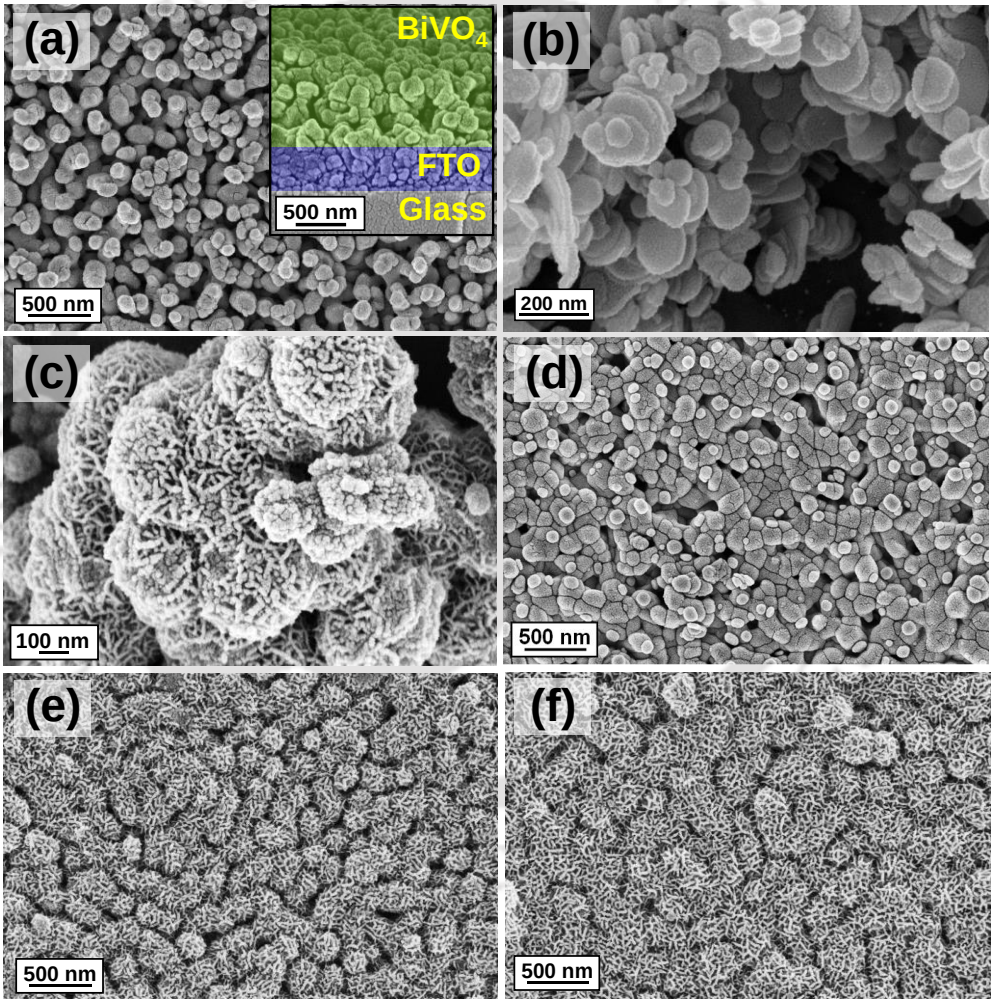

Figure 6.3.4 FESEM images of (a) $BiVO_4$ photoanode along with the Cross-sectional view, (b) BNNPs, (c) CoCr-LDH, (d) $BiVO_4$/BNNPs photoanode, (e) $BiVO_4$/CoCr-LDH photoanode and (f) $BiVO_4$/BNNPs/CoCr-LDH photoanode, respectively.

Part of this chapter has been published in **Electrochimica Acta, 2022,415, 140269.**

In order to evidence the structural and crystalline behavior of the composite photoanode, FETEM analysis was carried out (**figure 6.3.5**). **Figure 6.3.5(a)** is the FETEM image of BNNPs, which confirms the two-dimensional platelet structure of boron nitride with an average diameter of 150 nm. **Figure 6.3.5(b)** shows the FETEM image of CoCr-LDH. FETEM image of the composite $BiVO_4$/BNNPs/CoCr-LDH photoanode (**figure 6.3.5(c)**), proves the presence of $BiVO_4$ with incorporated hole extractor BNNPs and OECs i.e., CoCr-LDH. High-resolution transmission electron microscopy (HRTEM) analysis provides three different interplanar lattice spacings of 0.48 nm, 0.32 nm and 0.26 nm corresponding to (011) plane,[14] (002) plane[26] and (009) plane[18] of $BiVO_4$, BNNPs and CoCr-LDH, respectively (**figure 6.3.5(d)**). Scanning transmission electron microscopy (STEM) analysis with elemental mappings of $BiVO_4$/BNNPs/CoCr-LDH photoanode confirms the presence of homogeneous distribution of elements (**figure 6.3.6(I)-(VIII)**).

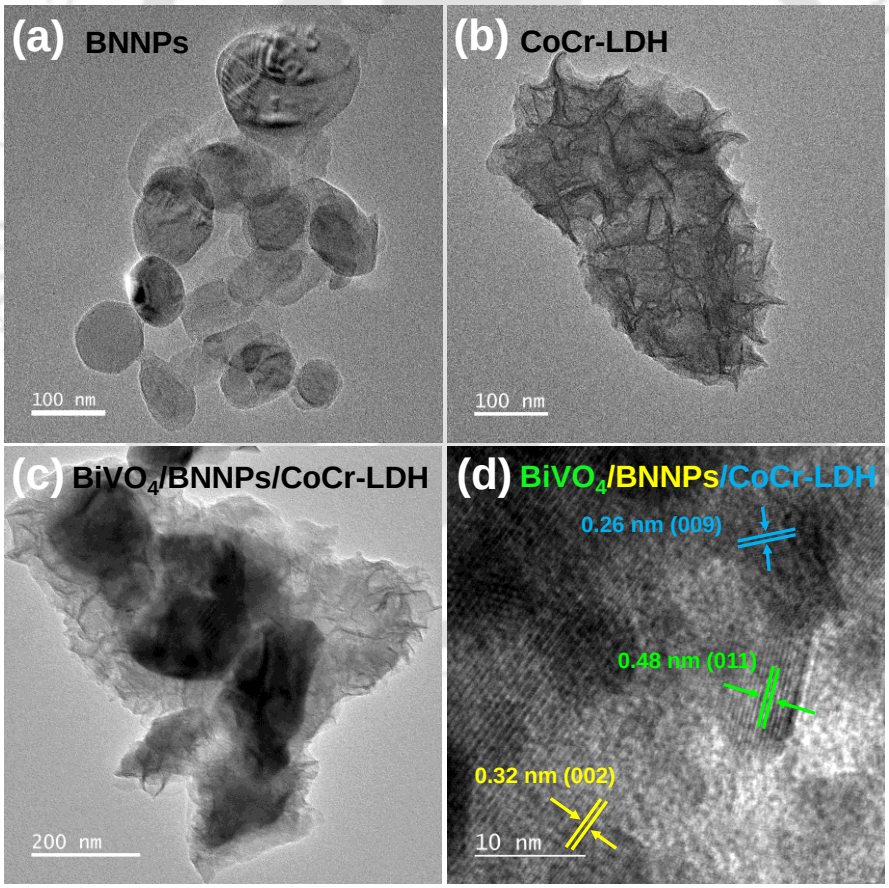

Figure 6.3.5 FETEM images of (a) BNNPs and (b) CoCr-LDH, (c) $BiVO_4$/BNNPs/CoCr-LDH composite photoanode; and (d) HRTEM image $BiVO_4$/BNNPs/CoCr-LDH composite.

Part of this chapter has been published in **Electrochimica Acta, 2022,415, 140269.**

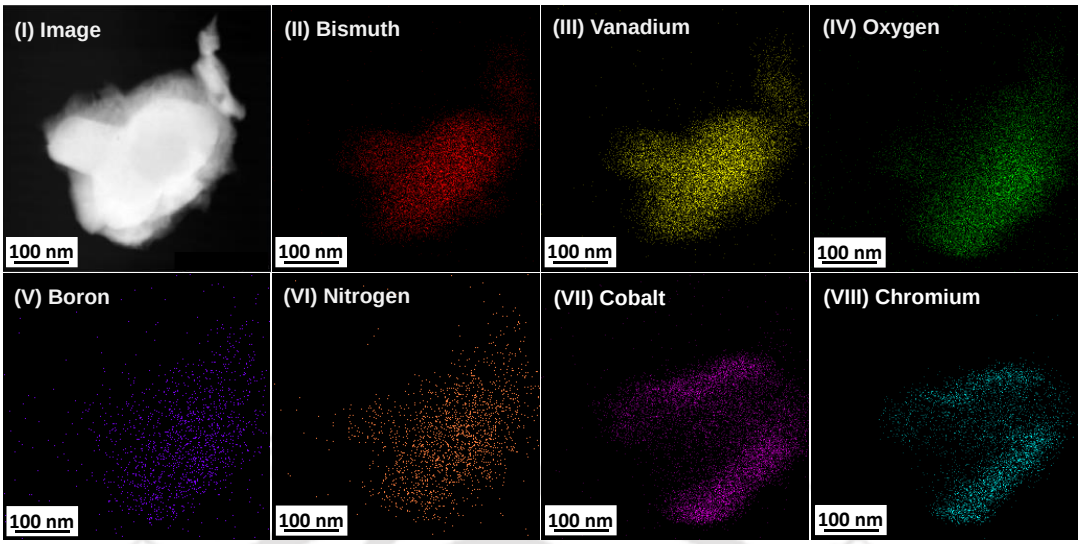

Figure 6.3.6 (I) STEM image and corresponding individual EDS mapping figures of $BiVO_4$/BNNPs/CoCr-LDH having (II) Bi, (III) V, (IV) O, (V) B , (VI) N, (VII) Co, and (VIII) Cr.

6.3.4 X-ray photoelectron spectroscopy (XPS) analysis

The electronic structure and chemical state analysis of all the bare and modified composite photoanodes were carried out through high-resolution XPS spectra, as shown in **figure 6.3.7**. All the well-defined characteristic peaks of Bi, V, O, B, N, Co and Cr from the survey spectra confirm the presence of $BiVO_4$, BNNPs and CoCr-LDH (**figure 6.3.7(a)**). The XPS binding energies for the analysis are corrected with respect to the binding energy of C 1s at 284.7 eV. Bismuth having +3 oxidation state in $BiVO_4$ photoanode was confirmed by the well assigned peaks of $4f_{7/2}$ and $4f_{5/2}$ at 159.1 and 164.4 eV, respectively (**figure 6.3.7(b)**).[14] The well ascribed peaks of $2p_{3/2}$ at 516.6 eV and $2p_{1/2}$ at 524.1 eV, indicates the presence vanadium having +5 oxidation state in $BiVO_4$ photoanode (**figure 6.3.7(c)**).[14] The XPS spectra for O 1s of $BiVO_4$ photoanode (**figure 6.3.7(d)**) has been fitted into two different signals at 529.8 and 531.7 eV assigned to lattice oxygen (O_L) signal and a mixed signal of oxygen vacancy (O_V) and hydroxylated surface (OH), i.e., O_V+ OH.[14] An insignificant change in peak positions of Bi (both $4f_{7/2}$ and $4f_{5/2}$), V (both $2p_{3/2}$ and $2p_{1/2}$) and O (only O_L) were noted due to incorporation of BNNPs, which confirms that the electronic environments of Bi, V and O_L are not significantly modified with BNNPs. The O_V+OH peak has been shifted towards lower binding energy, i.e., from 531.7 to 531.4 eV, which attributes the change in the nature of oxygen vacancy and surface modification. **Figure 6.3.7(e)** represents the XPS spectra of B 1s core-level spectra of BNNPs having two Gaussian peaks at 190.3 and 191 eV well agreeing to B-N and B-O bonds, respectively.[26] The XPS spectra for N 1s of BNNPs (**figure**

Part of this chapter has been published in **Electrochimica Acta, 2022,415, 140269.**

6.3.7(f)) has been fitted into two different signals at 397.9 and 398.5 eV corresponds to B-N bond and O-N bond, respectively.[26] The electronic interaction between $BiVO_4$ and BNNPs is confirmed due to shift in peak positions of B 1s (190.5 eV for B-N interaction and 191.2 eV for B-O interaction) and N 1s (398.3 eV for B-N interaction and 399.6 eV for O-N interaction) towards higher binding energy. The signals at 531.30 eV and 531.78 eV corresponds to surface-adsorbed hydroxyl species (M-OH) and M-O bond interactions of O 1s for CoCr-LDH (**figure 6.3.7(g)**).[18] A significant shift in signal positions of Bi (159.13 eV for $4f_{7/2}$ and 164.44 for $f_{5/2}$), V (516.7 eV for $2p_{3/2}$ and 524.4 eV for $2p_{1/2}$), O 1s (531.8 eV for O_L and 531.9 eV for O_V + OH), B1s

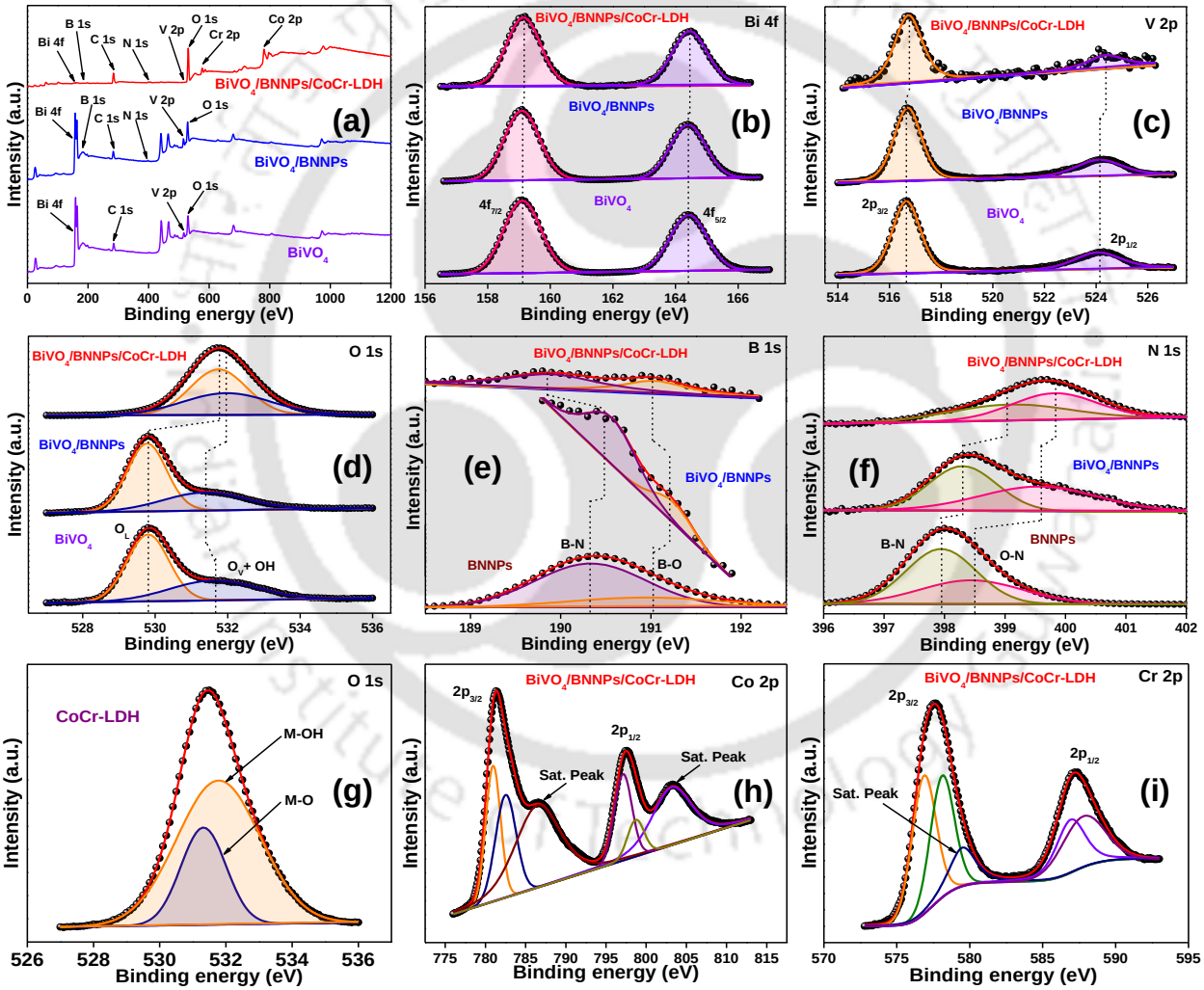

Figure 6.3.7 (a) XPS survey spectra of fabricated $BiVO_4$, $BiVO_4$/BNNPs and $BiVO_4$/BNNPs/CoCr-LDH photoanodes; High resolution XPS spectra of BNNPs, CoCr-LDH, fabricated $BiVO_4$, $BiVO_4$/BNNPs and $BiVO_4$/BNNPs/CoCr-LDH photoanodes: (b) Bi 4f , (c) V 2p, (d) O 1s (e) B 1s, (f) N 1s, (g) O 1s, (h) Co 2p and (i) Cr 2p.

Part of this chapter has been published in **Electrochimica Acta, 2022,415, 140269.**

(189.9 eV for B-N bond and 191 eV for B-O bond) and N 1s (398.9 eV for B-N bond and 399.8 eV for O-N bond) were noted after incorporation of CoCr-LDH over $BiVO_4$/BNNPs photoanode, which indicates a change in electronic environment of Bi, V, O, B and N. The high-resolution XPS spectra of Co 2p (**figure 6.3.7(h)**) has been fitted with four broad peaks corresponds to $2p_{3/2}$ at 781.3 eV, $2p_{1/2}$ at 797.5 eV and satellite peaks at 786.53 eV and 803.3 eV. Two wide peaks at 577.6 eV ($2p_{3/2}$), 587.3 eV ($2p_{1/2}$) and a satellite peak at 579.5 eV (**figure 6.3.7(i)**) were fitted for Cr 2p spectra. Further these two $2p_{3/2}$ and $2p_{1/2}$ peaks related to cobalt and chromium have fitted with four peaks related to spin-orbital splitting values.[27]

6.3.5 Photoelectrochemical characterizations

Linear sweep voltammetry (LSV) measurements of photoanodes were analyzed in 0.1 M Na_2SO_4 (pH=6) electrolyte under 1 Sun illumination to know the influence of BNNPs and CoCr-LDH incorporation over the surface of $BiVO_4$ photoanode (**figure 6.3.8(a)**). The bare $BiVO_4$ photoanode results in 1.2 mA/cm^2 current density at 1.23 V vs RHE with an onset potential of 0.42 V vs RHE. $BiVO_4$ photoanode with incorporation of BNNPs provides a maximum 2.8 mA/cm^2 current density at 1.23 V vs RHE with an onset potential of 0.42 V vs RHE. Optimization of BNNPs loaded onto the $BiVO_4$ has been studied and are shown in **figure 6.3.8(b)**. An increment of photocurrent density of ~ 2.3 times due to the incorporation BNNPs over $BiVO_4$ photoanode is accredited to enhancement in charge separation. Hole extraction ability of h-BN could be attributed to the availability of surface charges to maximize the photogenerated electron-hole separation has been reported in recent literatures.[25] Zeta potential is a suitable tool to assess the surface charge of BNNPs. Zeta potential analysis of BNNPs was carried out, as shown in **figure 6.3.8(c)**. A negative potential of - 29.5 mV with 4.23 mV zeta deviation was found in BNNPs. Thus incorporation of negatively charged species (BNNPs) influences the carrier separation by extracting the holes, thereby minimizing the recombination of charge carriers, resulting in enhanced photocurrent density. To further improve the interfacial charge resistance CoCr-LDH has been introduced. A maximum photocurrent density of 2.9 mA/cm^2 with 0.06 V vs RHE onset potential was found due to further modifications of $BiVO_4$ photoanode with CoCr-LDH. Incorporation of CoCr-LDH over $BiVO_4$ photoanode provides ~ 2.4 times higher current density. CoCr-LDH may enrich the kinetics of bare $BiVO_4$ photoanode for surface water oxidation to offer more reaction channels. Co-hydroxide and Cr-hydroxide were investigated in comparison to CoCr LDH to confirm the role of individual components Co and Cr in CoCr LDH for better oxidation kinetics.

Part of this chapter has been published in **Electrochimica Acta, 2022,415, 140269.**

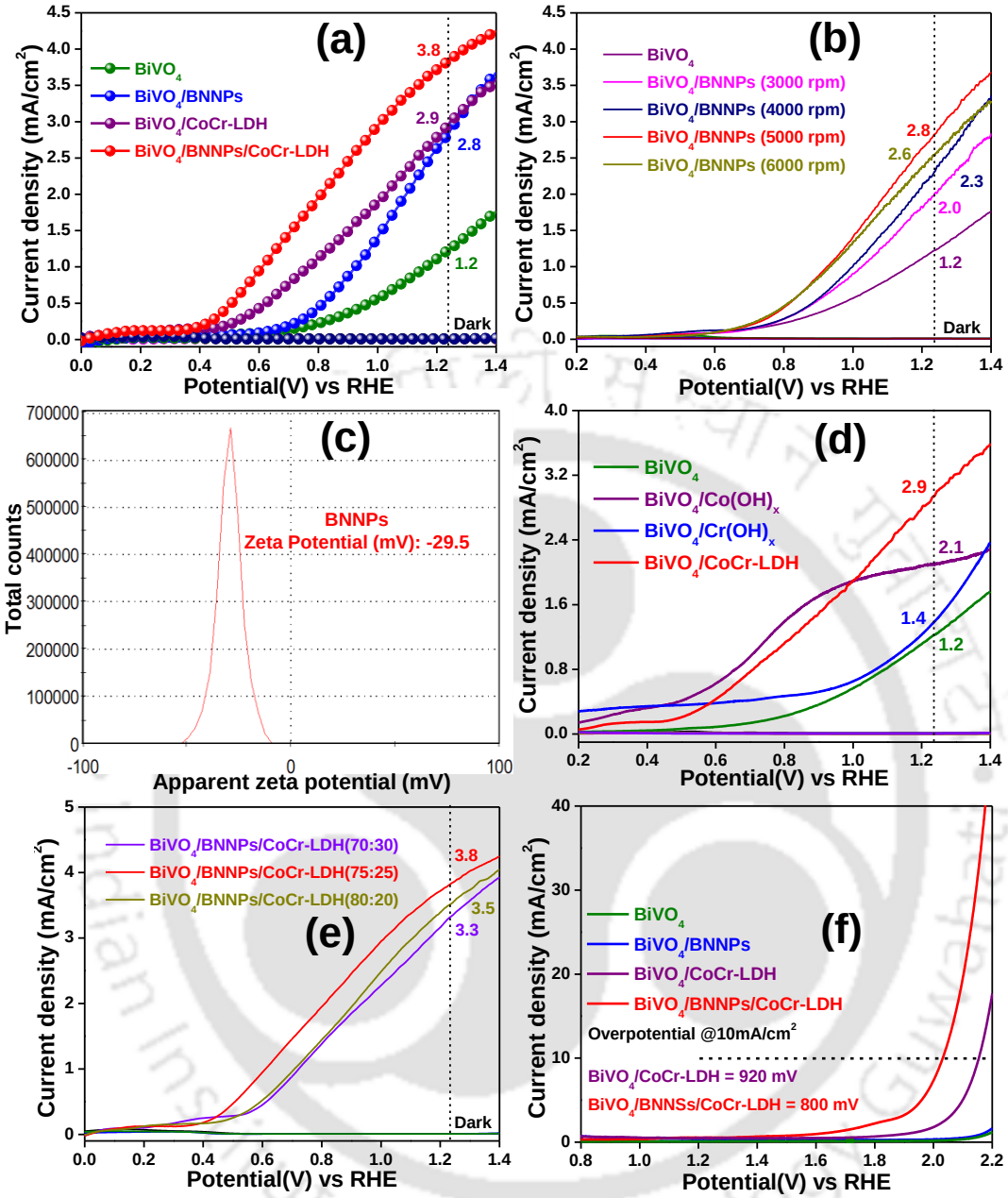

Figure 6.3.8 (a) LSV curves of $BiVO_4$, $BiVO_4$/BNNPs, $BiVO_4$/CoCr-LDH and $BiVO_4$/BNNPs/CoCr-LDH photoanodes, (b) LSV curves of $BiVO_4$ and $BiVO_4$/BNNPs photoanodes with respect to different rpms (3000 rpm, 4000 rpm, 5000 rpm and 6000 rpm) used in spin coater; (c) Zeta potential plot for BNNPs; (d) LSV curves of bare $BiVO_4$, $BiVO_4$/Co-hydroxide, $BiVO_4$/Cr-hydroxide and $BiVO_4$/CoCr-LDH photoanodes; (e) LSV curves $BiVO_4$/BNNPs/CoCr-LDH photoanodes with respect to different concentrations of $Co(NO_3)_2 \cdot 6H_2O$ (0.70 mmol, 0.75 mmol and 0.80 mmol) and different concentrations of $Cr(NO_3)_3 \cdot 9H_2O$ (0.30 mmol, 0.25 mmol and 0.20 mmol); (f) LSV measurements of $BiVO_4$, $BiVO_4$/BNNPs, $BiVO_4$/CoCr-LDH and $BiVO_4$/BNNPs/CoCr-LDH photoanodes under dark conditions. All LSV measurements were operated in neutral medium electrolyte (0.1M Na_2SO_4) under 1 Sun illumination (except figure f analysis) @ 1.23 V vs. RHE.

Part of this chapter has been published in **Electrochimica Acta, 2022,415, 140269.**

A maximum current density of 1.4 mA/cm^2 and 2.1 mA/cm^2 were noted for $BiVO_4$ photoanode due to modifications with Co-hydroxide and Cr-hydroxide, respectively (**figure 6.3.8(d)**). These LSV curves confirm the absence of active catalytic sites in Cr-hydroxide for promoting PEC performance. In order to get a better PEC water oxidation performance, dual modification of bare photoanode was carried out by deposition of both BNNPs and CoCr-LDH over $BiVO_4$ thin film. The current density optimization of $BiVO_4$/BNNPs/CoCr-LDH photoanodes with respect to different concentrations of $Co(NO_3)_2 \cdot 6H_2O$ (0.70 mmol, 0.75 mmol and 0.80 mmol) and different concentrations of $Cr(NO_3)_3 \cdot 9H_2O$ (0.30 mmol, 0.25 mmol and 0.20 mmol), are shown in **figure 6.3.8(e)**. A maximum current density of 3.8 mA/cm^2 having 0.06 V vs RHE onset potential was achieved for the optimized $BiVO_4$/BNNPs/CoCr-LDH photoanode. After dual modification of $BiVO_4$ thin film with BNNPs and CoCr-LDH, ~ 3.2 times enhancement in current density and ~ 360 mV shift in onset potential illustrates an improvement in photogenerated electron-hole separation and PEC water oxidation kinetics. To further understand the role of CoCr-LDH in $BiVO_4$/BNNPs/CoCr-LDH photoanode for PEC water oxidation, LSV measurements of all the photoanodes were carried out in dark conditions (**figure 6.3.8(f)**). The CoCr-LDH based photoanodes, i.e., $BiVO_4$/CoCr-LDH (920 mV overpotential @ 10 mA/cm^2) and $BiVO_4$/BNNPs/CoCr-LDH (800 mV overpotential @ 10 mA/cm^2) have a very high catalytic activity compared to bare $BiVO_4$ and $BiVO_4$/BNNPs photoanodes, which approves the enhanced OER kinetics of modified photoanode due to the electrocatalytic activity of CoCr-LDH .

In order to evaluate the improvement in photoelectric conversion efficacy due to dual modifications of $BiVO_4$ photoanode, IPCE analysis (**figure 6.3.9(a)**) of all the photoanodes was carried out. The IPCE value of bare $BiVO_4$ (26%) was enhanced by ~ 3 times due to dual modification with BNNPs hole extractor and CoCr-LDH (69%). Also, IPCE data demonstrates the more photocatalytic behavior of $BiVO_4$/BNNPs/CoCr-LDH photoanode in comparison to modified $BiVO_4$/BNNPs (47%) and $BiVO_4$/CoCr-LDH (51%). The Improved IPCE percentage of $BiVO_4$/BNNPs/CoCr-LDH photoanode was also confirmed by the corresponding enhanced current density from LSV data. The above IPCE results confirm the effective improvement in PEC water oxidation activities due to the action of the BNNPs hole extractor and CoCr-LDH kinetic accelerator. Chronoamperometry analysis of pristine $BiVO_4$, $BiVO_4$/BNNPs, $BiVO_4$/CoCr-LDH and $BiVO_4$/BNNPs/CoCr-LDH photoanodes was analyzed at 1.23 V vs RHE under light ON-OFF state, as shown in **figure 6.3.9(b)**. Anodic spikes of bare $BiVO_4$, modified $BiVO_4$ photoanodes

Part of this chapter has been published in **Electrochimica Acta, 2022,415, 140269.**

(i.e., $BiVO_4$/BNNPs, $BiVO_4$/CoCr-LDH photoanode) were reduced significantly with dual modifications of $BiVO_4$ (i.e., $BiVO_4$/BNNPs/CoCr-LDH) which confirms the minimization of electron-hole recombination due to BNNPs hole extracting ability and maximized charge injection due to CoCr-LDH decoration over $BiVO_4$ film.

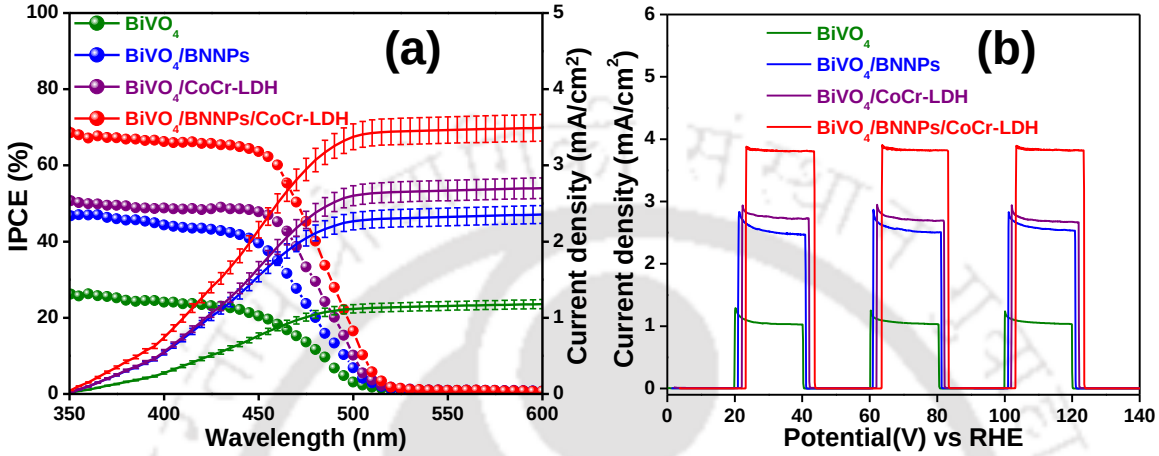

Figure 6.3.9 (a) Incident photon-to-current conversion efficiency (IPCE) w.r.t. obtained current densities; (b) Chronoamperometric curves of $BiVO_4$, $BiVO_4$/BNNPs, $BiVO_4$/CoCr-LDH and $BiVO_4$/BNNPs/CoCr-LDH photoanodes. The chronoamperometry measurements were operated in the neutral medium electrolyte (0.1M Na_2SO_4) under 1 Sun illumination (ON-OFF) @ 1.23 V vs. RHE.

6.3.6 Electrochemical impedance spectroscopy (EIS) analysis

In order to study the carrier transport behavior of $BiVO_4$ photoanode due to dual modification of BNNPs and CoCr-LDH, EIS measurements were carried out at 1.23 V vs RHE under 1 Sun illumination, as shown in **figure 6.3.10(a)**. The Nyquist plot for all photoanodes comprises the experimental data and fitted data w.r.t. equivalent circuit model (inset of **figure 6.3.10(a)**). The semicircles corresponding to $BiVO_4$/BNNPs/CoCr-LDH photoanode are smaller than the pristine $BiVO_4$ and $BiVO_4$/BNNPs, $BiVO_4$/CoCr-LDH photoanodes, which indicates the accelerated charge transfer behavior due to dual incorporation of BNNPs and CoCr-LDH. All the Nyquist plot fitted parameter values w.r.t. equivalent circuit model are given below in **table 6.3.1**. The recorded R_{ct} value for $BiVO_4$/BNNPs/CoCr-LDH photoanode was found to be 147 Ω, which is lesser than the R_{ct} values of other photoanodes, i.e., $BiVO_4$ (280 Ω), $BiVO_4$/BNNPs (189.4 Ω) and $BiVO_4$/CoCr-LDH (156.1 Ω) photoanodes, which illustrates the facilitated charge separation and transfer behavior of the loaded BNNPs and CoCr-LDH over $BiVO_4$ surface. The R_{trap} values for $BiVO_4$, $BiVO_4$/BNNPs, $BiVO_4$/CoCr-LDH and $BiVO_4$/BNNPs/CoCr-LDH photoanodes were

Part of this chapter has been published in **Electrochimica Acta, 2022,415, 140269.**

noted to be 105.3 Ω, 68.4 Ω, 45.9 Ω, 27.3 Ω, respectively. With dual modifications of $BiVO_4$ photoanode, a smaller R_{trap} (27.3 Ω) number in comparison to other photoanodes confirms the decrement in trap sites of bare and other modified $BiVO_4$ photoanodes. The C_{trap} values (capacitance at electrode/electrolyte interface) for $BiVO_4$, $BiVO_4$/BNNPs, $BiVO_4$/CoCr-LDH and $BiVO_4$/BNNPs/CoCr-LDH are enhanced significantly, which can be correlated to the surface layer modifications of $BiVO_4$ photoanode.[2] The overall resistance and capacitance parameters from the table represent the superior hole extraction property of BNNPs and accelerated PEC water oxidation kinetics of CoCr-LDH. The effect on charge carrier density (N_D) on dual modified $BiVO_4$ photoanode was analyzed through MS-analysis (**figure 6.3.10(b)**). The n-type conductivity behavior of all the photoanodes was confirmed with positive MS-slopes, whereas the slope of $BiVO_4$/BNNPs/CoCr-LDH photoanode is smaller in comparison to other modified photoanodes. The calculated carrier density value was found to be 10.1×10^{18} cm^{-3} which is 2.4, 1.7 and 1.4 times higher than the carrier density value of bare $BiVO_4$ (4.2×10^{18} cm^{-3}), $BiVO_4$/BNNPs (6.1×10^{18} cm^{-3}) and $BiVO_4$/CoCr-LDH (7.1×10^{18} cm^{-3}), respectively. The hole extraction from the valence band by BNNPs and the accelerated charge injection by CoCr-LDH are the major contributing factors toward boosted carrier density. The boosted carrier density with dual modifications are attributed to the facilitated electrical conductivity towards enhanced PEC water oxidation performance.

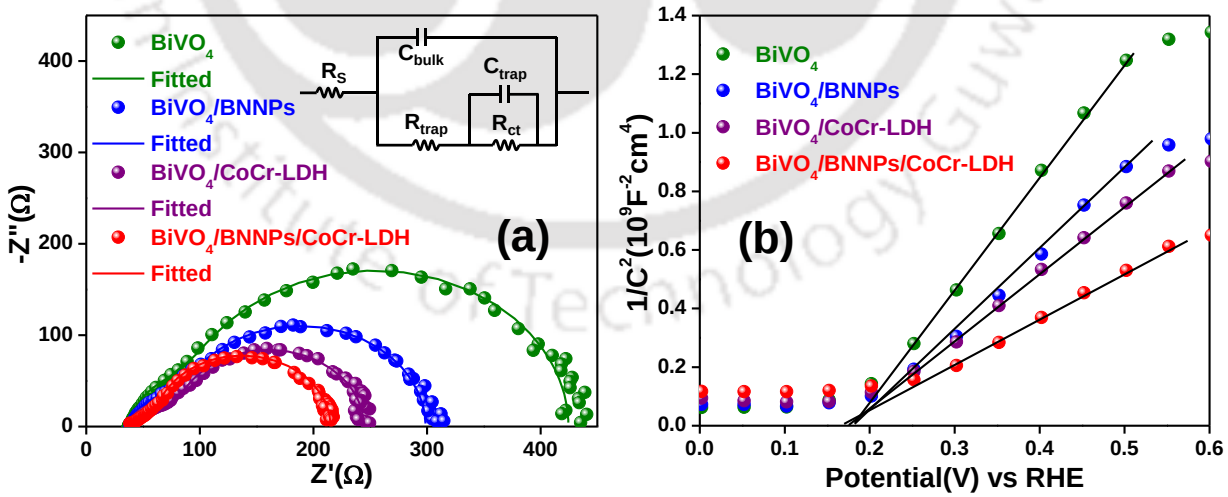

Figure 6.3.10 (a) Nyquist plots for $BiVO_4$, $BiVO_4$/BNNPs, $BiVO_4$/CoCr-LDH and $BiVO_4$/BNNPs/CoCr-LDH photoanodes in addition to their fitted curves and equivalent circuit model at 1.23 V vs RHE under 1 Sun illumination and (b) Mott−Schottky plots for $BiVO_4$, $BiVO_4$/BNNPs, $BiVO_4$/CoCr-LDH and $BiVO_4$/BNNPs/CoCr-LDH photoanodes.

Part of this chapter has been published in **Electrochimica Acta, 2022,415, 140269.**

Table 6.3.1 Nyquist plots fitting parameters for $BiVO_4$, $BiVO_4$/BNNPs, $BiVO_4$/CoCr-LDH and $BiVO_4$/BNNPs/CoCr-LDH photoanodes in addition to their charge carrier densities.

Photoanode	$R_s(\Omega)$	$R_{trap}(\Omega)$	$C_{bulk}(\mu F)$	$R_{ct}(\Omega)$	$C_{trap}(\mu F)$	$N_D(10^{18}\times cm^{-3})$
$BiVO_4$	**39.2**	**105.3**	**19.2**	**280**	**51.8**	**4.2**
$BiVO_4$/BNNPs	**40.8**	**68.4**	**13.7**	**189.4**	**101.3**	**6.1**
$BiVO_4$/CoCr LDH	**42.4**	**45.9**	**10.2**	**156.1**	**74.4**	**7.1**
$BiVO_4$/BNNPs/CoCr LDH	**40.7**	**27.3**	**8.8**	**147**	**251.9**	**10.1**

6.3.7 Charge separation and injection efficiency analysis

In order to get the effectual contributions of BNNPs and CoCr-LDH on charge separation and injection efficiency, hole scavenger (HS) test for all the bare and modified photoanodes was analyzed by adding 0.03 M Na_2SO_3 of hole scavenger with 0.1 M Na_2SO_4 electrolyte, as shown in **figure 6.3.11(a)** and **figure 6.3.11(b)**.[25] The calculated current densities of $BiVO_4$, $BiVO_4$/BNNPs, $BiVO_4$/CoCr-LDH and $BiVO_4$/BNNPs/CoCr-LDH photoanodes in the presence of the hole scavenger are found to be ~ 2.7, ~ 1.3, ~ 1.3 and ~ 1.2 times higher than the corresponding photoanodes in the absence of the hole scavenger. The increment in current density for bare $BiVO_4$ is very high than the $BiVO_4$/BNNPs and $BiVO_4$/BNNPs/CoCr-LDH photoanodes, which confirms the enhancement in electrical conductivity due to the incorporation of hole extractor BNNPs on $BiVO_4$ film. These results confirm the gradual decrement of self-corrosions and potential barriers for $BiVO_4$ based photoanodes with BNNPs and CoCr-LDH modifications. Also, the shifting of onset potentials for bare $BiVO_4$ and $BiVO_4$/BNNPs photoanodes towards lower potential is very high in comparison to $BiVO_4$/CoCr-LDH and $BiVO_4$/BNNPs/CoCr-LDH photoanodes, which illustrates the improvement in catalytic activity due to action of CoCr-LDH over $BiVO_4$ semiconductor. As the hole injection process has already been promoted by co-catalyst modification, the shifting of onset potentials for $BiVO_4$/CoCr-LDH and $BiVO_4$/BNNPs/CoCr-LDH photoanodes are smaller compared to other two photoanodes. The water oxidation kinetics of Na_2SO_3 is approximated to be 100 % as it is very high in comparison to the water oxidation kinetics of other general semiconductors. The enhancing order of η_{sep} from 46 % ($BiVO_4$) to 53 % ($BiVO_4$/BNNPs), 56 % ($BiVO_4$/CoCr-LDH) and 64 % ($BiVO_4$/BNNPs/CoCr-LDH) are shown in **figure 6.3.11(c)**. The η_{sep} data suggests that the charge separation ability for dual modified $BiVO_4$ is better and faster due to the combined effect of BNNPs and CoCr-LDH than the bare and single modified $BiVO_4$ photoanode. Similarly, a very high enhancing order of η_{inj} from 37 %

Part of this chapter has been published in **Electrochimica Acta, 2022,415, 140269.**

($BiVO_4$) to 75 % ($BiVO_4$/BNNPs), 80 % ($BiVO_4$/CoCr-LDH) and 87 % ($BiVO_4$/BNNPs/CoCr-LDH) are shown in **figure 6.3.11(d)**. This result confirms the improvement in charge transportation at the photoanode/electrolyte interface and the decrement in electron-hole recombination due to charge extractor and OECs modifications on $BiVO_4$ thin film. The hindered PEC performance of $BiVO_4$ photoanode due to sluggish hole diffusion on its surface is confirmed from the high η_{sep} (46 %) and low η_{inj} (37 %) values.[14] Hence, the notable enhancement in η_{inj} due to dual modifications of $BiVO_4$ film with BNNPs and CoCr-LDH is the major factor for high PEC water oxidation performance.

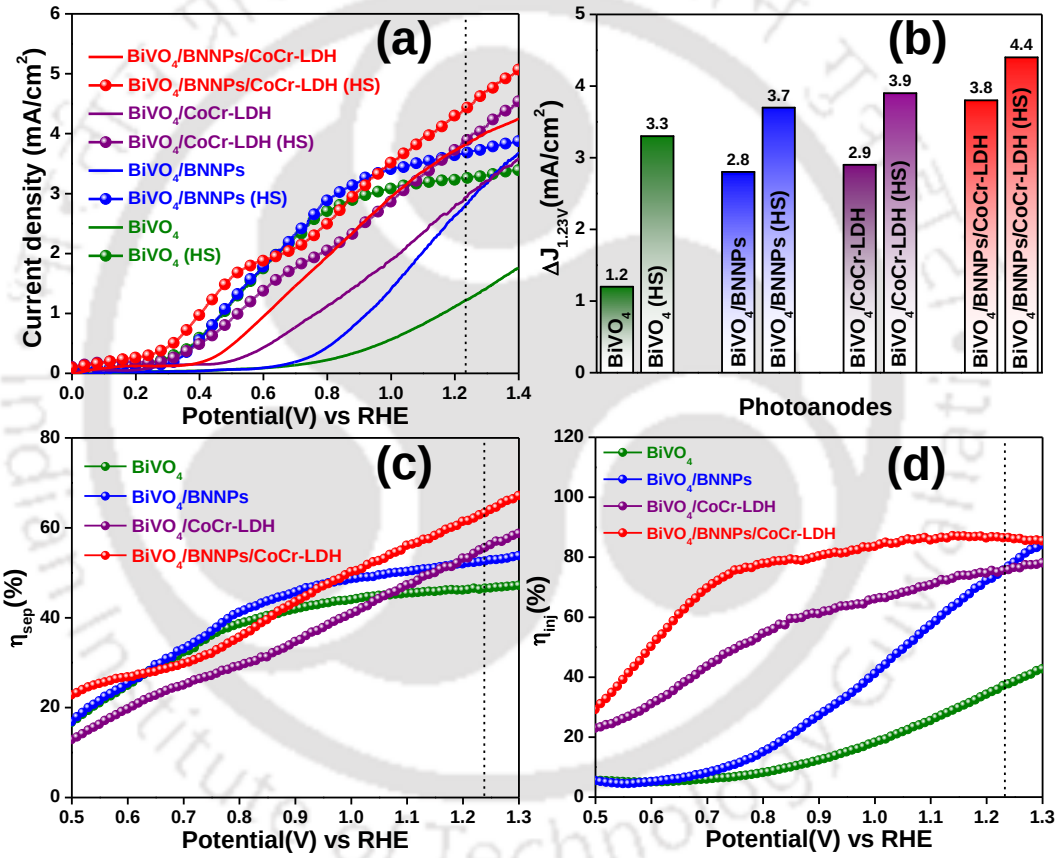

Figure 6.3.11 (a) LSV curves in presence of hole scavenger (Na_2SO_3) in Na_2SO_4 electrolyte under 1 Sun illumination; (b) bar diagram of current density (@1.23 V vs RHE) vs different photoanodes for hole scavenger (HS) test; (c) charge separation efficiencies and (d) charge injection efficiencies of all the bare and modified photoanodes.

6.3.8 Cyclic voltammetry (CV) and proposed mechanism

To further probe the involvement of active redox species, cyclic voltammetry (CV) measurements were performed. From **figure 6.3.12(a)**, it is observed that only Cobalt is electrochemically active species, i.e. Co(II)/ Co(III). The presence of chromium is not

Part of this chapter has been published in **Electrochimica Acta, 2022,415, 140269.**

electrochemically aiding in water oxidation; however, the incorporation of chromium into CoCr-LDH could lead to superior electric conductivity for enhanced OER activities.[18] For better understanding, we have proposed a complete mechanism of our system ($BiVO_4$/BNNPs/CoCr-LDH photoanode) to promote PEC water oxidation based on the earlier results (**figure 6.3.12(b)**). Mechanistically, under illumination, the type II heterostructure ($BiVO_4$ and CoCr-LDH) are connected through BNNPs hole extractor bridging. This type II heterojunction provides an internal built-in electric field to accelerate the charge transfer. Additionally, the electrochemical active species, Co(II) oxidised to Co(III) by receiving holes from BNNPs hole extractor. Later, Co(III) releases those holes to harvest O_2 gas and responds back to its original state, i.e., Co(II). PEC water oxidation is significantly promoted due to the incorporation of a superior hole extraction layer (BNNPs) and hole injection layer (CoCr-LDH) on the $BiVO_4$ surface.

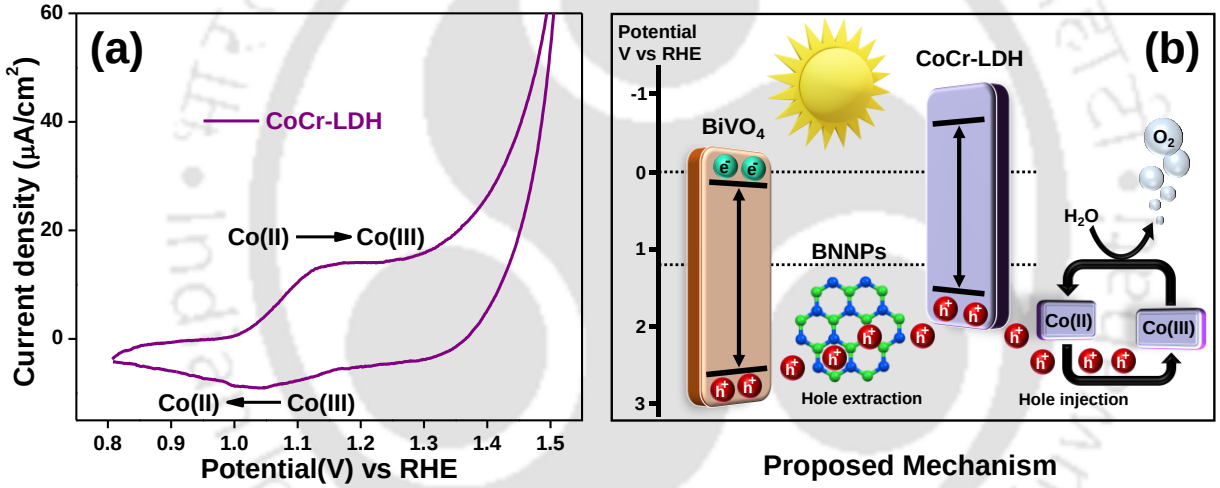

Figure 6.3.12 (a) CV measurement of CoCr-LDH under dark conditions; (b) Proposed mechanism of the $BiVO_4$/BNNPs/CoCr-LDH photoanode for enhanced PEC water oxidation.

6.3.9 Stability and Faradaic yield measurements

Figure 6.3.13(a) represents the continuous operational stabilities of 3h for all the bare and composite photoanodes. After 3h of measurements, the operational stabilities w.r.t. initial photocurrent densities were found to be ~ 81%, ~ 92%, ~ 97% and 99% for $BiVO_4$, $BiVO_4$/BNNPs, $BiVO_4$/CoCr-LDH and $BiVO_4$/BNNPs/CoCr-LDH photoanodes, respectively. The significant improvement in photostability is only because of the additional incorporations of BNNPs and CoCr-LDH. **Figure 6.3.13(b)** indicates the quantified evolved oxygen and hydrogen gases of the composite $BiVO_4$/BNNPs/CoCr-LDH photoanode. The exact figures of experimental evolved

oxygen and hydrogen gases are compared with the theoretical figures to provide Faradaic yield. After 3 h of experiment, an average Faradaic yield of ~ 93.5 % for oxygen gas and ~ 96.5 % for hydrogen gas were recorded.

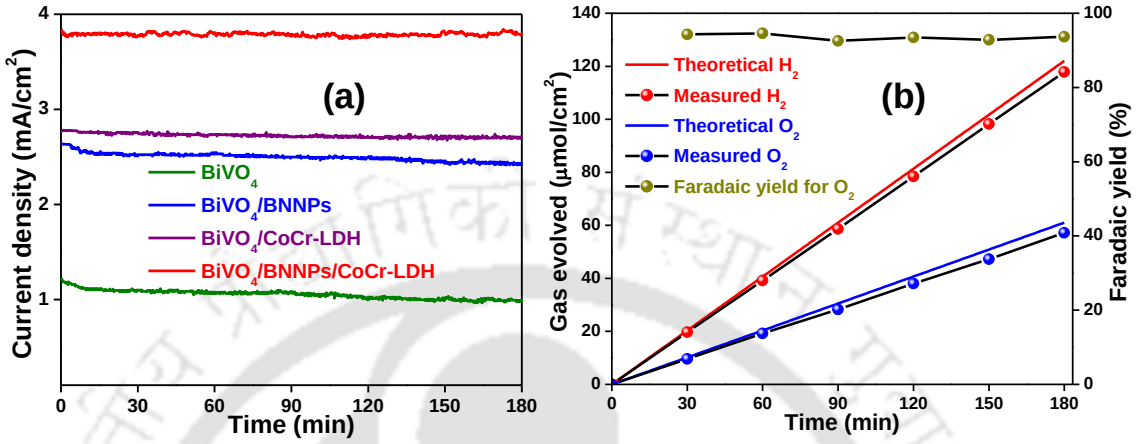

Figure 6.3.13 (a) Continuous operational stabilities of 3h for all the bare and composite photoanodes @ 1.23 V vs RHE under continuous light illumination and (b) Faradaic yield measurement of $BiVO_4$/BNNPs/CoCr-LDH photoanode for oxygen and hydrogen gas evolutions.

6.4 CONCLUSIONS

Firstly, we have incorporated a very thin layer of exfoliated 2D BNNPs as an ultra-rapid hole extractor over the surface $BiVO_4$ photoanode to enhance the speedy charge separation process along with suppressed charge recombination. Secondly, a supplementary OEC based thin layer of CoCr-LDH has been incorporated hydrothermally over $BiVO_4$/BNNPs photoanode to enhance the surface oxidation kinetics. Interfacial insertion of two-dimensional BNNPs between $BiVO_4$ semiconductor and CoCr-LDH results to achieve a maximum photocurrent density of 3.8 mA/cm^2 at 1.23 V vs RHE along with a cathodic shift of ~360 mV onset photocurrent, which indicates the 3.2 fold enrichment in photocurrent density in comparison to bare monoclinic $BiVO_4$. Accelerated PEC water oxidation kinetics, facilitated electrical conductivity, improved charge separation and injection efficiency and boosted electrochemical active surface area were achieved only due to the modifications of $BiVO_4$ photoanode with BNNPs and CoCr-LDH. The current work suggests a reasonable approach for boosted PEC water oxidation efficacy of photoanode by combo modifications with hole extractor and OECs.

Part of this chapter has been published in **Electrochimica Acta, 2022,415, 140269.**

6.5 REFERENCES

1. Y. Park, K. J. McDonald and K.-S. Choi, *Chem. Soc. Rev.*, 2013, **42**, 2321–2337.
2. K. Zhang, B. Jin, C. Park, Y. Cho, X. Song, X. Shi, S. Zhang, W. Kim, H. Zeng and J. H. Park, *Nat. Commun.*, 2019, **10**, 2001.
3. H. L. Tan, R. Amal and Y. H. Ng, *J. Mater. Chem. A*, 2017, **5**, 16498–16521.
4. Q. Z. Wang, T. J. Niu and L. Wang, *Chem. Eng. J.*, 2018, **337**, 506–514.
5. S. K. Pilli, T. E. Furtak, L. D. Brown, T. G. Deutsch, J. A. Turner and A. M. Herring, *Energy Environ. Sci.*, 2011, **4**, 5028–5034.
6. X. Chang, T. Wang, P. Zhang, J. Zhang, A. Li and J. Gong, *J. Am. Chem. Soc.*, 2015, **137**, 8356–8359.
7. H. S. Han, S. Shin, D. H. Kim, I. J. Park, J. S. Kim, P.-S. Huang, J.-K. Lee, I. S. Cho and X. Zheng, *Energy Environ. Sci.*, 2018, **11**, 1299–1306.
8. S. Wang, P. Chen, Y. Bai, J.-H. Yun, G. Liu and L. Wang, *Adv. Mater.*, 2018, **30**, 1800486.
9. M. García-Tecedor, D. Cardenas-Morcoso, R. Fernández-Climent and S. Giménez, Adv. Mater. Interfaces, 2019, **6**, 1900299.
10. M. K. Mohanta, T. K. Sahu, S. Alam, and M. Qureshi, *Chem Asian J.*, 2020, **15**, 3886–3896.
11. W. D. Chemelewski, H. C. Lee, J. F. Lin, A. J. Bard and C. B. Mullins, *J. Am. Chem. Soc.*, 2014, **136**, 2843.
12. F. Tang, W. Cheng, H. Su, X. Zhao and Q. Liu, *ACS Appl. Mater. Interfaces*, 2018, **10**, 6228–6234.
13. B. Gao, T. Wang, X. Fan, H. Gong, P. Li, Y. Feng, X. Huang, J. He and J. Ye, *J. Mater. Chem. A*, 2019, **7**, 278–288.
14. T.K. Sahu, S. Alam, D. Gogoi, N.R. Peela and M. Qureshi, *Acs Appl. Energy Mater.*, 2020, **3**, 5610–5619.
15. W. He, R. Wang, L. Zhang, J. Zhu, X. Xiang and F. Li, *J. Mater. Chem. A*, 2015, **3**, 17977.
16. Y. Fu, F. Ning, S. Xu, H. An, M. Shao and M. Wei, *J. Mater. Chem. A*, 2016, **4**, 3907.
17. Y. Zhao, B. Li, Q. Wang, W. Gao, C. J. Wang, M. Wei, D. G. Evans, X. Duan and D. O'Hare, *Chem. Sci.*, 2014, **5**, 951.
18. C. Dong , X. Yuan , X. Wang , X. Liu , W. Dong , R. Wang , Y. Duan and F. Huang , *J. Mater. Chem. A*, 2016, **4**, 11292 —11298.

19. C. Zachäus, F. F. Abdi, L. M. Peter and R. van de Krol, *Chem. Sci.*, 2017, **8**, 3712–3719.
20. M. Zhong, T. Hisatomi, Y. Kuang, J. Zhao, M. Liu, A. Iwase, Q. Jia, H. Nishiyama, T. Minegishi, M. Nakabayashi, N. Shibata, R. Niishiro, C. Katayama, H. Shibano, M. Katayama, A. Kudo, T. Yamada and K. Domen, *J. Am. Chem. Soc.*, 2015, **137**, 5053–5060.
21. L. Sun, Y. Wang, F. Raziq, Y. Qu, L. Bai and L. Jing, *Sci. Rep.*, 2017, **7**, 1303–1312.
22. B. Liu, S. Yan, Z. Song, M. Liu, X. Ji, W. Yang and J. Liu, *Chem. – Eur. J.*, 2016, **22**, 18899–18907.
23. S. Meng, X. Ye, X. Ning, M. Xie, X. Fu and S. *Chen, Appl. Catal., B*, 2016, **182**, 356–368.
24. T. K. Sahu, M. K. Mohanta and M. Qureshi, *J. Power Sources*, 2020, **445**, 227341.
25. M. K. Mohanta, T. K. Sahu, D. Gogoi, N. R. Peela and M. Qureshi, *ACS Appl. Energy Mater.*, 2019, **2**, 7457–7466.
26. L. Chen, X. Zhang, Z. Zhao, F. Wang, Y. Huang, C. Bai, L. An and Y. Yu, *Colloids and Surfaces A: Physicochemical and Engineering Aspects*, 2021, **614**, 126181.
27. L. Ran and L. Yin, *Adv. Mater. Interfaces*, 2018, **6**, 1800970.
28. B. Matović, J Luković, M. Nikolić, B. Babić, N. Stanković, B. Jokić and B. Jelenković, *Ceram. Int.*, 2016, **42**, 16655–16658.
29. D. Fan, J. Feng, J. Liu, T. Gao, Z. Ye, M. Chen and X. Lv, *Ceram. Int.*, 2016, **42**, 7155–7163.
30. P. Vinothbabu and P. Elumalai, *J. Solid State Electrochem.*, 2015, **19**, 813–820.

Part of this chapter has been published in **Electrochimica Acta, 2022,415, 140269.**

CHAPTER 7

Thesis overview and future perspectives

This chapter, in brief, outlines the outcomes and overview of the current thesis. Herein, it also discusses the possible modification in the near future that can be done with the metal oxides to enhance overall water splitting performance.

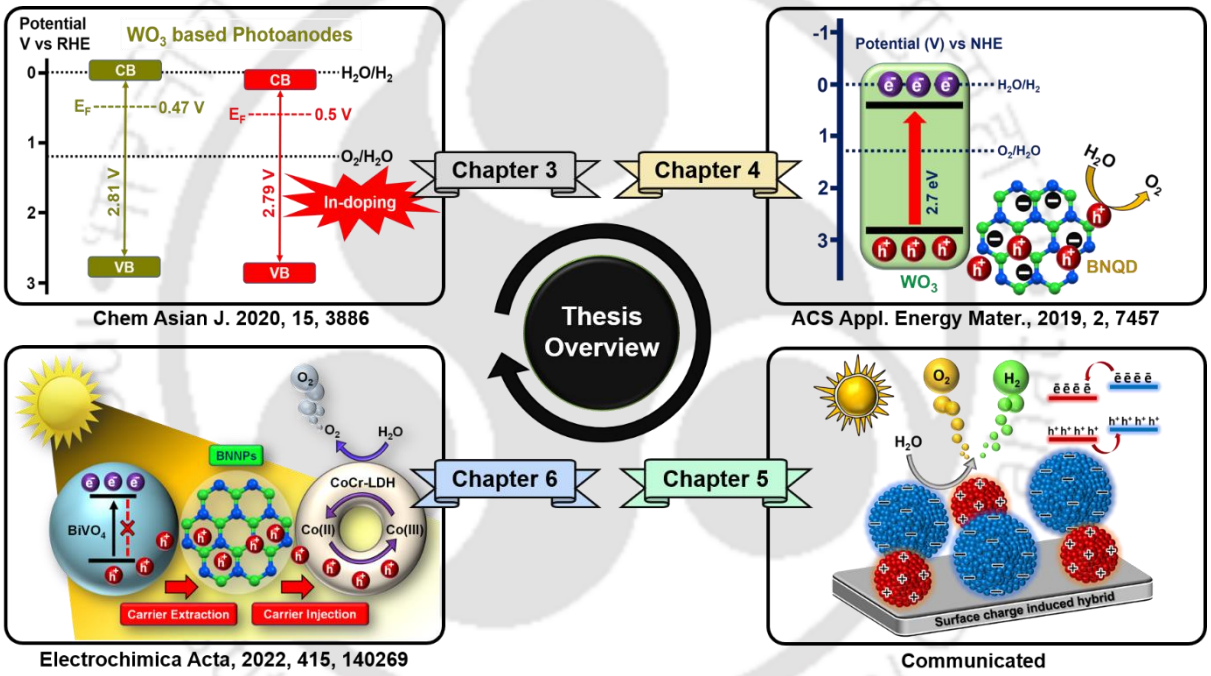

Chem Asian J. 2020, 15, 3886

ACS Appl. Energy Mater., 2019, 2, 7457

Electrochimica Acta, 2022, 415, 140269

Communicated

7.1 THESIS OVERVIEW

The thesis is focused on the design aspects of n-type metal oxide based photoanodes for electrochemical performance mainly using WO_3 and $BiVO_4$ as base semiconductors. The arrangement of this thesis is as follows:

- **Chapter 1** introduces global energy consumption and challenges to achieve sustainable and zero-emission production of energy. This chapter discusses the basics on photoelectrochemical (PEC) water splitting, working principle, new challenging approaches to develop photoelectrodes for improved PEC performance based on the reported literature.
- **Chapter 2** covers the discussions of material synthesis, fabrication and different material characterization techniques, experimental setup and desired analysis for PEC water oxidation.
- **Chapter 3** offers the hydrothermal growth of In-doped monoclinic WO_3 nanoblocks directly over fluorine doped tin oxide (FTO) substrate without the aid of any seed layer. X-ray photoelectron spectroscopy (XPS) data reveals the shifting W^{6+} peaks to lower binding energy by In^{3+}-doping which attributes the shorting of W-O bond and indicates that In^{3+} ions are partially occupying the W^{6+} ions in In-doped WO_3 photoanode. The current density of WO_3 photoanode has been enhanced by 3 times due to In-doping. Mott-Schottky (MS) analysis reveals charge carrier density (N_D) for In-doped WO_3 photoanode has been enhanced by a factor of 3. An average Faradic yield of ~ 90 % has been achieved which can serve as a model system using In^{3+} as a dopant for an inexpensive and attractive method for enhanced WO_3 based PEC water oxidation.
- **Chapter 4** demonstrates the modification of stable monoclinic WO_3 nanoblocks with hexagonal boron nitride quantum dots (h-BNQDs) incorporation to improve the photogenerated electron−hole separation and additionally to hinder the charge recombination process. The photocurrent density of WO_3 photoanode has been enhanced by 2.4 times due to modification with BNQDs which attributes the hole extraction property of BNQDs on WO_3 nanoblock surface. A 2-fold increment in photogenerated charge carrier density (N_D) has been achieved due to better charge separation of electron−hole pairs in the modified system, confirmed by the Mott−Schottky (MS) plot. The present work

demonstrates a unique, low-cost strategy for the enhancement of PEC water oxidation by modification of the photoanode with hole-extracting agents.

- **Chapter 5** determines the widely explored zero-dimensional (0D) non-metal based materials for photoelectrochemical (PEC) electrode modification due to their faster charge transfer and better light harvesting abilities. Herein, we have designed a complimentary charged nanosized 0D-0D hybrid assemble of phosphorous nitride dots (PNDs) (ς = + 9.5 mV) and borophene dots (BDs) (ς = - 26.2 mV) having favorable type-II heterojunction approach among them. A model system has been studied using WO_3 as a semiconductor for showing the effectiveness of PNDs- BDs for PEC water oxidation. The type-II-II′ heterojunction based WO_3/PNDs-BDs photoanode offers a significant three-fold improvement in carrier density expression as compared to bare WO_3 photoanode. The increase in carrier density translates to a four-fold higher current density of 2.8 mA/cm^2 at 1.23 V vs RHE in comparison to the bare WO_3 photoanode. The oppositely charged 0D-0D hybrid model provides rapid carrier separation along with minimized carrier recombination to metal oxide based semiconductor for enhanced PEC water oxidation.
- **Chapter 6** chapter offers the interfacial insertion of hole extractor between semiconductor photoanode and surface oxygen evolution catalyst (OECs) for amplified photoelectrochemical (PEC) water oxidation performance. Herein, modifications of bare monoclinic $BiVO_4$ photoanode with two-dimensional boron nitride nanoplatelets (BNNPs) as hole extractor and CoCr-layered double hydroxides (CoCr-LDH) as kinetics accelerator results to achieve a maximum photocurrent density of 3.8 mA/cm^2 at 1.23 V vs RHE along with a cathodic shift of ~360 mV onset photocurrent, which indicates the 3.2 fold enhancement in photocurrent density in comparison to bare $BiVO_4$. Semiconductor/hole extractor/OECs composite photoanode, i.e., $BiVO_4$/BNNPs/CoCr-LDH offers speedy charge separation with suppressed charge recombination to accelerate the PEC water oxidation kinetics. The presented work is promising as it fill-in the gap between the photoanode and OECs for boosting the PEC water oxidation efficiency of metal-oxide based photoanode.

7.2 FUTURE PERSPECTIVE

The presented thesis outlined the design aspects of n-type metal oxide based photoanodes for electrochemical performance during the research tenure. A detailed study on the photoanodes was carried out to resolve issues related to charge carrier density, photogenerated charge separation, charge injection, charge transfer at the interface and reaction kinetics. Although, several strategies have been adopted here making substantial advancements in the field of photoelectrochemical water splitting, numerous scopes are still available to further improve the overall efficiency towards commercialization. The plausible scopes for the advancement of photoelectrochemical water splitting towards practicality are as follows:

- The poor crystallinity of semiconductors hinders PEC performance. Increasing the crystallinity of these nanostructured photoanodes would be beneficial to its PEC performance. Post-annealing for these nanostructured photoanodes is the most direct way to improve its crystallinity, but the control of ramp rate, annealing temperature, duration, and atmosphere needs to be investigated carefully so as not to damage the nanostructure or undermine carrier mobility.
- Introduction of porosity to the nanostructured photoanode is a feasible way to increase the surface area for better water oxidation reaction. Combination of nano-porosity with a suitable morphology may possibly improve the performance of these photoanodes.
- Exploring new materials such as inorganic perovskite oxides with tunable crystallinity and morphology is another possible way to achieve improved PEC performance.
- Prediction of future structural properties by designing the photoelectrode materials with theoretical calculations and a combination of both theoretical investigation and experimental analysis will solve the limitations of new materials.
- Use of innovative and cost effective fabrication and synthetic methods for wide range of applications.

LIST OF PUBLICATIONS
AND
CONFERENCES ATTENDED

JOURNAL ARTICLES:

Included in the thesis:

1. **Manoj Kumar Mohanta**, Mohammad Qureshi*, Surface charge - directed borophene - phosphorous nitride nanodot heterojunction support for enhanced photoelectrochemical performance. ***J. Phys. Chem. Lett.***, 2023, **59**, 1955–1958, DOI: 10.1039/D2CC05900B

2. **Manoj Kumar Mohanta**, Tushar Kanta Sahu, Sourav Bhowmick, and Mohammad Qureshi*, Synchronized carrier extraction and injection through boron nitride nanoplatelets in hierarchical $BiVO_4$/CoCr-layered double hydroxides for efficient water oxidation. ***Electrochimica Acta***, 2022, **415**, 140269, DOI: 10.1016/j.electacta.2022.140269

3. **Manoj Kumar Mohanta**, Tushar Kanta Sahu, Suhaib Alam and Mohammad Qureshi*, Tuning the Electronic Structure of Monoclinic Tungsten Oxide Nanoblocks by Indium Doping for Boosted Photoelectrochemical Performance. ***Chem.: Asian J.***, 2020, **15**, 3886-3896, DOI: 10.1002/asia.202000787

4. **Manoj Kumar Mohanta**, Tushar Kanta Sahu, Devipriya Gogoi, Nageswara Rao Peela, Mohammad Qureshi*, Hexagonal Boron Nitride Quantum Dots as a Superior Hole Extractor for Efficient Charge Separation in WO_3-Based Photoelectrochemical Water Oxidation. ***ACS Appl. Energy Mater.***, 2019, **2**, 7457-7466, DOI: 10.1021/acsaem.9b01450

Work contributed /performed off the thesis:

5. Bishal Das, Laxmi Prasad Rao Pala, **Manoj Kumar Mohanta**, Meghali Devi, Debarati Chakraborty, Nageswara Rao Peela, Mohammad Qureshi and Siddhartha Sankar Dhar*, Organic-inorganic hybrid photocatalyst consisting of highly conjugated metal complex and graphitic carbon nitride for efficient hydrogen evolution and Cr(VI) reduction. ***J. Mater. Chem. A***, 2022, **10**, 23691-23703, DOI: 10.1039/D2TA05200H
6. Pronoy Dutta, Sujit Kumar Deb, Amalika Patra, Abhisek Majumdar, Golam Masud Karim, Chintak Kamalesh Parashar, **Manoj Kumar Mohanta**, Mohammad Qureshi, Uday Narayan Maiti*, Electric Field Guided Fast and Oriented Assembly of MXene into Scalable Pristine Hydrogels for Customized Energy Storage and Water Evaporation Applications. ***Adv. Funct. Mater.***, 2022, 2204622, DOI: 10.1002/adfm.202204622

7. Tushar Kanta Sahu, Suhaib Alam, Sourav Bhowmick, **Monaj Kumar Mohanta** and Mohammad Qureshi*, Phosphorous Nitride Nano-dots as a Versatile and Metal-free Support for Efficient Photoelectrochemical Water Oxidation. ***Chem. Commun.***, 2021, **57**, 6157-6160, DOI: 10.1039/D1CC01030A
8. Sourav Bhowmick, **Manoj Kumar Mohanta** and Mohammad Qureshi*, Transcription methodology for rationally designed morphological complex metal oxides: a versatile strategy for improved electrocatalysis. ***Sustainable Energy Fuels***, 2021, **5**, 6392-6405, DOI: 10.1039/D1SE01516H
9. Tushar Kanta Sahu, **Manoj Kumar Mohanta** and Mohammad Qureshi*, Modulating Water Oxidation Kinetics Utilizing h-BN Quantum Dots as an Efficient Hole Extractor on Fluorine Doped Hematite Photoanode. ***J. Power Sources***, 2020, **445**, 227341, DOI: 10.1016/j.jpowsour.2019.227341

CONFERENCES ATTENDED

1. Poster presentation at **Chemical Research Society of India 28th National Symposium in Chemistry (CRSI NSC-28),** IIT Guwahati, Guwahati, India, February 2022
2. Oral presentation at **7th International Conference on Advanced Nanomaterials and Nanotechnology (ICANN-2021)**, IIT Guwahati, Guwahati, India, December 2021
3. Poster presentation at **Recent Advances and Innovations in Solar Energy (RAiSE-2021)**, DST-IITM Solar Energy Harnessing Centre, IIT Madras, Chennai, India, December 2021
4. Poster presentation at **6th International Conference on Advanced Nanomaterials and Nanotechnology (ICANN-2019)**, IIT Guwahati, Guwahati, India, December 2019
5. Poster presentation at **International Conference on Frontiers in Chemical Sciences (FICS-2018)**, IIT Guwahati, Guwahati, India, December 2018